Optical Metasurfaces for Information Efficient Nanoscale Metrology

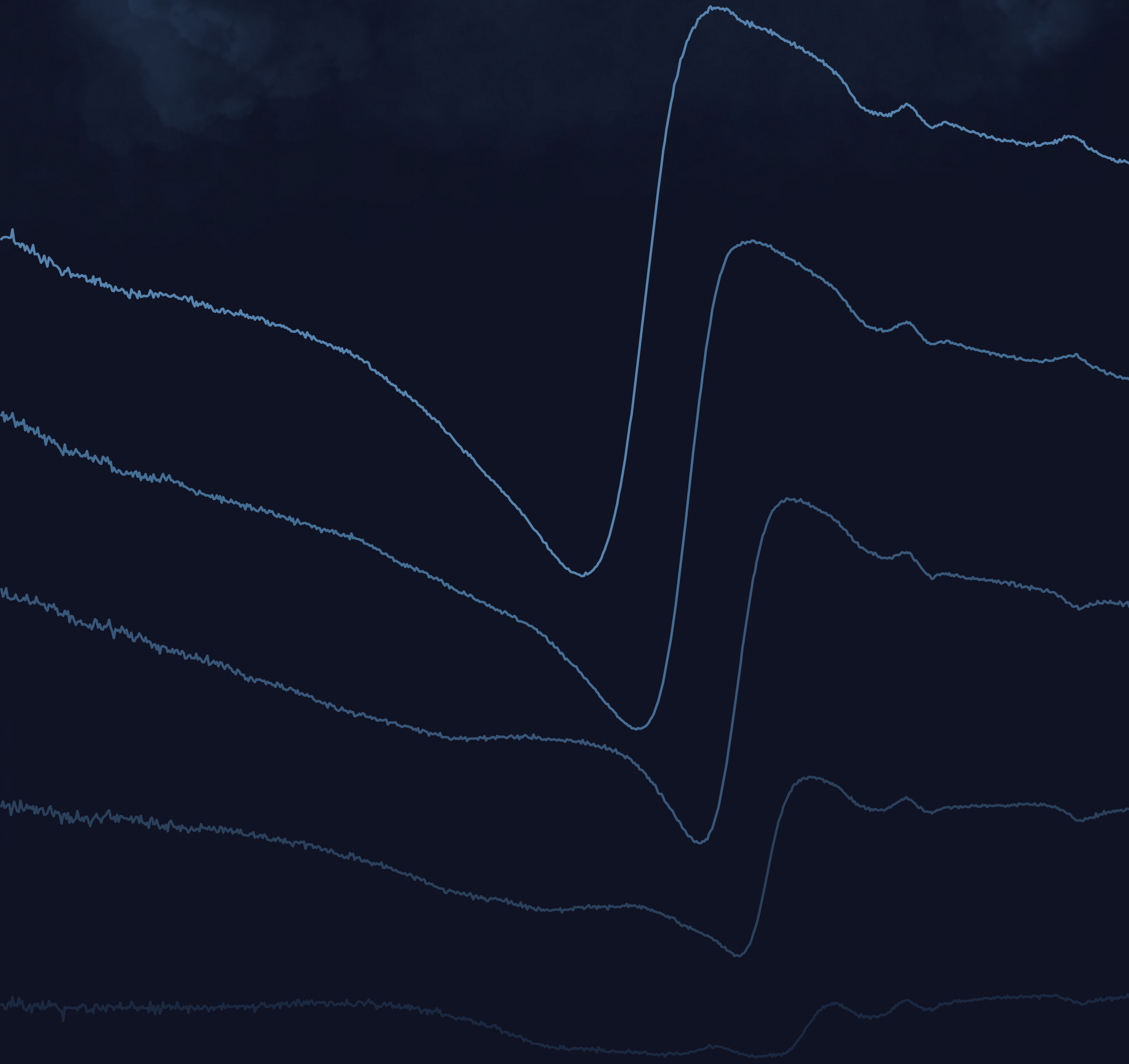

Nick Feldman

Optical Metasurfaces for Information Efficient Nanoscale Metrology

Ph.D. Thesis, University of Amsterdam, December 2025
Optical Metasurfaces for Information Efficient Nanoscale Metrology
Nick Feldman

ISBN: 978-94-92323-98-9

The work described in this thesis was performed at
AMOLF, Science Park 104, 1098 XG Amsterdam, The Netherlands, and
ARCNL, Science Park 106, 1098 XG Amsterdam, The Netherlands.

This work is part of the Netherlands Organisation for Scientific Research (NWO).

Printed by: Proefschriftspecialist — www.proefschriftspecialist.nl.

Optical Metasurfaces for Information Efficient Nanoscale Metrology

ACADEMISCH PROEFSCHRIFT

ter verkrijging van de graad van doctor
aan de Universiteit van Amsterdam
op gezag van de Rector Magnificus
prof. dr. ir. P.P.C.C. Verbeek
ten overstaan van een door het College voor Promoties ingestelde commissie,
in het openbaar te verdedigen in de Agnietenkapel
op woensdag 17 december 2025, te 10.00 uur

door

Nick Feldman

geboren te Roermond

Promotiecommissie

Promotor:	prof. dr. A. F. Koenderink	Universiteit van Amsterdam
Copromotor:	dr. L. V. Amitonova	ARCNL
Overige leden:	prof. dr. P. C. M. Planken	Universiteit van Amsterdam
	prof. dr. E. Alarcón Lladó	Universiteit van Amsterdam
	dr. K. I. E. Olsson	Universiteit van Amsterdam
	prof. dr. A. P. Mosk	Universiteit Utrecht
	prof. dr. A. Tittl	Ludwig-Maximilians-Universität München

Faculteit der Natuurwetenschappen, Wiskunde en Informatica

Contents

Chapter 1

Introduction

1.1 Light and information

Throughout history, light has played a pivotal role in how we gather and understand information about the world. It enabled us to form images of our immediate surroundings through vision, communicate over long distances using fire beacons and lighthouses, measure the passage of time with sundials, and navigate unknown terrains by starlight. Recognizing the immense potential of light as an information carrier, humanity has developed ingenious instruments over time, such as telescopes and microscopes, to extract information from otherwise inaccessible realms of the universe. In our society today, which is also termed the Information Age [1], the rapid developments in digital technologies and the internet have fundamentally transformed the way we access, share, and process information. Yet, light continues to serve as an indispensable medium at the heart of these processes.

First of all, light is used as a tool for information *transfer*. A prominent example of this use case is the optical fiber [2], which ensures high-speed data transmission over trans-oceanic distances. Moreover, rapid progress in the field of photonic integrated circuits [3] has lead to applications such as short-range optical interconnects between chips and communication devices in data centers. Second, although less mature, light could be utilized to *process* information and perform computations [4] through, for instance, a photonic equivalent of the transistor [5]. Third, light is used as an interrogation tool in measurements to *gain* information about physical systems. Famous examples include optical microscopy, which retrieves spatial information about objects on the micro- and nanoscale, fluorescence [6] and Raman [7] spectroscopy for precise molecular fingerprinting, and the recent LIGO experiment [8], where light is able to probe the minuscule space-time distortions resulting from gravitational waves. The encompassing field in which light is used to perform measurements on physical systems is called *optical metrology*, and will be the main use case discussed in this thesis.

A highly relevant and vibrant application domain within optical metrology is the semiconductor device manufacturing industry. This industry is characterized by impressive developments over the past 40 years, allowing microchips to perform ever more complex tasks at faster speeds. These developments are driven by a trend known as Moore's law [9], which states that the dimensions of the individual transistors on a microchip are halved approximately every two years. Currently, the most advanced microchips are composed of hundreds of layers of complex networks, where the feature sizes of individual components reach dimensions as small as 10 nm [10], and where individual layers need to be stacked on top of each other with an accuracy of 0.1 nm. These impressive demands require noninvasive, fast, and precise metrology tools to monitor any potential mishaps that might arise during chip fabrication, such as relative misalignments between layers in the stack, defects in individual components, surface roughness, and shape variations. The microchip, thereby, comprises a specific nanoscale system, from which information about structural parameters is to be extracted using an optical measurement. The work in this thesis revolves around the development of such advanced optical metrology platforms that efficiently retrieve information from nanoscale systems that simulate the typical environment of a microchip.

An optical metrology protocol is an intricate dance between three main interconnected players, as visualized in Figure 1.1. First, an *illumination* generates a specific electromagnetic probe which will act as the main carrier of information. The probe is incident upon a *nanoscale environment* or *sample* from which specific information is to be extracted. A nanoscale parameter should, therefore, influence the incident probe in such a way as to leave a specific fingerprint onto the carrier signal. Finally, a *detector* reads out the fingerprint

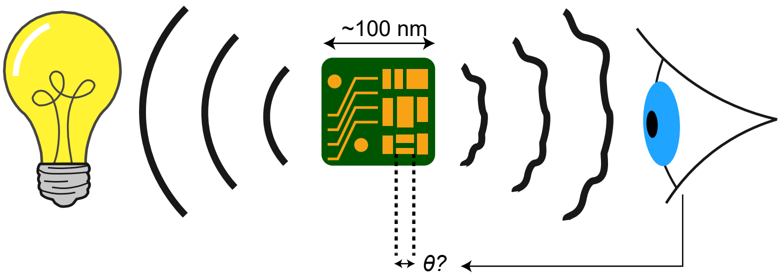

Figure 1.1: Optical metrology consists of an illumination probe incident upon a sample from which information is to be retrieved. The sample leaves a specific fingerprint on the probe, which a detector is able to read out.

from the signal, after which nanoscale parameters can be estimated. The goal of the experimentalist is to optimize the interactions between all players in the dance such that maximum information about the parameter is retrieved.

1.2 Defining information

In this didactic section, we introduce concepts from information theory that will allow us to precisely define and quantify information in the context of this thesis. Let θ therefore be a specific parameter that we would like to retrieve from a measurement, which, as an example, we set as the x-coordinate of the position x of a nanoscale object, as visualized in Figure 1.2a. In the next section, we describe various experimental tools that can be used to develop a measurement protocol for efficient parameter retrieval. For now, we can regard the measurement as a black box which generates data in the form of bright Gaussian spots, as shown in Figures 1.2b and 1.2c, where the center of the spot corresponds to the position of the nano-object. No measurement is perfect, and experimental data is unavoidably corrupted by some form of noise arising from random fluctuations in, for example, the environment or the electronics of the detector. A very common type of noise in optical experiments is shot-noise, which describes the random fluctuations in the light field itself that scale with the square root of the number of detected photons, and we assume that this is the dominant source of noise in our data. Figures 1.2b and 1.2c show data of the Gaussian spot when a high respectively low number of photons is detected, which correspond to a high and low signal-to-noise ratio (SNR) respectively.

After a measurement is performed, an operation is needed that translates noisy experimental data into an estimated value of the parameter $\hat{\theta}$, which is termed an *estimator*. An option is to apply a Gaussian curve fitting routine on the image while leaving the unknown x-coordinate x as a free fit parameter. We perform this fitting-based estimation procedure on 2000 different realizations of the noisy data of Figures 1.2b and 1.2c, and plot the estimated parameter $\hat{x}$ in a histogram plot in Figure 1.2d, where the black and red bars denote estimations applied on data that contain a high and low SNR, respectively. It can be observed that both estimation histograms form distributions centered around the true value of x, which in this example is apriori known. This indicates that the estimation procedure is *unbiased*: the average value of the estimator $\hat{x}$ is equal to the true parameter x. Furthermore, the standard deviation of the estimation distribution σ_x is lower for the data with a higher SNR, suggesting that the *precision* of the estimation procedure is higher for data with higher SNR, as expected from intuition. In addition to curve fitting, there may be other estimators that can be applied to the data to retrieve parameter estimates of x that might result in an even higher estimation precision than that obtained in Figure 1.2d. However, there exists a fundamental bound

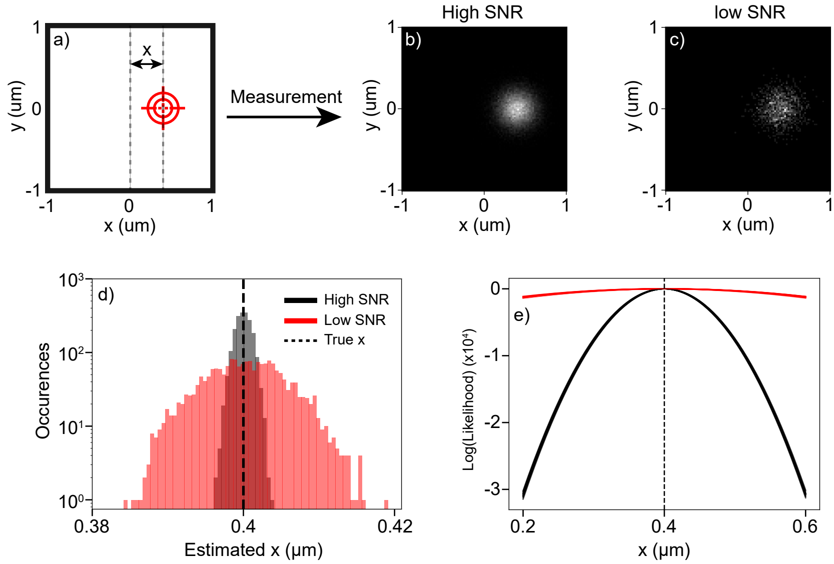

Figure 1.2: Measurement, estimation and information (A) An example parameter of a system that is to be estimated is the x-coordinate of an object on the nanoscale. Panels (B) and (C) denote measured data of the nano-object with a high and low SNR, respectively. (D) Estimation histograms of the x-coordinate of the object by performing a Gaussian fitting routine on 1000 configurations of the noisy data of panels (B) and (C), highlighted by black and red bars, respectively. (E) Log-likelihood as a function of the x-coordinate for both high and low SNR data, indicated by black and red curves, respectively.

on the precision of *any* unbiased estimator that is applied to noisy data. This is the *Cramer-Rao precision bound*, and is defined as

$$\sigma_x \geq \frac{1}{\sqrt{F}}, \tag{1.1}$$

where F is a quantity called the *Fisher information*. The Fisher information indicates the amount of information a specific dataset contains about a parameter θ, and estimators that reach the Cramer-Rao bound are termed efficient in the sense that these estimators optimally harness all available Fisher information in the data.

To gain more insight in the concept of Fisher information, we review the notion of *likelihood*. The likelihood function $p(I, \theta)$ is defined as the probability p of the system being parametrized by θ, given a certain measured dataset I. Since we assumed shot-noise as the main noise contribution in the data, we can express the likelihood function as a Poisson function:

$$p(I, \theta) = \prod_{i=0}^{N} p_i(I_i, \theta) = \prod_{i=0}^{N} \frac{\mu_i(\theta)^{I_i} e^{\mu_i(\theta)}}{I_i!}. \tag{1.2}$$

Here, $p_i(I_i, \theta)$ is the probability of measuring I_i photons on pixel i on the detector and $\mu_i(\theta)$ the expected number of photons on that pixel, which is equivalent to a noise-free Gaussian spot. Since we measure an image of N mutually independent pixels, the total probability factorizes as a product. Because we have access to a complete model of the noise and the expected data $\mu(\theta)$, we have direct access to the likelihood $p(I, \theta)$ as well, but it is important to note that in an experimental setting $p(I, \theta)$ is generally unknown. Likelihood functions often involve multiplying very small numbers, and it is more convenient to work with the logarithm of the likelihood function $\log(p(I, \theta))$, given by

$$\log(p(I,\theta)) = \sum_{i=0}^{N} I_i \log(\mu_i(\theta)) - \mu_i(\theta) - \log(I_i!). \tag{1.3}$$

We visualize $\log(p(I, \theta))$ for 25 individual measurements of both high and low SNR Gaussian signals in Figure 1.2e as black and red curves, respectively, and ask the question: *"Which measurements contain more information about x?"*. Clearly, both sets of curves peak around the true parameter value x, which is the *maximum likelihood estimation* for both datasets. However, for the low SNR dataset, it is more likely to estimate a wider range of x values than for the high SNR dataset. Therefore, the curvature of $\log(p(I, \theta))$ evaluated at the true parameter θ is a direct measure of the amount of information a dataset contains about the parameter θ. Indeed, the definition of Fisher information is given by [11]

$$F = -E\left[\left. \frac{\partial^2 \log(p(I,\theta))}{\partial \theta^2} \right|_{\theta} \right], \tag{1.4}$$

where $E[.]$ indicates the expectation operator. By explicit evaluation of the Fisher information, we can calculate the Cramer-Rao bounds of both the high and low SNR data in the example at hand, and obtain $\sigma_{\hat{x}CR,\text{high SNR}} = 0.8$ nm and $\sigma_{\hat{x}CR,\text{low SNR}} = 4.0$ nm, respectively. If we compare this result with the estimation precisions retrieved from the histograms in Figure 1.2d, which are $\sigma_{\hat{x},\text{high SNR}} = 1.1$ nm and $\sigma_{\hat{x}\text{low SNR}} = 5.3$ nm, we can see that the fitting-based estimation procedures are close to, yet do not violate, the Cramer-Rao precision bounds, demonstrating the efficiency of the estimators.

Equations (1.3) and (1.4) highlight an important additivity property of Fisher information. Given N independent measurements each containing Fisher information F, the Fisher information of the composite measurement is $F_{tot} = \sum_{i=0}^{N} F = NF$. In summary, the experimentalist has three different strategies to extract as much information about a system's parameter: 1) generating very informative data in the first place, 2) performing as many measurements as possible, and 3) making optimal use of the data by finding an estimator that reaches the Cramer-Rao bound. Since option 2) is not always possible in many applications where a fast measurement is paramount, such as the domain of semiconductor metrology, the work in this thesis will mainly address strategy 1) by developing information-efficient measurement protocols. While the example discussed in this section specifically applies to object localization from image data, the Fisher information formalism also holds generally for any other measurement scheme and data type from which parameters are to be estimated.

1.3 Metrology: the art of measuring informatively

As mentioned previously, an informative optical metrology protocol requires an optimum interaction between the illuminations, the environment, and the detection strategy. In the following sections, we will briefly review the relevant tools available on all three fronts that allow the development of an information-efficient measurement scheme.

1.3.1 Shaping the environment

The first strategy towards developing an information efficient measurement is to shape the nanoscale environment, or sample, in which a relevant parameter is embedded. The sample should be engineered such that a small parameter variation generates a strong response upon illumination by a probe that can be effectively transduced onto a detectable signal. To this end, strong light-matter interactions between the probe and the nanoscale environment are desirable. The field of nanophotonics [13] provides a rich and flexible toolkit to enhance and control light-matter interactions on the nanoscale. For example, metallic [14] and dielectric nanoparticles [15] host a plethora of photonic modes that resonantly enhance local nanoscale electromagnetic fields. These modes originate from the resonant oscillation of free electrons in metallic particles, or bound electrons in dielectric particles, and are termed plasmon and Mie resonances, respectively. Consider, for example, the case of a silicon cylinder with height H =100 nm, radius R =82 nm, and permitivitty $\epsilon = 12$ embedded in vacuum, as shown in Figure 1.3a. The photonic modes of this structure can be obtained by performing eigenmode simulations with the finite element method (COMSOL), and the magnitudes of four exemplary modal electric field distributions are shown in Figure 1.3b. It can be seen that the modes form strongly enhanced and localized electric field hotspots in the vicinity of the nanocylinder. By close inspection of the field distributions, one can identify the modes, from left to right, as electric quadrupole (EQ), magnetic quadrupole (MQ), electric dipole (ED), and magnetic dipole (MD) resonances. These modes can be excited by an external probe which we, for now, set as a linearly polarized plane wave normally incident on the cylinder. To gain insight into how the modes generate a response that is transduced into a far-field signal, we calculate the far-field scattering cross section σ_{scat} of the cylinder as

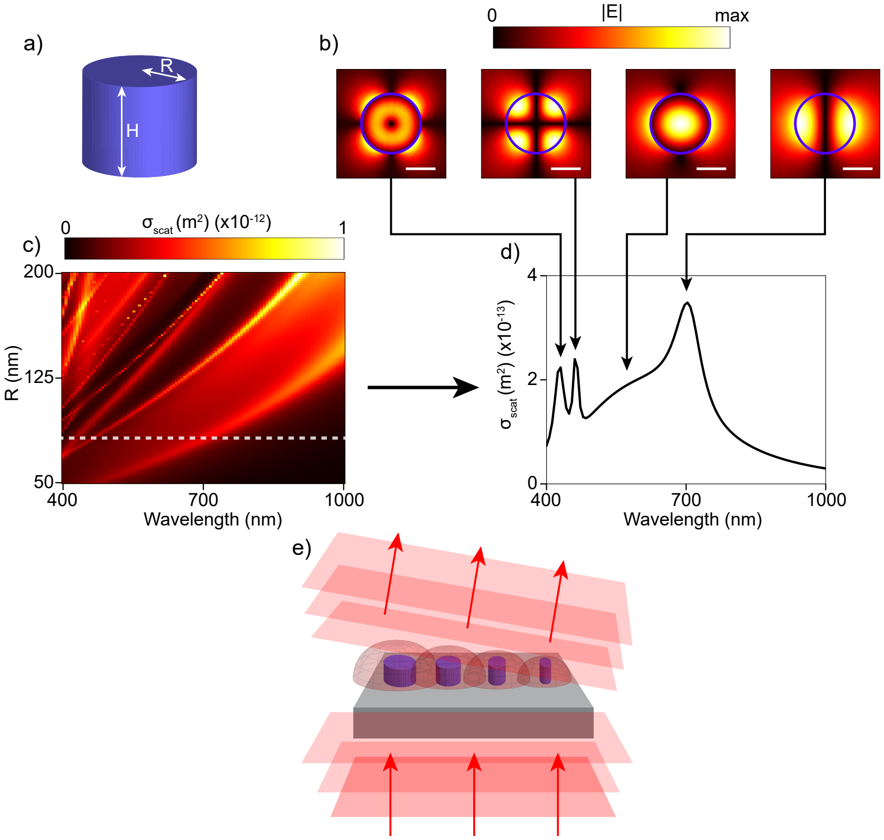

Figure 1.3: Tuning light-matter interaction with nanoparticles (A) Sketch of a dielectric nanocylinder with height H and radius R. The height is set to $H = 100$ nm. (B) Top view of the magnitude of the electric field eigenmode profiles corresponding to, from left to right, the EQ, MQ, ED, and MD resonance. The radius of the cylinder is set to 82 nm, and the scalebar corresponds to 80 nm. (C) Scattering cross section of the cylinder versus wavelength and radius. (D) 1D scattering cross section versus wavelength of the cylinder with a radius of 82 nm. (E) A collection of nanoparticles with different shapes patterned on a substrate forms a metasurface, that, in this case, steers an incident beam into a different direction. Calculation inspired by Ref. [12].

a function of the illumination wavelength and plot the result in Figure 1.3d. Several peaks in the scattering response can be discerned, which correspond to resonant excitations of the modes discussed in Figure 1.3b. The geometric parameters of the resonator can be used as a flexible tuning knob to engineer modes on the nanoscale. To see this, we calculate the scattering cross sections versus both wavelength and radius R of the cylinder, and visualize the results in Figure 1.3c. It can be seen that the spectral positions of the resonant modes redshift for increasing R, which is due to the fact that a larger resonator results in a higher effective modal resonant wavelength. This spectral sensitivity of photonic modes already provides a first example of how a nanophotonic object can be used to efficiently generate information about, in this case, the geometrical parameter R.

The flexible tuning of the electromagnetic environment on the nanoscale through the use of nanoparticles was quickly exploited by the metamaterials community [16], whose objective is to engineer artificial materials with specifically designed properties that cannot be found in nature. For instance, it was realized that individual nanoparticles with precisely chosen shapes and sizes could be fabricated on a 2D surface, termed a metasurface [17, 18], where the combination of all local electromagnetic responses would generate a compound response that could be tailored at will. The concept is visualized in Figure 1.3e. By using the fact that the scattering response (in this particular case the scattered phase) of individual cylinders is dependent on R, a metasurface can be designed that steers an incident beam into a different direction. Apart from beamsteering, metasurfaces with a wide range of functionalities have been designed that range from ultra thin optical elements [17, 19, 20], hologram projectors [21, 22], perfect absorbers [23] and computing devices [24, 25].

A powerful advantage of metasurfaces is that they can host strong collective effects between the individual particles on the surface, which could be used to enhance light-matter interactions even further. An example of such a collective effect is the Fano resonance [26], which is a modal interference effect that can lead to ultra narrow linewidth spectral features and enhanced local fields. These properties have sparked an enormous interest in the nanophotonics community, specifically in the fields of non-linear optics [27, 28] and sensing [29]. A very convenient strategy to engineer Fano resonances in the metasurface community is based on the concept of bound states in the continuum (BIC) [30, 31]. BICs are peculiar resonant states that are embedded within the radiation continuum, but, contrary to the modes we have encountered in Figure 1.3, completely decoupled from that continuum. True BIC modes can, therefore, not be excited by an incident far-field probe. In practical scenarios, a BIC is transposed into a so-called quasi-BIC by introducing a structural asymmetry to the metasurface geometry, which opens a coupling channel to the far-field. Figure 1.4a shows an archetypical example of a Fano resonant metasurface [12] based on quasi-BIC modes. The unit cell consists of 2 silicon

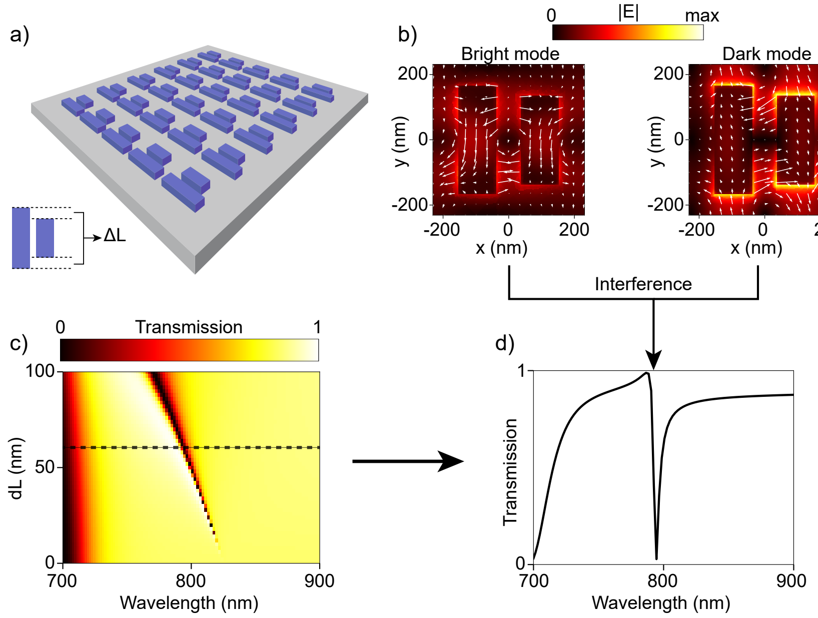

Figure 1.4: Fano resonances and quasi-BIC modes in dielectric metasurfaces. (A) Example of a dielectric Fano resonant metasurface. The unit cell consists of 2 silicon rods, which have a length mismatch ΔL. (B) Super-radiant and sub-radiant mode profiles that lead to the Fano interference. The colorbar and white arrows indicate magnitude and real part of the electric fields, respectively. (C) Simulated metasurface transmission versus wavelength and ΔL. (D) Metasurface transmission spectrum versus wavelength, for $\Delta L = 60$ nm.

nanorods that have a slight length mismatch ΔL that represents the necessary structural asymmetry. Figure 1.4b shows the corresponding dominant eigenmode profiles of the metasurface unit cell. A dipolar-like super radiant (bright) mode and a quadrupolar sub radiant (dark) mode can be discerned with an efficient respectively inhibited coupling to the far-field, where ΔL, set to 60 nm here, functions as tuning knob to control the coupling rate of the dark mode. These are exactly the two modes that are responsible for the Fano interference effect. Indeed by calculating the transmission spectrum of the metasurface, a sharp, asymmetric Fano lineshape is observed. To visualize the importance of the asymmetry parameter ΔL, we show the metasurface transmission versus wavelength and ΔL in Figure 1.4c. As ΔL decreases, the linewidth of the Fano resonance decreases until eventually disappearing when ΔL approached zero, reminiscent of a quasi-BIC mode excitation. Many realizations of these quasi-BIC metasurfaces have already been exploited to generate informative responses in nanoscale sensing experiments [32, 33].

1.3.2 Detection techniques

Strong nanoscale responses are futile without an efficient detection of the relevant signal. One of the most powerful detection tools available in the optical metrology community is the conventional microscope, as shown in Figure 1.5a. Here, light is collected from a sample using an objective lens and projected onto a camera by a tube lens, forming a magnified image of the sample under study. Ever since its invention in the 17th century, microscopes have been used to acquire direct images of samples that are too small to see by the naked eye alone, and still form the backbone of many state-of-the-art scientific instrumentation in the fields of physics, biology and medical diagnostics. The main form of information that is retrieved with conventional microscopes is the size d of the features of the sample under study, which is bounded by a fundamental resolution limit discovered by Ernst Abbe [34]

$$d = \frac{\lambda}{2\mathrm{NA}}. \tag{1.5}$$

Here, λ is the wavelength of the collected light, and NA $= n\sin(\theta)$ is the numerical aperture of the objective lens with an acceptance half angle θ immersed in a medium of refractive index n. Assuming that the objective has an NA of 0.8 and is immersed in air ($n = 1$), while illuminating a sample with a typical optical wavelength of $\lambda = 500$ nm, the minimum feature size that can be discerned is roughly 300 nm. Retrieving structural information of deeply subwavelength ($d << \lambda$) is, therefore, an enormous challenge within optical metrology. In a later section we will discuss some strategies beyond conventional imaging with which deeply sub-wavelength information can nevertheless be retrieved with an optical measurement.

Instead of imaging the sample directly, an extra lens can be inserted in the imaging system of Figure 1.5a, such that the back-focal-plane (BFP) of the microscope objective is imaged onto the camera as shown in Figure 1.5b. Parallel rays that are captured within the same collection angle are focused at specific locations in the BFP, which thereby provides information about the directional light scattering or emission originating from the sample. Since the collected fields in the BFP are related to the fields in the sample plane by a Fourier transform, this technique is also termed "Fourier microscopy". As can be seen from the BFP image in Figure 1.5b, only collection angles, or in plane wave vector components $k_{||}/k_0$, that lie within the NA of the objective (NA=0.8) are captured, which is causing the blurring of the corresponding magnified object in Figure 1.5a due to the resolution limit of equation (1.5).

Microscopes can be equipped with a dispersive element for spectroscopic measurements, such as a grating or prism, in the detection path of the system to retrieve wavelength-resolved information, as shown in Figure 1.5c. As we have already encountered in the previous section, many nanoscale objects contain resonances which are highly sensitive to nanoscale parameters such

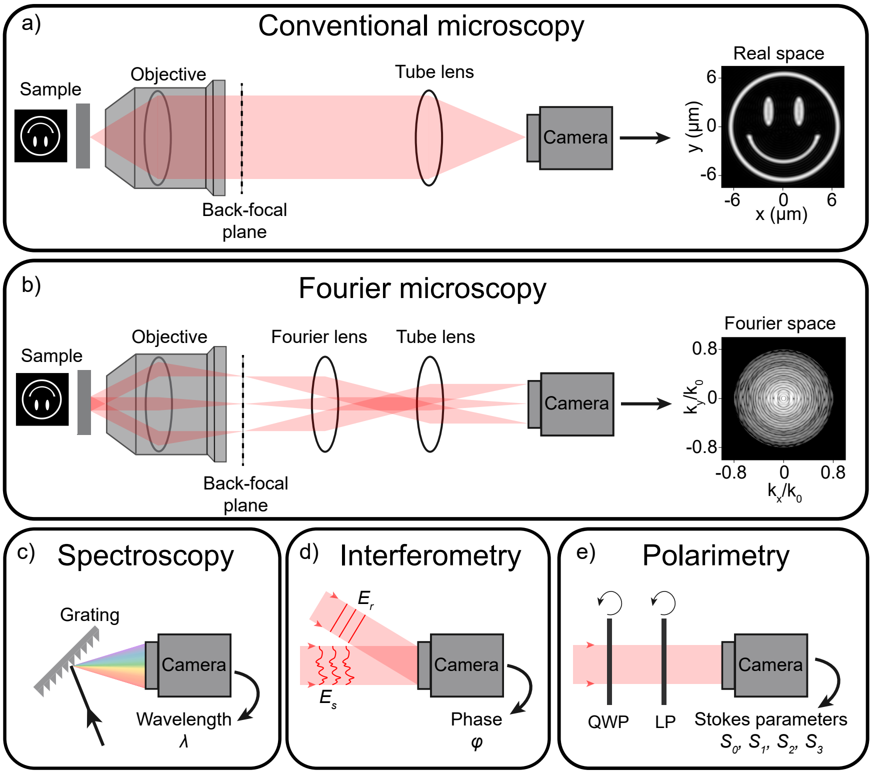

Figure 1.5: Detection techniques in optical metrology (A) Conventional microscopy produces a magnified image of a sample under study. (B) Fourier microscopy images the wave vector (Fourier) space of the sample. (C) A dispersive element in front of the camera provides access to wavelength-resolved information. (D) In interferometry, the relevant unknown signal E_s is interfered with a reference field E_r, which allows to retrieve the phase of the unknown signal. (E) Using a quarter wave plate (QWP) and a linear polarizer (LP), the full polarization state of a signal can be reconstructed through acquition of the Stokes parameters.

as dimension, morphology and local perturbations. Experimental techniques such as transmission, reflection and dark-field spectroscopy [35] are thereby indispensable characterization tools to precisely identify these resonant features.

In the detection modalities discussed so far, a signal is typically acquired on Complementary Metal-Oxide-Semiconductor (CMOS) or Charge-Coupled Device (CCD) cameras, which are all detectors that are sensitive only to the intensity of a signal. However, light is a wave that contains both intensity and phase information, and phase information is lost during signal acquisition. Even so, phase information can still be retrieved from a signal using several techniques based on interferometry, as shown in Figure 1.5d. In these techniques, an unknown complex field E_s is coherently mixed with a reference field E_r on the camera, and through postprocessing of the resulting interference pattern the unknown phase of E_s is recovered. Phase information has indeed proven to be invaluable over the course of time, where the archetypical Michelson interferometer has been used to perform accurate metrology of parameters such as the speed of light in the Michelson-Morley experiment, or, more recently, the minuscule displacement between two mirrors caused by gravitational waves.

A final fundamental property of light onto which information can be encoded is the polarization state. The mathematical description of a polarization state was developed by Stokes [36], Poincaré [37] and Jones [38], and can be fully summarized by knowledge of the 4 Stokes parameters. The first Stokes parameter S_0 corresponds to the total intensity of the signal, while the three remaining parameters S_1, S_2 and S_3 indicate intensity differences in the horizontal, diagonal and circular polarization bases, respectively. Experimentally, the Stokes parameters can be retrieved by acquiring a sequence of signals that is filtered in polarization by using specific combinations of a quarter wave plate (QWP) and linear polarizer (LP) [39, 40], as depicted in Figure 1.5e.

1.3.3 Shaping the illumination

We have already seen that nanoparticles and metasurfaces offer an excellent toolkit to structure the local electromagnetic environment on the nanoscale. However, there is also an untapped potential in structuring the degrees of freedom of the incident probe illumination, *before* interaction with the sample. Indeed, if we consider the illumination to be a propagating visible laser beam, there are millions of transverse modes of radiation per square milimeter [41], offering an enormous possibility for the optical metrology community to optimize their measurement protocol. Indeed, advances in the field of structured light [42, 43] have developed an immense toolkit to structure an incident illumination in either amplitude, phase, polarization or spectral degrees of freedom.

An example of how the amplitude or phase of an incident light probe can be spatially structured is by a technique called wavefront shaping, as visualized in Figure 1.6a. Here, a plane wave originating from a coherent light source is incident upon a spatial light modulator [44] (SLM), which is a device capable of applying phase modulations onto the incident wavefronts with extremely high resolution. An SLM makes use of the birefringent properties of liquid crystals, which induce a varying optical path length difference depending on the rotation angle of the cystals and can be precisely controlled by electrodes. Although an SLM is a phase-only modulator, other devices such as the digital mirror device [45, 46] (DMD) offer amplitude modulation capabilities as well, and several advanced techniques have been developed that allow for full complex modulation possibilities [47, 48] using these devices. Wavefront

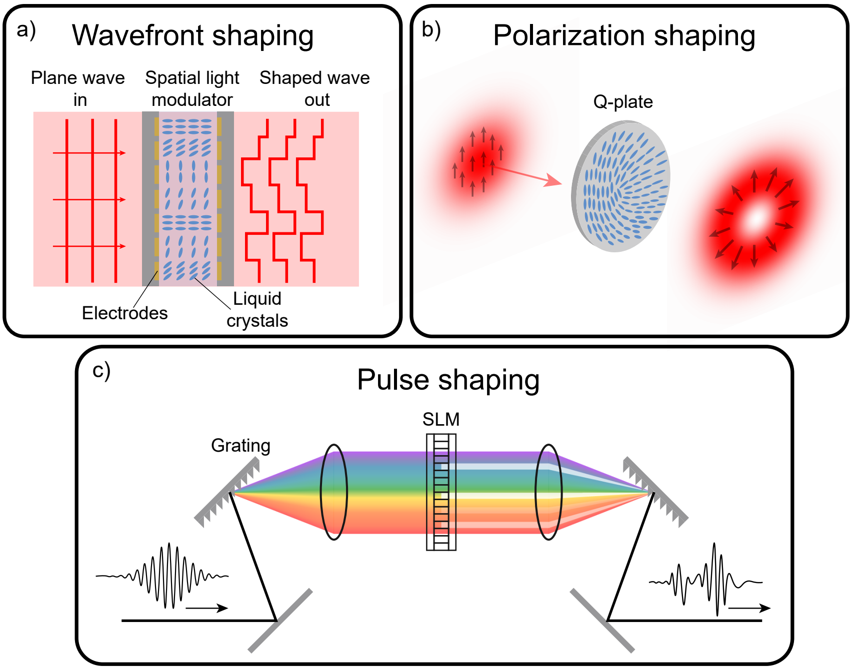

Figure 1.6: Structured illumination techniques (A) A birefringent liquid crystal based spatial light modulator modulates the phase of an impinging planar wavefront. (B) A Q-plate generates complex polarization structuring of an incident linearly polarized beam. (C) Excitation shaping in the time domain by modulating the spectral components of an ultrafast laser pulse.

shaping is a young and active field [49], and its main objective is to understand and control light propagation in complex media. Its origins can be traced back to 2007, when it was demonstrated that light can be focused to a diffraction-limited spotsize behind a strongly scattering disordered medium by controlling the phase of over a thousand incident wavefronts [50]. Currently, the field has reached a maturity level that spans the application domains of imaging through disordered environments [51, 52], focusing *inside* complex media [53], fluorescence microscopy [54, 55], endoscopy with multimode fibers [56, 57] and reservoir computing [58].

The modulation capacities provided by wavefront shaping generally apply to a single polarization channel only. Spatially shaping the polarization distribution of an incident beam in itself provides an additional tuning knob in structured illumination engineering. This can be achieved with q-plates [59], which are birefringent liquid crystal-based devices in which the angle α of the molecular director rotates in the azimuthal direction ϕ, as visualized in Figure 1.6b. Q-plates are characterized by a topological charge q, which indicates the number of times the molecular director rotates in a full 2π azimuthal cycle (q=1/2 in Figure 1.6b), and, similar to SLMs, by a phase retardation δ that can be tuned dynamically by a applying a voltage. Q-plates were initially proposed as wavefront shaping devices to efficiently generate beams carrying phase vortices, which are also known as orbital angular momentum beams [60]. Later, it was discovered that if particular polarization states are used as input beams, in combination with specific Q-plate retardances, a plethora of complex polarization distributions in the output beam [61] can be engineered. Figure 1.6b shows the example of converting a linearly polarized input beam into a radial polarization vector beam, which contains a singularity in the center. These spatially non-uniform polarization vector beams already proved advantageous in generating a sharper focus [62], microscopy [63] and optical trapping of particles. [64]

In the examples discussed thus far, structuring the illumination is limited to the planar spatial domain perpendicular to the propagation direction of the beam, which is also known as 2D structured light. While this is the main structured illumination strategy used in this thesis, it is worth mentioning that there are advances towards 3D [42], and even 4D (3D spatial plus temporal dimensions) structured light as well [65, 66], which pave the way towards ultimate spatio-temporal control of light fields [67]. An example of how an illumination can be shaped in the time domain is shown in Figure 1.6c. Here, the spectral components of an ultrafast (femto or pico second) laser pulse are modulated by positioning an SLM between two gratings in a so-called 4f shaping setup [65, 66]. Because the spectral and temporal domains are connected by a Fourier transform, arbitrary ultrafast pulse packets, limited by the spectral bandwidth of the pulse, can be designed. Examples of application domains where adaptive pulse shaping is relevant include pulse propagation in optical fibers [68] and coherent control of light-matter interactions [69].

1.3.4 Information efficient metrology

The semiconductor industry already uses many techniques discussed in the previous section in commercially available instruments to efficiently extract information from nanoscale environments. For instance, nanometer-scale critical dimension (CD) variations of the devices on a chip can currently be directly imaged by scanning electron microscopy (SEM). Here, the low effective wavelength of high-energy incident electrons results in a sufficient imaging resolution to resolve feature sizes as low as 0.5 nm [70]. Although effective, SEM requires relatively long integration times to obtain images with an acceptable SNR, which comes at the cost of inspection throughput. In addition, the high-energy incident electrons can degrade the quality of the photo resist layer [71]. Fortunately, many techniques based on optical scatterometry have been developed that can retrieve metrology precisions similar to SEM, without the need for direct imaging. To this end, during a typical microchip fabrication cycle, various optical scattering sensors are patterned in devoted areas of the production wafer, as visualized in Figure 1.7a. Because the scattering sensors are patterned during the same exposure as the actual microchips, fabrication parameters such as CD variations, side wall angles, and overlay (OV) errors between device layers in both the microchip and the scattering sensors are strongly related to each other. Optical scatterometry experiments can then be performed on the scattering targets, from which all relevant fabrication parameters are estimated. Figure 1.7b shows an example of how spectroscopic scatterometry retrieves the CD and the angle of the side walls θ in devices [10]. A broadband source illuminates a periodic grating pattern at a fixed angle of incidence, after which the back reflected spectrum is measured on a spectrometer. The unknown CD and θ can then be recovered from the measured spectrum by using inverse reconstruction algorithms in combination with a calibration library of grating spectra at various known CD and θ. Figure 1.7c shows a diffraction-based approach to estimate overlay errors between device layers on a chip. Two gratings are patterned on top of each other in consecutive exposure steps, after which a coherent light source illuminates the stack. The gratings will diffract light into a +1, 0 and -1 diffraction orders, and any imbalance in OV will translate into an imbalance in diffracted intensities between the +1 and -1 orders, from which the unknown OV can be deduced [72]. Although these techniques achieve sub-nanometer precisions at 100 ms integration times, continuous innovation is required to keep up with the increasing fabrication demands within the semiconductor industry.

Many academic research teams have already made significant efforts towards the development of innovative measurement schemes that extract maximum information about parameters in nanoscale environments. For example, the authors of Ref. [73] used concepts from information theory to design

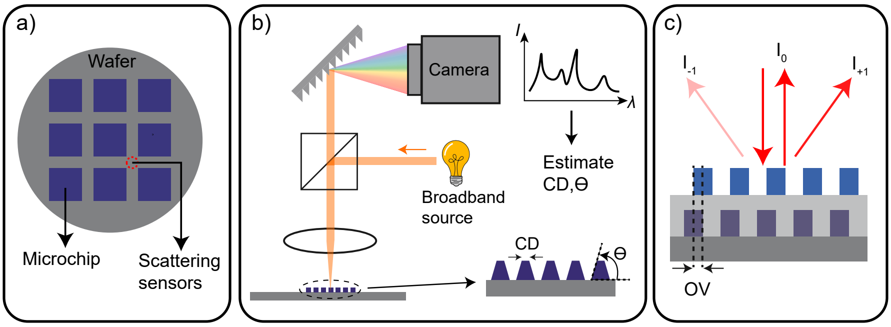

Figure 1.7: Optical scatterometry in semiconductor metrology. (A) Scattering sensors are printed on devoted areas on the wafer during the same exposure as the actual microchips. (B) Spectroscopic scatterometry to estimate CD and θ, inspired from [10]. (C) Diffraction based overlay metrology.

a detection scheme for optimum 3D localization of nano objects. For this, they generated a point spread function (PSF) with maximum Fisher information about the 3D spatial coordinates by modulating the phase of the acquired Fourier space. On the side of the illuminations, the wavefront shaping community has recently introduced the concept of "maximum information states" [74], which are specific modes of illumination that generate maximum Fisher information about parameters in complex and disordered systems. Structured illumination strategies have also been exploited to perform metrology on individual nanoparticles. The authors of Ref. [75] used vector polarization beams to selectively excite multipolar resonances that directionally scatter light as a function of the relative position of the particle with respect to the beam, which can be read out using Fourier microscopy. Aside from resonances in nanoscale objects, the metasurface toolbox offers a wide range of other mechanisms that can be exploited for informative metrology. For instance, the authors of Ref. [76] designed a metasurface in combination with an interferometric detection scheme that generates and detects specific singularities, which can be used as an "optical ruler" with a resolving power of 1 nm. These examples highlight the enormous possibilities that nanophotonic mechanisms and wavefront shaping, in combination with a suitable detection scheme, may add to the semiconductor metrology toolbox. Furthermore, the examples from Refs. [75] and [76] also show that optimizing multiple elements of a measurement concurrently, such as the sample and the detection scheme, can greatly enhance the measurement precision of the relevant nanoscale parameter.

1.4 This thesis

In the metrology examples discussed in the previous section, usually one, or at most two, of the three key ingredients of a measurement protocol are optimized to retrieve maximum information about a parameter. Developing metrology platforms in which all three ingredients are optimized simultaneously are, however, hardly explored, and would pave the way towards optimally informative nanoscale metrology. The work performed in this thesis is motivated by this challenge, and attempts to combine expertise from the fields of wavefront shaping, metasurfaces, Fourier scatterometry and information theory to develop information efficient nanoscale metrology platforms. The thesis is organized according to the following outline:

Chapter 2 describes a metasurface based metrology protocol in which displacement information on the nanoscale is transduced into specific polarization signatures in the diffracted signal of the metasurface. We provide a theoretical description of the scattering properties of the metasurface sensor, which rely on the physics of Pancharatnam-Berry and detour phase shifts. We demonstrate experimentally that the metasurface, in combination with a suitable polarized illumination and a Fourier space polarimetric readout scheme, is capable of resolving single-digit nanometer structural displacements within the plane of the metasurface. Finally, we use information theoretical arguments how the metasurface could be further optimized.

In **Chapter 3** we experimentally investigate different detection strategies to extract maximum information from a quasi-BIC metasurface scattering sensor. Specifically, we compare the conventional approach of detecting perturbations by analyzing shifts in spectral lineshapes, in which the signal is usually integrated in Fourier space, to an angle-resolved Fourier space measurement. We demonstrate that perturbations in the quasi-BIC metasurface can lead to resonant directional scattering effects that enhance the Fisher information content by a factor of 7 with respect to conventional approaches.

Chapter 4 we theoretically explore how structured illumination schemes can increase the information scattered by quasi-BIC metasurface sensors. We utilize the sensing platform discussed in **Chapter 3**, equipped with wavefront shaping capabilities in the excitation, and show that structured illuminations can lead to selective modal excitations that are incompatible with trivial illumination schemes. We further show that these selective excitations can provide more information about a nanoscale perturbation than conventional excitations.

In **Chapter 5**, we experimentally report how wavefront shaping of an incident beam, in combination with suitable sample engineering on the nanoscale, leads to optimum extinction conditions in individual nanoparticles. We fabricate plasmonic nanoparticle arrays with different array sizes separated from a mirror by a dielectric spacer layer of variable height, and investigate the extinction properties as a function of both spacer height and particle array size, all the way towards a single nanoscatterer. We demonstrate that the phase of the incident wave vectors of a tightly focused beam should be matched to the scattered phase of a nanoparticle-on-mirror to achieve optimum extinction, connecting the notions of time reversal in wave scattering to nanoparticle extinction.

Chapter 2

Nanometer Interlaced Displacement Metrology Using Diffractive Pancharatnam-Berry and Detour Phase Metasurfaces

Resolving structural misalignments on the nanoscale is of utmost importance in areas such as semiconductor device manufacturing. Metaphotonics provides a powerful toolbox to efficiently transduce information on the nanoscale into measurable far-field observables. In this chapter, we propose and demonstrate a novel interlaced displacement sensing platform based on diffractive anisotropic metasurfaces combined with polarimetric Fourier microscopy capable of resolving few nanometer displacements within a device layer. We show that the sensing mechanism relies on an interplay of Pancharatnam-Berry and detour phase shifts, and argue how nanoscale displacements are transduced into specific polarization signatures in the diffraction orders. We discuss efficient measurement protocols suitable for high speed metrology applications and lay out optimization strategies for maximal sensing responsivity. Finally, we show that the proposed platform is capable of resolving arbitrary two-dimensional displacements on a device.

2.1 Introduction

The field of optical metrology [77, 78] covers a range of measurement techniques in which light is used as the main information carrier, finding applications in for instance superresolution imaging [79–81], gravitational wave detection [8] and medical diagnostics [82]. In these technologies, a physical property of an object or specimen affects fundamental properties of an electromagnetic wave, such as polarization, amplitude, phase or propagation direction, which is subsequently read out in a suitable measurement protocol. In optical metrology, the goal is to gather as much information as possible about this single unknown property of interest, while assuming prior knowledge and control over all other relevant parameters. By virtue of this prior knowledge, the single unknown parameter can be deduced with deeply subwavelength resolution, which highlights a crucial difference between the fields of optical metrology and imaging, where in the latter no such prior knowledge is assumed at the cost of a resolution bound defined by the diffraction limit. Optical metrology techniques to measure spatial positions, displacements, sizes and shapes on the nanoscale are therefore an indispensable tool in modern day semiconductor device manufacturing processes [83]. Nanoscale structures which are lithographically defined in a resist and subsequently transferred into a device wafer, are routinely checked for potential fabrication mishaps such as defects, relative alignment errors between devices and device layers, surface roughness [10, 84], size variations that might occur due to overexposure or overetching, and shape errors. To keep up with the exponentially decreasing trend in the feature size of these structures, known as Moore's law [9], there is a stringent need for refined and highly sensitive nanoscale optical metrology platforms. Indeed, the yield of advances in lithography is directly dependent on the availability of rapid, non-invasive metrology that is pertinent for the dimensions of the lithography process at hand. There is thus a very large interest in performing optical metrology with subnanometer resolution, but using visible optical wavelengths.

The field of nanophotonics excels at controlling light-matter interactions, scattering and diffraction from nanoscale structures [13]. Thereby, it holds an important role in refining the capabilities of optical metrology. Optical metrology poses the interesting design question which scattering structures and scattering mechanisms provide the most sensitivity to a metrological parameter of interest, and which read-out scheme is optimal for a given scattering structure. At the same time, the field of nanophotonics develops new microscopy techniques such as superresolution localization microscopy [79, 80, 85–87], Fourier microscopy [40, 88, 89], and microscopy with structured light [90, 91] that may be leveraged for metrology. As examples of works on the interface of metrology and nanophotonics, indeed, single nanoparticles and oligomers of nanoparticles have proven to be excellent displacement sensors by exploiting the nanoscale interactions between a structured optical field with underlying resonant modes in the nanoparticles [75, 92, 93], exemplifying the potential of plasmonic and Mie resonances. Metasurfaces are 2-dimensional dense arrays of individually tailored sub-wavelength designer building blocks [17], and can be used to alter fundamental properties of an impinging electromagnetic wave at will [94, 95]. This flexible engineering at the nanoscale has already been leveraged in several optical metrology scenarios. For instance, if the relevant property to be estimated is an overall displacement of a specimen relative to a reference platform, Yuan et. al. [76] reported a metasurface that generates electromagnetic fields with strong phase gradients that may serve as deeply subwavelength markers on a ruler, containing sub-nanometer displacement resolving power. This approach of strong phase gradients and singularities can also be used with random speckle patterns that can be generated in multimode fiber probes [96]. Zang et. al. [97] reported a nanometric displacement platform in which absolute metasurface displacements are transduced into polarization rotations, which are subsequently converted into measurable intensity differentials.

In this chapter, we propose Pancharatnam-Berry metasurfaces for so-called 'interlaced metrology.' Interlaced metrology is a branch of semiconductor optical metrology that retrieves potential misalignments between structures and devices that are written in a multistep lithography process, but in the same device layer. For such a metrology usecase, typically devoted scattering targets are printed as telltale sensors onto every writefield of a device wafer. These targets are designed to be used in combination with diffraction based readout techniques [72, 98] to sense potential intralayer displacements between nanostructures. A typical approach is that the scattering targets are conventional diffraction gratings consisting of lines or grooves where a first set of lines is written in the first exposure, while in the second exposure a second set of lines is defined to appear inbetween the first set. The task of interlaced metrology is to resolve sub-nanometer displacements of the second set of lines relative to their nominally ideal position as referenced to the first set of lines. This capability often depends on a very precise dictionary of computed or measured scattering efficiencies versus displacement. Such structures do not exploit the full potential of the nanophotonic toolbox. In this work, we present a novel nanometer interlaced metrology sensing platform based on diffractive metasurfaces consisting of anisotropic birefringent meta-atoms. The main idea is to combine two mechanisms to program geometrical sensitivity onto diffraction efficiencies: these are the Pancharatnam-Berry phase [99–102] on one hand, and the socalled detour phase [103] on the other hand. The detour phase effect is well known in grating physics [103] and computer hologram design [103–105] and was introduced to the metasurface community by Khorasaninejad et al. [106]. It is an effect wherein meta-atom displacements relative to an underlying periodic lattice induce displacement-dependent phase shifts in scattering. The use of birefringent meta-atoms allows to use the Pancharatnam-Berry phase to magnify the visibility of the displacements. Upon excitation with circularly polarized light, the Pancharatnam-Berry phase principle efficiently transduces interstructural displacement information into measurable polarization splittings in the far field diffraction channels. In contrast with existing displacement sensing platforms, our concept is fully generic and does not rely on meticulous meta-atom designs to obtain the desired signal. Practically any material of choice could be used, with the only requirement a structural form birefringence within the meta-atoms. No complex experimental setups or structured illumination conditions are required, a standard Fourier microscope equipped with polarizing optics is sufficient for a successful measurement. In fact, our method can be directly implemented within existing state of the art commercial diffraction based metrology systems [10]. The specific polarization signature has the additional advantage that the optical signal can be accurately nulled by polarization analysis, and can therefore provide a background free response. We propose a simple theoretical model elucidating the sensing mechanism and demonstrate all the qualitative expectations of this model experimentally by performing polarimetric measurements on anisotropic diffractive metasurfaces fabricated from all-dielectric silicon meta-atoms. We show that the polarimetric response encodes deeply subwavelength displacements, and we analyse efficient sensing scenarios capable of resolving nanometer scale displacements, in line with modern day semiconductor metrology standards. We finally discuss strategies to optimize metasurfaces for maximal sensing performance in the sense of presenting the highest Fisher information assuming shot noise limited readout. We show proof-of-concept experiments in which the metrology platform is extended towards two-dimensional interlaced displacement sensing.

2.2 Theoretical concept

Figure 2.1 elucidates the main idea of this work: we consider metasurfaces consisting of alternating lanes of birefringent meta-atoms, where from lane to lane the meta-atoms are rotated by 90 degrees. Upon circularly polarized excitation, the grating diffraction orders must be polarized with an opposite handedness with respect to the excitation if the alternating lanes are exactly equally spaced, a fact which underlies the design philosophy of Pancharatnam-Berry phase metasurfaces. Any displacement Δx of one set of lanes relative to the other set will cause additional symmetry broken phase shifts $\varphi(\pm\Delta x)$ between the orthogonal polarization components within the diffraction orders as a consequence of the so-called detour phase mechanism, which will in turn lead to a detectable splitting in polarization ellipticity between the two diffraction orders. To bring out these two mechanisms, we describe our diffractive metasurfaces as arrays of polarizable scattering meta-atoms, which are positioned in a lattice with interparticle spacing a as depicted in Figure 2.2a. The total

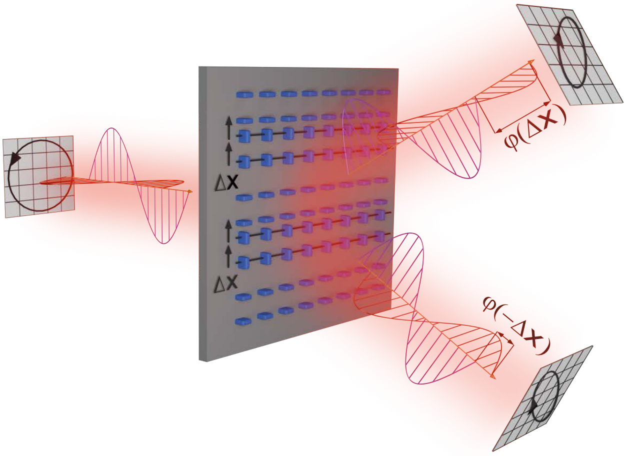

Figure 2.1: Concept of the metasurface interlaced displacement sensor. A metasurface consisting of alternating lanes of anisotropic meta-atoms is excited by a circularly polarized plane wave. Deeply subwavelength displacements between the lanes of the metasurface lead to an interplay of Pancharatnam-Berry and detour phase shifts in the diffraction channels, which result in a detectable splitting in ellipticity between the diffraction orders.

periodicity P is equal to $P = Na$, depending on the number of participating meta units N per unit cell, which is chosen such that it will generate diffraction orders. In this work we limit ourselves to unit cells of 50% duty cycle, meaning that a lane of $N/2$ anisotropic meta-atoms of one orientation is combined with a second lane of $N/2$ meta-atoms that are 90 degree rotated but otherwise identical. An in general unknown displacement Δx will be imprinted on the lanes of rotated meta-atoms, which is the quantity we would like to retrieve by measuring the polarization state of the diffraction orders.

The scattering properties of an isolated meta-atom are modelled by an electric dipole polarizability tensor $\begin{pmatrix} \alpha_L, 0 \\ 0, \alpha_S \end{pmatrix}$, with α_L and α_S the polarizabilities of the scatterer along the long and short axis respectively, accounting for linear birefringence. The polarizability in the out-of-plane dimension is omitted from the formalism, as the normally incident field has no out of plane component. It can be shown (see supplementary information) that the scattered fields of this anisotropic metagrating in the m'th diffraction order in Fourier space can be described by the following expression

$$\mathbf{E}_{\text{out}} \propto \left[\begin{pmatrix} \alpha_L, 0 \\ 0, \alpha_S \end{pmatrix} + e^{im(\pi + 2\pi \frac{\Delta x}{P})} \begin{pmatrix} \alpha_S, 0 \\ 0, \alpha_L \end{pmatrix} \right] \mathbf{E}_{\text{in}}, \tag{2.1}$$

This expression is derived under two assumptions. First, we assume the 1st Born approximation, essentially ignoring multiple scattering between meta-atoms. Secondly, we assume that individual meta-atoms radiate their electric far-field parallel to their dipole moment, which is strictly true only in the paraxial limit of small diffraction angles. Both assumptions could be relaxed by including Ewald lattice sums to deal with meta-atom interactions [107], and by including an orientation dependent matrix as prefactor to the right-hand side to account for the high-angle dipole radiation pattern. The scenario of zero displacement $\Delta x = 0$ would result in a phase factor of π in the second expression. The condition of non-birefringent meta-atoms ($\alpha_L = \alpha_S$) leads to a vanishing of the diffractive signal. This is immediately evident since in this scenario only the lattice with sub-diffractive spacing a is left. As soon as the meta-atoms are birefringent, or as soon as a displacement Δx is introduced, diffraction can occur.

Next, we consider excitation of the metasurface by a circularly polarized plane wave with polarization state described by the Jones vector $\mathbf{E}_{\text{in}} = \frac{1}{\sqrt{2}}(1, \sigma)$, with $\sigma = \pm i$ for RCP and LCP (right- resp. lefthanded circular polarization) illumination respectively. Supposing we inspect only the ± 1 diffraction orders, the diffracted fields can be written as

$$\mathbf{E}_{\text{out}}(\pm 1) \propto \begin{pmatrix} \alpha_L - \alpha_S e^{\pm i 2\pi \frac{\Delta x}{P}} \\ \sigma(\alpha_S - \alpha_L e^{\pm i 2\pi \frac{\Delta x}{P}}) \end{pmatrix}. \tag{2.2}$$

Notice here how a nonzero displacement Δx introduces a phase slip of $\frac{\Delta x}{P}$ to the diffracted fields, which is opposite in sign for the $\pm$1st orders. This phase shift, which is related to the concept of detour phase [104, 105], thus transduces displacement information in the metasurface plane to polarization information in Fourier space, and is the main carrier of displacement information.

To clarify how the Pancharatnam-Berry phase is leveraged to encode displacements in the polarization state of diffracted orders, we project Eq. (2.2) onto a detection basis of circular polarization using Jones calculus. This leads to the circularly co-polarized and cross-polarized signals relative to the incident handedness

$$\mathbf{E}_{\text{circ. co-polariz}} \propto (\alpha_L + \alpha_S)(1 - e^{\pm i 2\pi \frac{\Delta x}{P}}), \tag{2.3}$$

$$\mathbf{E}_{\text{circ. cross-polariz}} \propto (\alpha_L - \alpha_S)(1 + e^{\pm i 2\pi \frac{\Delta x}{P}}). \tag{2.4}$$

Notice here that for $\Delta x = 0$, only cross-polarized diffraction is present with respect to the excitation field, with a diffraction strength proportional to the linear birefringence. Diffraction in this regime is purely due to the Pancharatnam-Berry (PB) phase [99, 100], which is a geometric phase which encodes phase shifts purely onto circular polarized states of light with an opposite handedness with respect to driving fields. For non-zero values of Δx, a co-polarized diffraction component is present in the diffracted signal, which can be read out in a polarimetric measurement scheme. A clear indication that this polarimetric scheme can have a sensitivity advantage is that this co-polarized displacement dependent signal occurs on top of a zero-background signal at $\Delta x = 0$.

To elucidate the diffractive properties of the anisotropic metasurface that is contained in the preceding analysis, we plot the full polarization state of the two diffracted channels on the Poincaré sphere for two scenarios. First, in Figure 2.2b, the polarization states of the ±1st orders are plotted versus the normalized displacement parameter $\Delta x/P$ and at a fixed birefringence defined by the polarizability ratio α_L/α_S (set to 3 for this example). For $\Delta x/P = 0$, the polarization states of the two diffraction orders are equal, with a purely circular polarization state with opposite handedness with respect to the excitation, which is due to the aforementioned Pancharatnam-Berry phase. For increasing values of $\Delta x/P$, the polarization states of the diffraction orders split in opposite directions on the Poincaré sphere, which is due to displacement induced detour phase shifts in Eq. (2.2). This combination of Pancharatnam-Berry and detour phase shifts thus allows for a unique encoding of potential deeply subwavelength displacements within the plane of the metasurface onto the diffracted polarization states.

To highlight the polarization dependence as a function of the linear birefringence of the meta-atoms, we show the polarization dependence as function of the polarizability ratio α_L/α_S for a fixed displacement $\Delta x/P = 0.1$ in Figure 2.2c. Here, the interplay between Pancharatnam-Berry and detour phase shifts becomes evident. When no birefringence is present in the meta-atoms ($\alpha_L/\alpha_S = 1$), the polarization state of the diffraction orders retains the same handedness state as the excitation field, which is the regime of pure detour phase diffraction, as is also evident from Eqs. (2.3) and (2.4). As the birefringence increases, a cross-polarized contribution is added to the diffracted signal, again resulting in a splitting towards the opposite pole of the Poincaré sphere.

2.3 Experiment

For an experimental realization of the polarimetric displacement sensor, we have fabricated silicon metasurfaces with anisotropic meta-atoms by electron beam lithography (see Appendix B for design and nanofabrication details). The dimensions are chosen such that the meta-atoms act as effective half-wave retarders. This design replicates a meta-atom design by Wang et al. [108] for PB-phase based metasurfaces, and the design choice maximizes the PB phase conversion efficiency and thereby fixes the linear birefringence. We note that this is by no means an optimized design for metrology, and discuss potential routes for metasurface optimization in a later section. We fabricated several versions of this anisotropic metasurface with different values of the

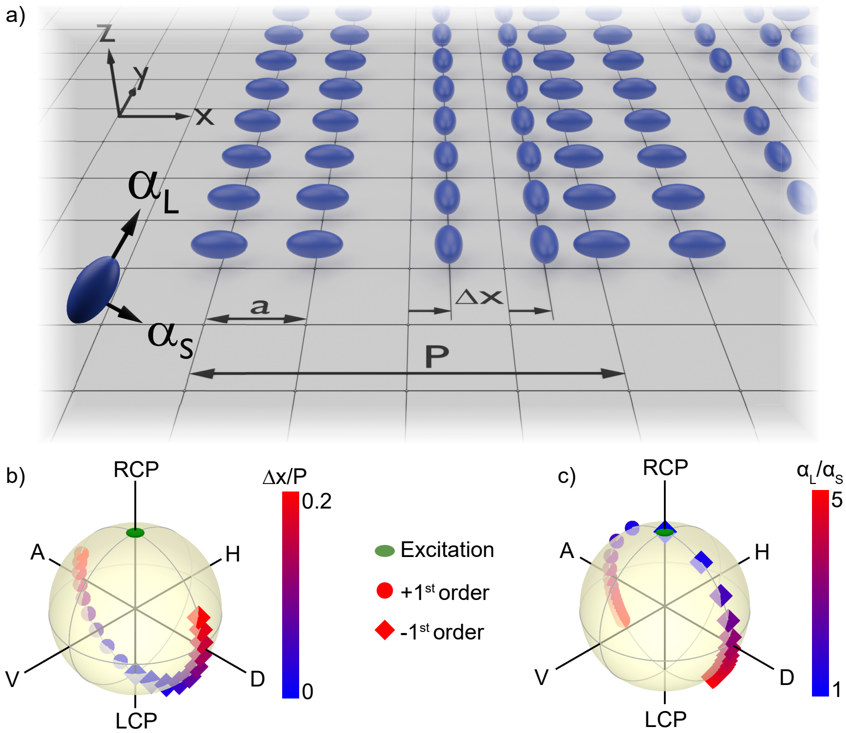

Figure 2.2: Analytical calculations on anisotropic metagratings show polarization splitting in diffraction orders. Panel (a): Schematic illustration of the metasurface interlaced displacement sensor. Panel (b): Polarization state of the diffraction orders as function of the normalized displacement $\frac{\Delta x}{P}$ for fixed polarizability ratio $\frac{\alpha_L}{\alpha_S} = 3$. Panel (c): Polarization state of the diffraction orders as function of the polarizability ratio $\frac{\alpha_L}{\alpha_S}$ for fixed normalized displacement $\frac{\Delta x}{P} = 0.1$. The green dot highlights the polarization state of the excitation beam.

displacement Δx. Scanning electron microscope images of typical devices with $\Delta x = 0$ nm and $\Delta x = 120$ nm are shown in Figure 2.3b. To analyze the polarization state of the diffraction orders, we utilize Fourier space polarimetry [40], with a typical experimental setup shown in Figure 2.3a. In this technique, the back-focal-plane (BFP) of a microscope objective is imaged onto a CMOS camera, which retrieves the Fourier space of the scattered light from the metasurface and therefore directly images the discrete diffraction channels. A combination of linear polarizers and quarter wave plates in both the input beam and detection path provide control over the polarization state of the input beam which illuminates the metasurface, and provide the means to interrogate the full polarization state of the scattered signal through Stokes polarimetry. The Stokes parameters S_0, S_1, S_2 and S_3 are determined by

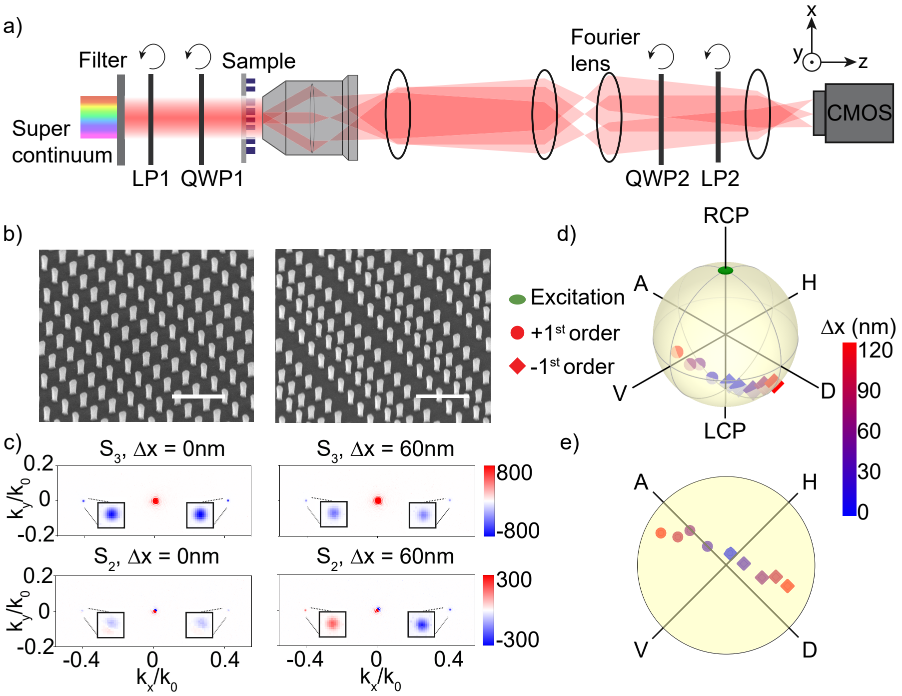

Figure 2.3: Experimental realization of the PB/detour metasurface interlaced displacement sensor. Panel (a) Fourier space polarimetric microscope for reading out the polarization state of the metasurface. LP: linear polarizer, QWP: quarter wave plate. Panel (b): Tilted view (tilt angle: 45°) scanning electron microscopy images showing undisplaced ($\Delta x = 0$ nm, left) and displaced ($\Delta x = 120$ nm, right) lanes of a metasurface containing anisotropic meta-atoms. The scalebar corresponds to 1 μm. Panel (c): Third and second Stokes parameters of the diffraction orders of a metasurface with $\Delta x = 0$ nm (left) and $\Delta x = 60$ nm (right). Panel (d): Full polarization state of the diffraction orders of the metasurface as function of Δx. The green dot highlights the polarization state of the excitation beam. Panel (e): 2 dimensional projection of the data in panel (d) onto the lower hemisphere of the Poincaré sphere.

acquiring 6 intensity images for different configurations of the collection linear polarizer and quarter wave plate, following the protocol outlined in [40]. The first Stokes parameter S_0 corresponds to the total intensity of the acquired signal, while the remaining three Stokes parameters report intensity differentials between orthogonal polarization states: S_1 for the horizontal/vertical basis, S_2 for the diagonal/anti-diagonal basis and S_3 for the left handed/right handed circular basis.

In the following experiments, we perform Fourier space polarimetry at a wavelength of 650 nm using metasurfaces with interparticle spacing $a = 400$ nm and 4 meta-units per unitcell ($N = 4$). In Figure 2.3c, raw images of the Stokes parameters S_3 and S_2 of the diffraction channels of unperturbed (Δx

= 0 nm, left) and perturbed (Δx = 60 nm, right) metagratings are shown. First, we note that the S_3 parameter of the ±1st diffraction orders at zero displacement is fully sign reversed with respect to the direct transmission of the beam through the sample. This observation highlights the PB phase shift due to the anisotropic meta-atoms. Since at zero displacement these orders are fully circularly (cross-) polarized, they carry no preferential linear polarization, leading to a null-signal in S_2. In contrast, for the displaced version of the metasurface the S_2 parameter shows a strong diffraction signature. This splitting in S_2 is precisely due to the additional detour phase shift provoked by the inter-structural displacements in the plane, as predicted by our model, causing marked ellipticity. The non-zero S_2 parameter not only directly visualizes that there is a non-zero displacement Δx but also through its sign directly reveals the direction of the shift.

To summarize the complete polarization dependence as a function of displacement, we show the measured polarization state of the diffraction orders for metasurfaces with different values of displacement on the Poincaré sphere in Figure 2.3d. Here, we recover the same trend of polarization splitting as predicted by our model in Figure 2.2b. We also note here that the trajectory of the measured splittings on the Poincaré sphere is not exactly in the $S_1 = 0$ plane, and after a 2D projection of the datapoints onto the lower hemisphere of the Poincaré sphere in Figure 2.3e an additional minor splitting is clearly present in the S_1 parameter as well. This can be explained by the fact that slight deviations from the ideal half-wave retarder condition in the Si meta-atoms causes an additional phase lag between the scattering polarizabilities α_L and α_S, leading to non-symmetric splitting effects on the Poincaré sphere (see supplementary information).

2.4 Metrology and responsivity

While analyzing excursions of the diffracted orders on the Poincaré sphere highlights the essential physics of encoding displacements through detour and PB phase, it arguably does not constitute a practical measurement scheme for metrology. In this section, we analyze polarimetric measurement schemes that are more applicable in an interlaced metrology scenario. Current day requirements for semiconductor interlaced metrology involve displacement sensitivity down to the nanometer scale, while maintaining a high inspection throughput, corresponding to measurement times of approximately 100 ms per target [10]. Reading out the full polarization state by sequential image recordings using mechanically rotating polarizing optics is in that context not very practical. A fast readout scheme using specific combinations of QWP2 and LP2, which optimally converts the polarization characteristics into intensity differentials is, therefore, desirable.

To investigate optimal measurement protocols, we measure diffraction intensities of the metagratings by keeping the incident polarization circular and fixed, while on the analysis side fixing the angle of the quarter wave plate QWP2 to 45° relative to the y-axis in Figure 2.3a, while rotating the angle of the linear polarizer LP2 from 0° to 180°. The results of this measurement are shown in Figures 2.4 for metasurfaces with encoded displacements of $\Delta x = 0$ nm in panel (A), $\Delta x = 4$ nm in panel (B), $\Delta x = 8$ nm in panel (C) and $\Delta x = 60$ nm in panel (D). First, we note that the diffracted intensities follow a sinusoidal behaviour with respect to the angle Θ of LP2, where in the case of $\Delta x = 0$ nm maximum signal is measured when LP2 is fixed at 0° and 180°, while no signal is measured at an angle of 90°. These regimes correspond to circular polarization filtering of respectively the orthogonal and parallel handedness states with respect to the excitation, highlighting the well-known PB phase effect in grating diffraction. Furthermore, a clear symmetrical shift between the sinusoids of the ±1st diffraction orders around $\Theta = 90^\circ$ is observed which increases as a function of Δx. Indeed, fitting our experimental data with a pair of $\sin^2(\Theta)$ functions that are symmetrically shifted relative to the 90° point results in an excellent match. It is easy to verify that the behaviour of these experimental curves is consistent with our simple model by applying Jones calculus to the diffracted fields predicted by Eq. (2.2), as shown for displacement parameters $\Delta x/P = 0$ in panel (E) and $\Delta x/P = 0.1$ in panel (F). These results show that displacements even down to the few nanometer scale can be resolved, and that the displacement is essentially encoded in the fitted shift of the null signal away from $\Theta = 90^\circ$.

For metrology, a suitable estimator needs to be defined which relates displacements within the plane of the metasurface into differentials of measurable observables. To keep up with the speed requirements of modern day interlaced metrology, we propose an estimation scheme relying on acquisition at a single polarizer setting instead of fitting the sinusoidal dependencies evident in Figure 2.4 in full. The idea is to measure at the fixed angle of LP2 at which the maximum intensity difference between the plus and minus first diffraction orders occurs, which by construction is at $\Theta = \pm 45^\circ$ (independent of displacement). For the dataset at hand, the blue datapoints in Figure 2.4g report the intensity difference measured for metasurfaces with different lithographically imprinted displacements. More precisely stated, we work with a normalized intensity difference $\Delta I_\pm$ that divides out absolute intensities and grating efficiencies, defined as

$$\Delta I_\pm = \frac{I_+ - I_-}{I_+ + I_-} \tag{2.5}$$

where $I_\pm$ represent the intensity in the positive and negative diffraction order. For comparison, in the same graph we indicate $\Delta I_\pm$ as extracted from the fit results by red datapoints, where the errorbars are deduced by propagating the errors from individual fitparameters, and achieve a good overlap with the normalized intensities as extracted from the single measurement. Selecting the range $\Delta x \leq 20$ nm, we deduce a responsivity of $\Delta I_{\pm}/\Delta x = (0.99 \pm 0.17)$ percent intensity change per nanometer displacement.

This estimation scheme has, apart from being high speed, several advantages for semiconductor metrology. First, the measurement is inherently self-referencing to potential fluctuations in laserpower or differences in scattering strengths of different metasurface configurations which might cause overall fluctuations in absolute diffracted counts, as is also evident from our measurements. Second, metrology sensors are usually closely surrounded by other structures on the device wafer which might corrupt the sensing signal by scattering crosstalk [109]. Because the relevant signal here relies on specific polarization filtering, we expect the unwanted crosstalk to be effectively filtered out.

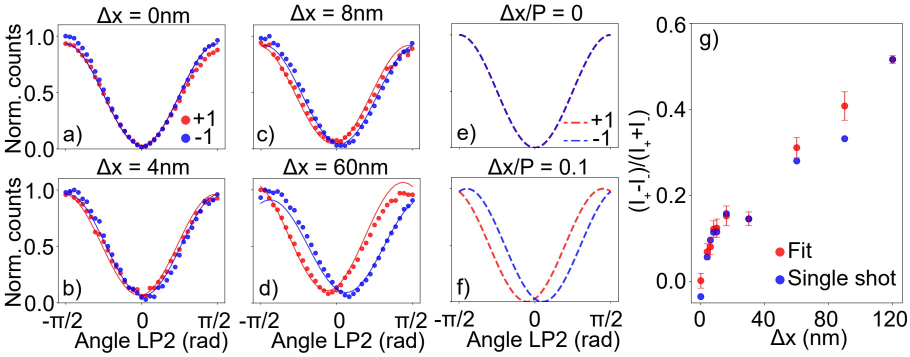

Figure 2.4: Application of the anisotropic metasurface in an interlaced metrology scenario. Measurements and corresponding fits of shifted $\sin^2(\Theta)$ functions of the intensities of the $\pm 1^{st}$ diffraction orders for fixed angle of QWP2 (45°), while rotation the angle Θ of LP2 for a metasurface imprinted by Panel (a): $\Delta x = 0$ nm, Panel (b): $\Delta x = 4$ nm, Panel (c): $\Delta x = 8$ nm and panel (d): $\Delta x = 60$ nm. Panels (e) and (f) correspond to analytical calculations of metasurfaces containing normalized displacement parameters $\frac{\Delta x}{P} = 0$ and $\frac{\Delta x}{P} = 0.1$ respectively. Panel (g): Responsivity of the normalized intensity differential estimator versus metasurface displacement Δx extracted from a single measurement (blue) and the fitresults (red).

All experimental results shown thus far have been conducted with fixed meta-atom polarizabilites satisfying half-wave plate conditions [108], which are optimal for Pancharatnam-Berry metasurface diffraction efficiencies, but which are not necessarily optimal for sensing performance. To investigate how the meta-atoms can be optimized, we turn again to our analytical model and calculate diffraction intensity contrast $\Delta I_{\pm}$ for fixed angles of QWP2 and LP2, as defined for the single shot metrology scenario in Figure 2.4f, and for a fixed normalized displacement parameter $\Delta x/P = 0.01$. For different values of the meta-atom polarizability ratio α_L/α_S, we calculate values of the normalized differential intensity estimator $\Delta I_{\pm}$ and plot the results in the complex polarizability plane in Figure 2.5a. From this figure alone, it might appear that the optimal polarizability ratio approaches unity (no birefringence), where $\Delta I_{\pm}$ results in maximum responsivity. This, however, overlooks the fact that in precisely this regime, the PB diffraction efficiency is minimal, which results in a low number of detected photons and thus a low signal to noise ratio in an experimental setting. This is evident from Figure 2.5b, where we plot the total diffraction intensities of the ±1st diffraction orders. It is thus evident that in light of noise and photon budget there is a tradeoff between optimizing absolute diffraction efficiency on one hand, and the relative contrast ΔI on the other hand.

We use a concept from information theory called ‘Fisher information’ [11] to analyze this tradeoff in light of noise. In brief, the Fisher information quantifies the amount of information a measured dataset contains with respect to a relevant parameter, and puts a bound on the maximum precision with which this parameter can be estimated given a certain noise statistics assumed for the observable at hand. This concept has already been successfully applied in several metrology scenarios, such as optimizing a metagrating for transverse position metrology [110] and finding optimal illumination states in coherent scattering experiments [74]. Assuming for simplicity that photon shot noise is the limiting noise factor, we can derive (see Appendix F) an explicit expression for the Fisher information in our specific measurement protocol according to:

$$F = \frac{1}{I_+}\left(\frac{\partial I_+}{\partial x}\right)^2 + \frac{1}{I_-}\left(\frac{\partial I_-}{\partial x}\right)^2 \tag{2.6}$$

and plot its values in the complex plane of polarizability ratios in Figure 2.5c. Comparing this figure to the regime in which our metasurface operates, which is the negative direction on the real axis of the polarizability ratio (due to the half-wave plate condition), it is seen that the sensing performance of the metasurface can still be optimized substantially. The results presented in this work thus only report a very conservative bound on the displacement resolving power of our metasurface, and we expect that sub-nanometer precision lies within reach.

2.5 2D metagratings

Finally, we show proof of concept experiments in which the metasurface displacement sensing platform is extended towards interlaced metrology along two directions. For this, we fabricated metagratings with diffractive periodicities in both x and y directions as shown in the SEM image in Figure 2.6c and e for an unperturbed ($\Delta x = 0$ nm, $\Delta y = 0$ nm) and perturbed ($\Delta x = 80$ nm, $\Delta y = 0$ nm) respectively, which will now generate diffraction channels along both k_x and k_y directions. In the same way as discussed for the one-dimensional metasurface, arbitrary two-dimensional displacements can be imprinted onto the set of rotated meta-atoms in the unit-cell, which

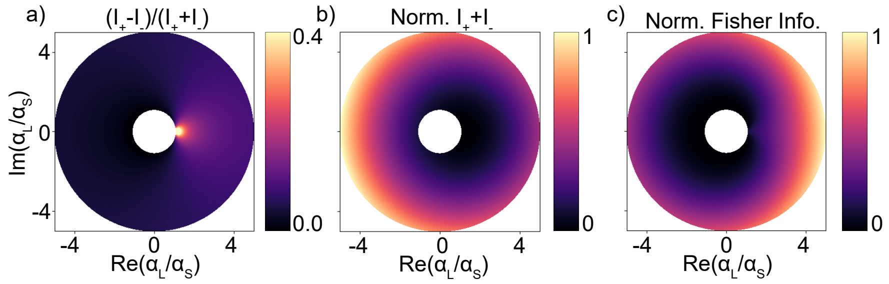

Figure 2.5: Meta-atom optimization and noise considerations. As a function of polarizability ratio $\frac{\alpha_L}{\alpha_s}$, in the complex plane we show: Panel (a): Normalized responsivity parameter $\frac{\Delta I}{I_+ + I_-}$, Panel (b): Diffraction efficiency $I_+ + I_-$ and Panel (c): Fisher information of a measurement while using the readout strategy discussed in the metrology section.

will subsequently lead to detour phase shifts in the diffraction channels along the k_x and k_y directions for displacements in x and y respectively. Figures 2.6a and 2.6b show calculated values of normalized S_3 and S_2 Stokes parameters of a typical Fourier image of such a metasurface containing 2D displacements (with $\Delta x/P = 0.1$, $\Delta y/P = 0.05$), where again the PB-phase shift and polarization splitting are evident in S_3 and S_2 respectively. Because the detour phase shifts, and thereby also the strengths of the polarization splitting, imprinted on the diffraction channels in the k_x (k_y) viewing directions are specifically linked to the 1 dimensional displacement components x (y) within the metasurface plane, complete 2D displacement information can be retrieved from a single polarization resolved measurement by analyzing the set of $(\hat{k}_x, \hat{k}_y) = [(-1,0),(1,0),(0,-1),(0,1)]$ diffraction orders.

To show this directional link between metasurface displacements and polarization splitting in the relevant viewing direction in Fourier space, we perform polarimetric measurements on the four diffraction orders of an unperturbed ($\Delta x = 0$ nm, Figure 2.6d) and perturbed ($\Delta x = 40$ nm, Figure 2.6f) version of a two dimensional anisotropic metagrating, using the same measurement protocol as was used in Figure 2.4. The results again show identical intensity dependencies for the unperturbed metagrating, whereas for the perturbed metagrating only the set of $((-1,0),(1,0))$ orders along the k_x direction show the characteristic shift in intensity curves commensurate with the fact that for this particular sample the displacement vector is nonzero only in the x-direction. This data also shows an overall intensity offset, which we attribute to deviations in the meta-atom dimensions from the half-wave plate condition (see supplementary information). We further note that linear combinations of the displacements Δx and Δy are transduced not only via the lowest diffraction orders, but also into the diagonal diffraction orders $(\hat{k}_x, \hat{k}_y) = [(-1,-1),(1,-1),(1,-1),(1,1)]$, which might be analyzed in addition to enhance the signal to noise ratio.

2.6 Conclusions

In conclusion, we proposed a sensing platform which encodes deeply subwavelength displacements within a layer of an anisotropic diffractive metasurface onto the polarization signatures of the diffraction orders. We argued that the sensing mechanism relies on an interplay between Pancharatnam-Berry and detour phase shifts, and demonstrated that displacements down to few nanometers can be effectively resolved. A key advantage of our platform is the background-free nature of the signal. Using a specific polarimetric readout strategy, the signal provides an inherently self-referenced estimator for potentially unknown displacements, which renders the knowledge of experimental parameters such as total laser power, integration time and diffraction efficiencies irrelevant. For an accurate estimation of unknown displacements, however, the polarizability contrasts of the meta-atoms need to be known, which can be inferred from a calibration measurement using a metasurface with a-priori known displacement. This highlights an additional advantage of the sensing platform: at known displacements these structures can also report on the polarization anisotropy and on whether nominally identical but simply rotated polarization anisotropies are indeed identical up to rotation. As such the presented structures could also be used as optical sensors of shape parameters, e.g. as a reporter for anisotropies and astigmatism in lithography. We expect that the responsivity of the metasurface can be optimized substantially by designing anisotropic meta-atoms with giant polarizability ratios, which could be achieved by for instance exploiting the physics of bound states in the continuum [30] or inverse design strategies [111], and believe that subnanometer resolving power lies within reach. We note that both the detour phase and the PB mechanism are fully generic and only require designs that show structural birefringence. Furthermore, the meta-atoms themselves do not require a minimum size or refractive index. As such this approach to metrology can work also on arrays of deeply subwavelength structures within each lane, as long as they present optical form birefringence in an effective medium limit. This is of relevance in semiconductor manufacturing where it is desirable to have metrology target structures that are similar in size to devices at the relevant manufacturing node. Furthermore, we highlight the possibility of extending the method towards aperiodic metrology targets in the form of Pancharatnam-Berry holographic phasemasks, which could provide an information advantage in the far-field polarization signal with respect to the sparse discrete diffraction channels as analyzed in this work. Finally, the concepts of Pancharatnam-Berry phase and detour phase are applicable not only to metrologies within a single layer, and may be advantageously combined with overlay metrologies that aim to resolve lateral displacements between

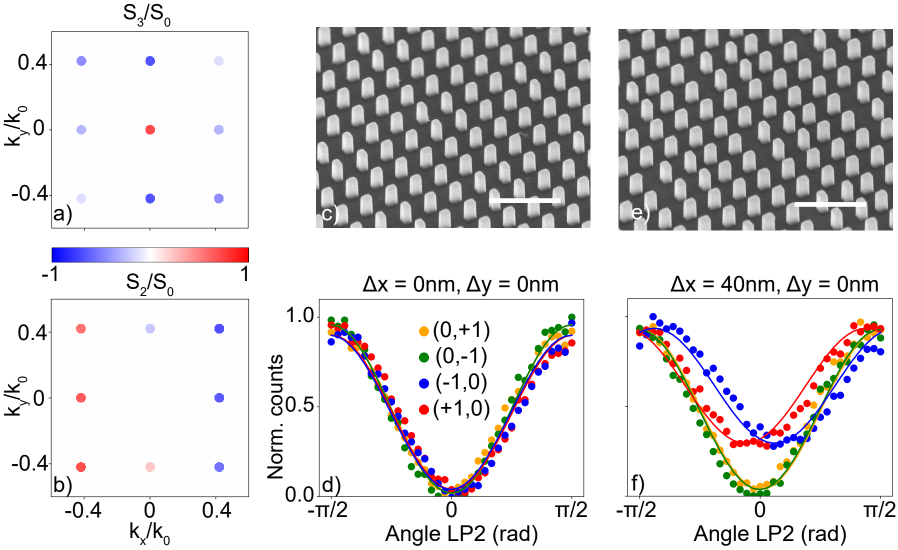

Figure 2.6: Towards 2D interlaced metrology in anisotropic metasurfaces Panels (a) and (b): calculated normalized stokes parameters S_3/S_0 and S_2/S_0 respectively of a 2D anisotropic metasurface ($\frac{\alpha_L}{\alpha_S} = 3$ with $\frac{\Delta x}{P} = 0.1$ and $\frac{\Delta y}{P} = 0.04$). Panels (c) and (e): Tilted view (tilt angle: 45° SEM image of an unperturbed ($\Delta x = 0$ nm, $\Delta y = 0$ nm) and perturbed ($\Delta x = 80$ nm, $\Delta y = 0$ nm) 2D displacement sensing metasurface respectively. The scalebar corresponds to 1 μm. Panels (d) and (f) report measurements on unperturbed ($\Delta x = 0$ nm, $\Delta y = 0$ nm) and perturbed ($\Delta x = 40$ nm, $\Delta y = 0$ nm) version of 2D anisotropic metasurfaces respectively with corresponding fits of shifted $\sin^2(\Theta)$ functions of the intensities of the four diffraction orders for fixed angle of QWP2 (45°), while rotation the angle Θ of LP2.

vertically offset layers. Overall, our work provides a metasurface based platform for retrieving structural misalignments within a device, a highly relevant problem in today's semiconductor manufacturing processes.

Appendices

A Experimental setup

A supercontinuum laser (Leukos Electro-VIS) is monochromated (1nm bandwidth) by an Acousto-Optic Tunable Filter (AOTF) and coulped into a single mode optical fiber. The output of the fiber (power 120 μW) is subsequently collimated by a lens (Thorlabs, AC-254-035-A) and guided through the first linear polarizer (Thorlabs, LPVICS100-MP2) and quarter wave plate (Thorlabs, AQWP05M-600) to obtain circular polarized illumination. After passing through the sample, an objective (NIKON, CFI Achro) captures the diffracted signal and is guided through a telescope consisting of two lenses (Thorlabs, AC-254-050-B). The polarization state of the diffracted signal is then analyzed by the second quarter wave plate (Thorlabs, AQWP05M-600) and linear polarizer (Thorlabs, LPVIS100-MP2). The Fourier plane of the metasurface is finally imaged by a last pair of lenses (Thorlabs, AC-254-200-B) onto a CMOS camera (PCO Panda 4.2). All polarization optics were mounted in motorized (Thorlabs, KDC101) rotation mounts (Thorlabs, PRM1/MZ8). For the Stokes polarimetry measurements in Figure 2.3, the wavelength was set to 630 nm and 20 frames were averaged with an integration time of 150 μs. In the sensitivity measurements in Figure 2.4, the wavelength was set to 650 nm and 20 frames were averaged with an integration time of 20 μs.

B Sample design and nanofabrication

We fabricated Si metasurfaces using electron beam lithography using the following procedure. A fused quartz substrate (Menzel-Gläser) with a thickness of 0.5 mm was sonicated in H_2O for 10 mins and subsequently cleaned in a solution of $NH_4OH/H_2H_2/H_2O = 1/1/5$ (base piranha) at 75°C for 15 mins and, after rinsing with H_2O, blown dry with N_2. 320 nm of amorphous silicon (a-Si) was deposited onto the substrate using physical vapor deposition (Polyteknik Flextura M506 S) at RF power 260 W with corresponding deposition rate of 0.12 nm/s. After an oxygen plasma descum process of 2 mins, a 160 nm layer of hydrogen silsequioxane (HSQ) was spincoated (Süss Microtec Delta 80 spincoater) for 60 s with a speed of 1000 rpm and acceleration of 1000 rpm/s and baked for 2 mins at 180°C. A conductive layer (Espacer 300Z) was spincoated for 60 s with speed 2000 rpm and acceleration 1000 rpm/s. 50 nm gold nanoparticles were dropcasted in the corners of the substrate for aligning the electron beam (Raith). Exposure of the sample was done with 50kV acceleration voltage and an e-beam dose of 2200 $\mu C/cm^2$. After exposure, the substrate was developed for 60 s in a solution of tetramethylammoniumhydroxide (TMAH) at 60°C and rinsed with H_2O for 15 s. Finally, the substrate was etched (Oxford Plasmalab 80+) using a mixture of 10 sccm sulfurhexafluoride (SF_6), 15 sscm trifluoromethane (CHF_3) and 3 sccm O_2. The final anisotropic meta-atoms in the metasurface have a length of 145 nm, a width of 105 nm and a height of 320 nm.

C Diffracted fields of an anisotropic metagrating

For didactic purposes, we first consider the scattering behaviour of a metagrating with identical meta-atoms and a duty cycle of $P/2$, where the long axis of the meta-atom is oriented along the principal axis of the grating. The fields scattered by such a grating upon excitation by some incident field $\mathbf{E}_{\text{in}}$ are described by a series of sources:

$$\begin{aligned}\mathbf{E}_{\text{out}}(\mathbf{r}) \quad &= \quad \left(\left(\left(\left(\sum_{m,n\in\mathbb{Z}} \delta\left(\mathbf{r}-\begin{pmatrix} m \\ n \end{pmatrix} a\right)\right)\right) \cdot \operatorname{rect}(\mathbf{x};-P/4,P/4)\right)\right. \\ &\qquad \left.\star \sum_{m\in\mathbb{Z}} \delta(\mathbf{x}-mP)\right)\begin{pmatrix} \alpha_L & 0 \\ 0 & \alpha_S \end{pmatrix} \mathbf{E}_{\text{in}}(\mathbf{r})\,. \qquad (2.7)\end{aligned}$$

where we ignore multiple scattering between individual meta-atoms and thereby assume metasurface operation in the 1st Born approximation. This metagrating will generate diffraction channels in Fourier space, which can be analyzed by Fourier transforming Eq. (2.7):

$$\mathbf{E}_{\text{out}}(\mathbf{k}_{||}) = \mathcal{F}[\text{geometry}]\left[\mathbf{M}(\mathbf{k}_{||})\begin{pmatrix} \alpha_L, 0 \\ 0, \alpha_S \end{pmatrix}\mathbf{E}_{\text{in}}\right]. \qquad (2.8)$$

This expression describes light scattering in Fourier space as the product of the Fourier-transform of the geometry $\mathcal{F}[\text{geometry}]$ with the radiation pattern of the isolated meta-atoms $\mathbf{M}(\mathbf{k}_{||})$. For simplicity, we will assume that the meta-atoms scatter light uniformly in all directions by equating $\mathbf{M}(\mathbf{k}_{||})$ to the identity matrix $\mathbf{I}$. The Fourier transform of the geometry can be evaluated by using the convolution theorem:

$$\begin{aligned}\mathcal{F}[\text{geometry}] = \left(\mathcal{F}\left[\sum_{m,n\in\mathbb{Z}} \delta\left(\mathbf{r}-\begin{pmatrix} m \\ n \end{pmatrix} a\right)\right] \star \mathcal{F}[\text{rect}(\mathbf{x};-P/4,P/4)]\right) \quad (2.9) \\ \cdot\mathcal{F}[\sum_{m\in\mathbb{Z}} \delta(\mathbf{x}-mP)].\end{aligned}$$

This expression consists of three main parts: the first part describes the Fourier transform of the dense sub-diffractive lattice, which will again result in a discrete lattice in Fourier space. The only k-vector component that is allowed to propagate, however, is the $k_{||}=0$ component, by virtue of the sub-diffractive spacing a. The second part is the Fourier transform of a rectangle function, which is a sinc function. These two expressions are finally multiplied by the Fourier transform of the supercell lattice, which will generate the relevant diffraction channels. Summarizing these operations, we obtain:

$$\mathbf{E}_{\text{out}}(\mathbf{k}_{||}) \propto \sum_{m\in\mathbb{Z}} \text{sinc}\left(\frac{k_{||}P}{4}\right)\delta\left(\mathbf{k}_{||} - m\frac{2\pi}{P}\right)\left[\begin{pmatrix}\alpha_L, 0\\ 0, \alpha_S\end{pmatrix}\mathbf{E}_{\text{in}}\right]. \tag{2.10}$$

The metagrating studied in the main text is the sum of two gratings with identical periodicity and duty cycle, but where in the second grating the scattering objects are differently oriented (90 degrees rotated) with respect to the objects in the first grating, which can be described by rotating the polarizability tensor to $\begin{pmatrix}\alpha_S, 0\\ 0, \alpha_L\end{pmatrix}$. Moreover, the second grating will experience a shift with respect to the first grating, where the shift is in general equal to $P/2+\Delta x$. Due to the Fourier shift theorem, the diffracted fields in Fourier space will experience an additional phase shift due to this displacement in real space, such that the total diffracted fields of the composite metagrating now read:

$$\begin{gathered}\mathbf{E}_{\text{out}}(\mathbf{k}_{||}) \propto \sum_{m\in\mathbb{Z}} \text{sinc}(k_{||}P/4)\delta(\mathbf{k}_{||} - m\frac{2\pi}{P}) \\ \left[\begin{pmatrix}\alpha_L, 0\\ 0, \alpha_S\end{pmatrix} + e^{ik_{||}(P/2+\Delta x)}\begin{pmatrix}\alpha_S, 0\\ 0, \alpha_L\end{pmatrix}\right]\mathbf{E}_{\text{in}}.\end{gathered} \tag{2.11}$$

Notice how in the scenario of $\Delta x = 0$, the extra phase shift in the diffracted fields of the second grating would be equal to -1, due to the diffraction condition $k_{||}P = 2\pi m$ in the $m'th$ diffraction channel. If the building blocks would be identical ($\alpha_L = \alpha_S$, then the diffraction channels would vanish, due to perfect destructive interference of the two interspersed gratings. This is logical, since in that case there only is a sub-diffractive lattice left.

To arrive at the expression from the main text, we substitute the grating condition into Eq. (2.11) to obtain:

$$\mathbf{E}_{\text{out}} \propto \left[\begin{pmatrix}\alpha_L, 0\\ 0, \alpha_S\end{pmatrix} + e^{im(\pi+\frac{2\pi\Delta x}{P})}\begin{pmatrix}\alpha_S, 0\\ 0, \alpha_L\end{pmatrix}\right]\mathbf{E}_{\text{in}}. \tag{2.12}$$

D Extension to 2D metasurfaces

Considering the two dimensional metagrating as discussed in Figure 2.6 from the main text, with 3 unrotated meta-atoms and 1 rotated meta-atom in the unitcell, the diffracted fields can be extended to two dimensions:

$$\mathbf{E}_{\text{out}}(\mathbf{k}_x, \mathbf{k}_y) \propto \sum_{m\in\mathbb{Z}} \sum_{n\in\mathbb{Z}} \delta\left(\mathbf{k}_x - m\frac{2\pi}{P}\right) \delta\left(\mathbf{k}_y - n\frac{2\pi}{P}\right) \quad (2.13)$$

$$\left[\left(1 + e^{i\frac{k_xP}{2}} + e^{\frac{ik_yP}{2}}\right) \begin{pmatrix} \alpha_L, 0 \\ 0, \alpha_S \end{pmatrix} + e^{ik_x\left(\frac{P}{2}+\Delta x\right)} e^{ik_y\left(\frac{P}{2}+\Delta y\right)} \begin{pmatrix} \alpha_S, 0 \\ 0, \alpha_L \end{pmatrix}\right] \mathbf{E}_{\text{in}}.$$

E Phase lags in the polarizability tensor

In this section, we show how deviations from the ideal half wave plate condition can lead to non-symmetrical polarization splitting effects on the Poincaré sphere and intensity offsets in metrological experiments such as we report in Figures 2.4 and 2.6 in the main manuscript. For this, we introduce extra phase lags between the complex polarizabilities α_L and α_S and calculate the polarization states of the diffraction orders and corresponding sensitivity curves using our analytical model. In this particular example, we set α_S to 1 and α_L to $2.25e^{1.25\pi i}$. Figure 2.7a shows the corresponding polarization state of the diffraction channels on the Poincaré sphere, and Figure 2.7b shows the corresponding 2D projection onto the lower hemisphere, showing marked deviations from the symmetric splitting in S_2 such as we measured in experiments. For the same polarizability settings, we furthermore plot the analytical sensitivity curves using the same procedure as was done in Figures 2.4 and 2.6 for an unperturbed ($\frac{\Delta x}{P} = 0$) and perturbed ($\frac{\Delta x}{P} = 0.25$) metasurface. Here we note an intensity offset in the shifted $\sin^2$ functions, such as we have also observed in Figure 2.6f and 2.4d in the main text.

F Fisher information of a single pixel measurement

To derive the information content in one diffraction channel of the anisotropic metasurface, we derive the Fisher information of a single pixel measurement. The Fisher information is defined according to [11]:

$$F = E\left[\left(\frac{\partial \ln p(X;\hat{\Theta})}{\partial\hat{\Theta}}\right)^2\right], \quad (2.14)$$

where $E[]$ is the expectation operator, $p(X;\hat{\Theta})$ is a probability density function, describing the probability of measuring a dataset X parametrized by an in principle un-known parameter $\hat{\Theta}$. In our work, this parameter $\hat{\Theta}$ corresponds to potential displacements Δx in the plane of the metasurface, which we would like to estimate based on our polarimetric measurement. The Fisher information then quantifies a lower bound on the variance with which this unknown parameter can be estimated, according to the Cramér-Rao lower bound:

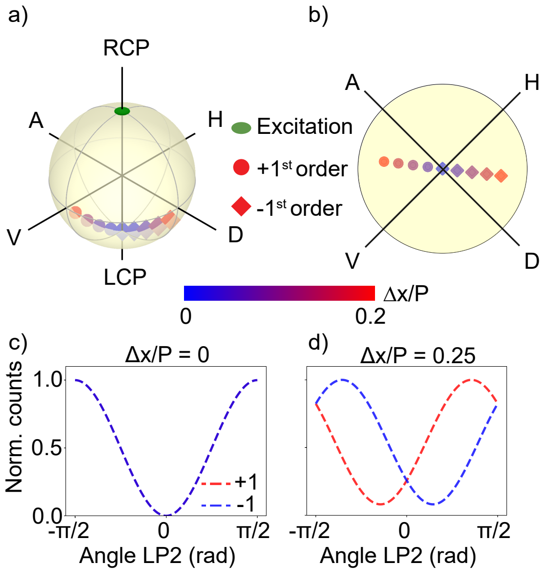

Figure 2.7: Influence of phase lags in the complex polarizability tensor. Panel (a): Polarization state of the diffraction orders on the Poincare sphere for α_S = 1 and α_L = $2.25e^{1.25\pi i}$. Panel (b): 2D projection of the data in panel (a) onto the lower hemisphere of the Poincare sphere. Panels (c) and (d) show corresponding sensitivity curves for $\frac{\Delta x}{P} = 0$ and $\frac{\Delta x}{P} = 0.25$ respectively.

$$V(\hat{\Theta}) \geq \frac{1}{F}. \tag{2.15}$$

We assume that shot-noise is the limiting noise contribution in our measurements. In that case, $p(X; \hat{\Theta})$ follows Poisson statistics:

$$p(X = k; \hat{\Theta}) = \frac{I^k e^{-I}}{k!}, \tag{2.16}$$

which describes the probability of measuring k photons onto a single pixel detector and $I(\hat{\Theta})$ the mean number of photons. Substituting this expression for the proability density into Eq. (2.14) and working out the terms results in:

$$F = \left(\frac{\partial I}{\partial \hat{\Theta}}\right)^2 \left(\frac{1}{I^2} E\left[k^2\right] - \frac{2}{I} E\left[k\right] + E\left[1\right]\right). \tag{2.17}$$

Here, we recognize the moments of the expectation operator:

$$\begin{aligned} E\left[k^2\right] &= I^2 + I \\ E\left[k\right] &= I \\ E\left[1\right] &= 1 \end{aligned} \tag{2.18}$$

and obtain the expression for the Fisher information content from a shot-noise limited single pixel bucket measurement:

$$F = \frac{1}{I}\left(\frac{\partial I}{\partial \hat{\Theta}}\right)^2 . \tag{2.19}$$

In order to apply this expression to our Fourier space polarimetric readout scheme, we notice that our parameter estimation problem relies on measuring the intensities of 2 discrete diffraction orders, which can, in principle, be acquired by two single pixel bucket detectors. Because the Fisher information is an additive quantity, the information content in our polarimetric measurement can finally be written as:

$$F = \frac{1}{I_+}\left(\frac{\partial I_+}{\partial x}\right)^2 + \frac{1}{I_-}\left(\frac{\partial I_-}{\partial x}\right)^2 , \tag{2.20}$$

where $I_\pm$ and $\frac{\partial I_\pm}{\partial x}$ are the diffracted intensity and intensity differentials respectively in the $\pm 1^{st}$ diffraction orders

Chapter 3

Information Advantage in Sensing Revealed by Fano-Resonant Fourier Scatterometry

Fano resonances in nanophotonic structures are attractive for sensing due to their ultanarrow resonant linewidths and high local fields. Conventional read out schemes rely on measuring a frequency shift in Fano scattering spectra as function of perturbation. We experimentally demonstrate that angle-resolved analysis of the scattering of a Fano resonant structure is quantitatively more informative than measuring spectral shifts. We theoretically discuss how a perturbation affects fundamental nanophotonic properties of a Fano resonant metasystem, and how these are transduced to an observable far field response. We perform a rigorous experimental study in which we characterize deeply subwavelength perturbations in a Fano resonant dielectric metasurface using a conventional spectral approach, and a Fourier scatterometry based approach, and show that perturbations can lead to marked directional scattering in Fourier space. We finally quantitatively compare these two sensing methods in terms of their inherent Fisher information content, and show that an information advantage is obtained when the signal is resolved in Fourier space.

3.1 Introduction

Resonance based sensors are at the heart of many modern day scientific and commercial instruments to accurately detect minute forces [112] or mass changes [113], characterize material properties [114] and acquire high quality medical images [115]. In these technologies, the strong responsivity of the system at resonance is exploited to retrieve precise estimations of the relevant physical property to be detected. In the field of nano-optics, resonance based sensors are routinely exploited to detect perturbations in the form of biomolecules [116, 117], gasses [118, 119], displacements [120] and accelerations [121], where the resonant response originates from localized surface plasmon modes in noble metal nanoparticles [116, 117] or an interplay between optical and mechanical vibrations [120, 121], to name a few. In all these nanophotonic sensing protocols, a resonant spectral feature is usually identified in experimental observables like absorption [116], scattering and extinction cross sections [117, 118] in single nanoparticles, or reflection and transmission spectra in extended thin films or arrays of nanoparticles [117]. Refractive index changes and geometry changes form a perturbation that imprints a detectable shift onto the resonance frequency. To achieve optimal sensing performance, which is usually captured in the sensing figure of merit (FOM), the shift of the resonance frequency per unit perturbation needs to be large compared to the linewidth of the resonance, and systems which exhibit ultrahigh quality factor (Q-factor) resonant features are therefore highly sought after in the sensing community. The Fano resonance [26, 122], which is a distinct asymmetric spectral line shape arising from interference effects between a broad superradiant and sharp subradiant state, has shown great potential in sensing applications due to their inherent high Q-factors [123]. The recent advent of dielectric metasurfaces, which are two-dimensional (2D) sheets decorated by designer low-loss dielectric particles, has provided a powerful toolbox for engineering these Fano resonances through the physics of bound states in the continuum (BIC) [30, 31]. A BIC is a phenomenon in which a state remains perfectly localized and therefore does not radiate, despite existing within the continuous energy spectrum of radiating states. True BICs therefore have a vanishing resonance linewidth and infinite quality factor, and can only exist within infinite and ideal lossless systems. In practical scenarios a BIC mode can be translated into a so-called quasi-BIC with finite and tunable quality factor by introducing a small asymmetry in the structural parameters of the metasystem. Sensors exploiting the excitation of these symmetry protected quasi-BIC modes have shown record high sensing FOM's [32, 33].

In parallel to these resonance based efforts, nanophotonic platforms have been designed that efficiently transduce information about a given perturbation into the far-field by monitoring the rich contents of angle resolved scattering patterns. Indeed, deeply subwavelength or "superresolution" estimation precision of a perturbation has been achieved by analyzing the Fourier space scattering of complex nanophotonic objects [93, 124], and even single nanoparticles [75, 125, 126]. These studies differ in experimental observable from the resonance based works in the sense that in the former, the far-field signal is resolved into its angular components (Fourier space), whereas in the latter the signal is usually acquired in an angle integrated modality on either a spectrometer or a single pixel bucket detector, thereby losing potentially useful information about the perturbation in Fourier space. In fact, Fano resonances have been shown to exhibit directionality properties [127, 128], which could provide an information gain in a sensing based experiment. However, to the best of our knowledge, there are no reported sensing experiments in which the signal of a Fano resonant scattering sensor is analyzed in Fourier space, and in which the information advantage is quantified which such an angle resolved measurement modality may have relative to conventional spectroscopy.

In this chapter, we study how perturbations affect the far field scattering properties of a Fano resonant metasystem, and show that an information gain can be achieved when the resonant scattering is analyzed in Fourier space, as conceptually sketched in figure 3.1. We start with a theoretical discussion of all relevant nanophotonic response function changes a perturbation can induce onto a Fano resonant system, and how these are transduced into the far-field. We then perform a rigorous experimental study, in which we characterize the influence of a perturbation in dielectric Fano resonant metasystems in both an angle integrated spectral modality and a Fourier space measurement, and show that deeply subwavelength information about the perturbation is resonantly transduced into marked directional scattering in Fourier space. We finally compare both measurement modalities in terms of the Fisher information they contain about the perturbation, and show quantitatively that a Fourier space measurement has a higher Fisher information content than an angle integrated measurement.

3.2 Theoretical motives

To study how a Fano resonant metasystem transduces information into far-field Fourier components, our first objective is to identify a Fano resonant metasurface that allows light scattering into higher order diffractive channels. This is not a trivial prerequisite, since the majority of Fano resonant metasurfaces studied in the literature are constructed by semi-infinite periodic lattices with subwavelength periodicity, thus only allowing coupling to the zero order transmission and reflection channels. Possible disturbances from the perfect sub-wavelength periodicity, that are necessary to generate diffraction channels, such as edge effects [129] [130] and fabrication imperfections [131] generically lead to a reduction of the resonance quality factor. Besides semi-infinite non-diffractive lattices, other well known types of metasystems

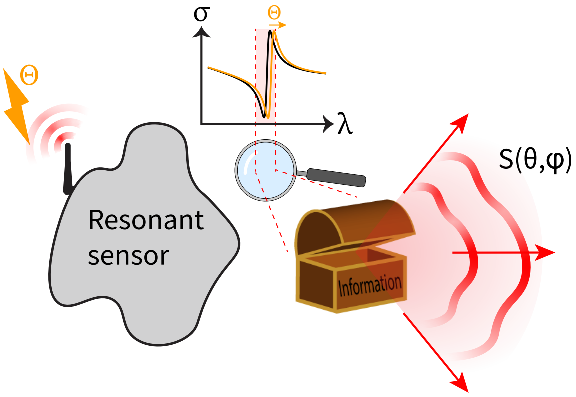

Figure 3.1: A Fano resonant scattering sensor detects a perturbation Θ, causing the resonance wavelength to be shifted. When the signal is analyzed in Fourier space, however, additional information about the perturbation can be gained.

supporting Fano resonances are for instance plasmonic [132, 133] and dielectric [134] oligomers of nanoparticles, and even single dielectric nanoparticles supporting so-called supercavity modes [134–136]. In contrast to the subdiffractive infinitely extended metalattices, these finite sized systems are allowed to scatter light into a continuous angular spectrum, fully determined by the structure factor of the relevant mode profile at play. Drawbacks of many finite-sized Fano resonant structures are that often the quality factor is not easily tunable, or that complex structured illumination conditions are required to selectively excite the resonances. We identify symmetry protected quasi-BIC Fano resonances in finite sized annular metarings as particularly promising for our study. Such metarings were demonstrated in a recent study by Kühner et al. [137] and have tuneable resonances that are accessible by simple plane wave illumination. While the interparticle spacing of the high refractive index meta-atoms in such rings is still subdiffractive to ensure strong collective mode coupling, the shape in which the meta-atoms are patterned allows light scattering into higher order Fourier channels. In the language of X-ray scattering or treatments of antenna directivity, the radiation pattern can be understood as the product of a ‘structure factor’, or ‘array factor’, that derives from the placement of units on a circle, and a ‘form factor’ or ‘element factor’ that accounts for the dipolar radiation pattern of each individual meta-atom [138]. The structure factor of a circle, chosen as a few wavelengths across, provides concentric rings of scattered intensity in Fourier space. The flexible toolkit of symmetry protected quasi-BIC resonances allows relatively straightforward tuning of the Fano resonance by controlling structural symmetry parameters.

In the following we will focus on sensing perturbations in the form of deeply subwavelength structural displacements between the individual building blocks in metarings as described above. These type of perturbations are highly relevant in modern day semiconductor device manufacturing for so-called interlaced metrology [10]. Figures 3.2a and 3.2b illustrate the scenario at hand on basis of electron microscopy images of resonant silicon metarings that we interrogate in the experimental part of this paper (see Appendix B for nanofabrication details). Figure 3.2a displays an unperturbed metaring: radially oriented silicon blocks are equidistantly placed on a ring, and blocks alternate in length. The asymmetry in the length of neighboring meta-atoms ΔL tunes the Fano resonance by a symmetry protected quasi-BIC mechanism [30, 137]. In figure 3.2b, the perturbed structure is shown. The perturbation corresponds to a collective upward shift Δy of the entire subring of short meta-atoms.

To explore the influence of perturbations in a Fano resonant sensing scenario, we tackle the problem from an eigenmode perspective. While one could derive quasinormal modes from a numerical eigensolver, we semi-analytically model the annular metasystem using coupled dipole theory [139, 140], in which the individual meta-atoms are approximated as polarizable point dipoles, while all electrodynamic multiple scattering interactions are taken into account. Using the specific modeling parameters as discussed in the methods section, we construct the dipole-dipole interaction matrix of the system, from which we extract all relevant modes of the metarings by performing an eigenvalue decomposition. We obtain (essentially frequency-independent) eigenvectors $\mathbf{p}_{\mathrm{m}}$, which correspond to the natural coupled dipole oscillations in the metaring, along with corresponding eigenvalues $\lambda_{\mathrm{m}}(\omega)$, describing the eigenpolarizabilities of the respective modes. The response of the metaring to incident light can be decomposed in the eigenmodes, and depends both on the magnitude of the eigenpolarizabilities and the overlap of the incident field with the eigenvector. We assume an externally applied electric field $\mathbf{E}_{\mathrm{exc}}$ that correspond to a y-polarized plane wave normally incident onto the ring. This will lead to a driven dipole configuration $\mathbf{p}_{\mathrm{driven}}$

$$\mathbf{p}_{\mathrm{driven}} = \sum_{\mathrm{m}} \alpha_{\mathrm{m}}(\omega)\mathbf{p}_{\mathrm{m}}, \tag{3.1}$$

where $\alpha_{\mathrm{m}}(\omega)$ corresponds to the expansion coefficients of mode $\mathbf{p}_{\mathrm{m}}$. These coefficients depend on the overlap of the eigenmode with the external excitation field $\langle \mathbf{p}_{\mathrm{m}} | \mathbf{E}_{\mathrm{exc}} \rangle$ and the eigenvalue $\lambda_{\mathrm{m}}(\omega)$ as

$$\alpha_{\mathrm{m}}(\omega) = \lambda_{\mathrm{m}}(\omega) \langle \mathbf{p}_{\mathrm{m}} | \mathbf{E}_{\mathrm{exc}} \rangle \,. \tag{3.2}$$

The two most dominant eigenvector profiles in the expansion are depicted in figures 3.2c and 3.2d. From the plot in figure 3.2c, we see a collective dipolar eigenmode $\mathbf{p}_{\mathrm{bright}}$ which is superradiant, whereas in the profile shown in figure 3.2d a subradiant eigenmode $\mathbf{p}_{\mathrm{dark}}$ can be identified. These are exactly the bright and dark modes that are responsible for the Fano interference in our metasystem, and lay the foundation for the relevant physics in the sensing experiment.

We are now in a position to discuss the possible consequences of a perturbation to the modes of a Fano system. First of all, the eigenmode profiles themselves will be perturbed. This is highlighted for both the bright and dark modes in figures 3.2c and 3.2d, where the black and red arrows correspond to the unperturbed and perturbed eigenmodes respectively. We note that particularly the dark mode profile shows considerable sensitivity to perturbations. The perturbed eigenmode profiles will in turn lead to an altered overlap of the modes with the external driving field, along with perturbed eigenvalues. These two effects combined consequently lead to perturbed excitation coefficients $\alpha_{\mathrm{m}}(\omega)$, as shown in figures 3.2e and 3.2f for both the bright and dark mode respectively. Here, the absolute value of the complex excitation coefficients is plotted as function of wavelength. Note here that $\alpha_{\mathrm{bright}}(\omega)$ has a relatively weak wavelength dependence, which is expected due to the broadband nature of a mode with large scattering losses. On the other hand $\alpha_{\mathrm{dark}}(\omega)$ shows a strong dispersion and a sharp peak around 780 nm where the Fano interference takes place, and again the largest sensitivity to perturbations. Note that the eigenmode perturbation and corresponding change in overlap with an external driving field is exactly the underlying mechanism that also allows coupling to a symmetry protected quasi BIC resonance, with the perturbation being a structural symmetry breaker (ΔL here). The prediction of Fig. 3.2(b-f) is that this same mechanism brings sensitivity to Δy.

We have so far discussed the influence of perturbations on eigenmodes only, but not yet on experimental observables with which an experimentalist would actually probe the perturbations. The conventional strategy in sensing is to analyze the spectral response of the Fano system, which would be a single scattering channel reflection or transmission spectrum in the case of nondiffractive metasurfaces, or an angle integrated scattering spectrum in finite sized diffractive structures. In figure 3.2g we show the angle integrated scattering cross section of the unperturbed and perturbed driven dipole configuration $\mathbf{p}_{\mathrm{driven}}$ for a y-polarized plane wave driving field. A Fano lineshape is evident, resulting from the modal interference of the eigenmodes $\mathbf{p}_{\mathrm{bright}}$ and $\mathbf{p}_{\mathrm{dark}}$. A small shift and decrease in scattering amplitude is also visible for the perturbed cross section, which results from the perturbed excitation coefficient in figure 3.2f. This altered spectral lineshape can be used to for instance translate structural perturbations into measurable intensity differentials when the system is illuminated at resonance, thus providing information about the perturbation at hand. However, as the entire angular spectrum of the scattered signal is integrated, potentially rich angular dependent information is lost in the angle integration.

We now investigate how the perturbation influences directional scattering in Fourier space by resolving the scattered signal over all viewing angles $\hat{\mathbf{k}}$.

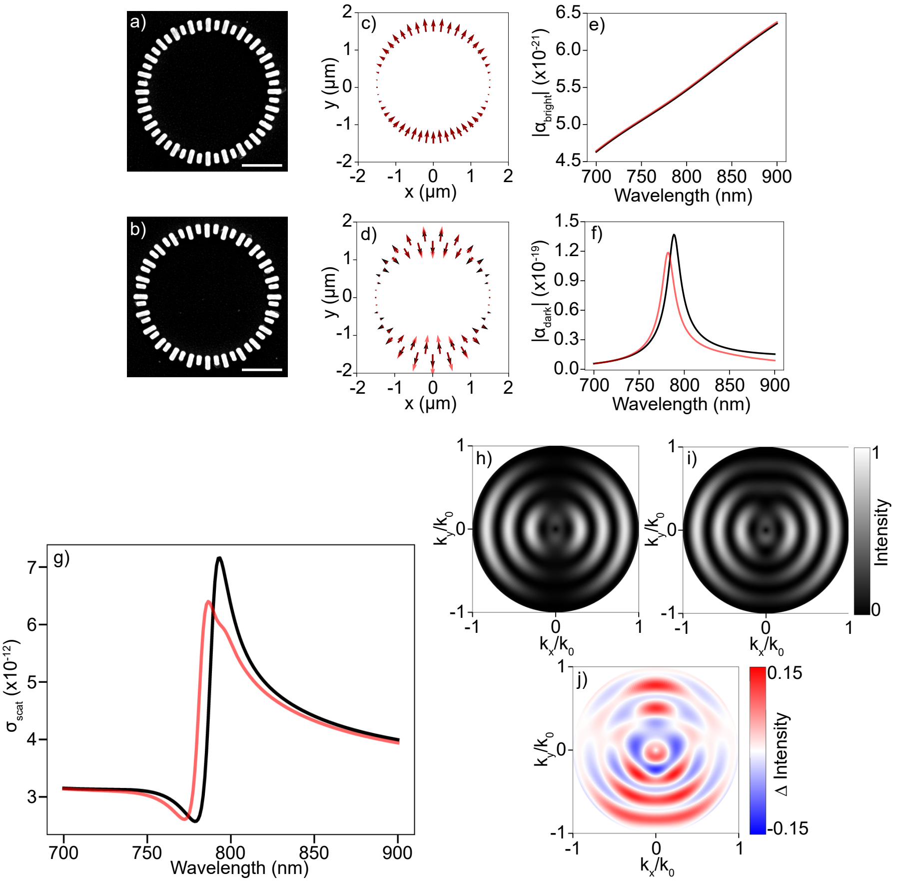

Figure 3.2: Theoretical considerations in Fano resonance based sensing schemes. Panels (A) and (B): SEM images of the unperturbed and perturbed versions of the studied Fano resonant metasystem respectively, where the perturbation corresponds to an upward shift of every other meta-atom by 50 nm. Scalebar corresponds to 1 μm. Panels (C) and (D): Respectively super and subradiant eigenmode profiles of the dipole orientations in the metaring. The black and red arrows showcase unperturbed and perturbed versions of the eigenmodes respectively. Panels (E) and (F): Absolute value of the modal excitation coefficient for the super and subradiant eigenmodes respectively. Panel (G): Scattering cross section of the (un)perturbed dipolar metasystem. Panels (H) and (I): Fourier space radiation patterns for the unperturbed and perturbed metaring respectively, driven by an excitation wavelength of 775 nm. Panel (J): Differential radiation pattern resulting from the subtraction of radiation patterns in panels (H) and (I).

The acquired Fourier space radiation diagrams $S_{\mathrm{tot}}(\hat{\mathbf{k}}, \omega)$ can again be decomposed into modal contributions as

$$S_{\mathrm{tot}}(\hat{\mathbf{k}}, \omega) = \alpha_{\mathrm{bright}}(\omega) S_{\mathrm{bright}}(\hat{\mathbf{k}}) + \alpha_{\mathrm{dark}}(\omega) S_{\mathrm{dark}}(\hat{\mathbf{k}}), \tag{3.3}$$

where $S_{\mathrm{bright}}(\hat{\mathbf{k}})$ and $S_{\mathrm{dark}}(\hat{\mathbf{k}})$ are the modal radiation patterns emitted by $\mathbf{p}_{\mathrm{dark}}$ and $\mathbf{p}_{\mathrm{bright}}$ respectively. Intensity only measurements on a detector can be accounted for by taking the modulus squared of the complex radiation patterns, resulting in

$$|S_{\mathrm{tot}}(\hat{\mathbf{k}}, \omega)|^2 = |\alpha_{\mathrm{bright}}(\omega) S_{\mathrm{bright}}(\hat{\mathbf{k}}) + \alpha_{\mathrm{dark}}(\omega) S_{\mathrm{dark}}(\hat{\mathbf{k}})|^2$$

$$= |\alpha_{\mathrm{bright}}|^2 |S_{\mathrm{bright}}|^2 + |\alpha_{\mathrm{dark}}|^2 |S_{\mathrm{dark}}|^2 + 2\,\mathrm{Re}(\alpha_{\mathrm{bright}} \alpha^*_{\mathrm{dark}} S_{\mathrm{bright}} S^*_{\mathrm{dark}}). \tag{3.4}$$

From this expression it is evident that the total acquired radiation pattern is composed of individual contributions from the bright and dark modes, along with a modal interferometric term. Supposing there is complete transparency in scattering, which is realistic in Fano resonant systems, that would mean that the interferometric term in Eq. (3.4) fully cancels the first two terms for every viewing angle, from which it can be concluded that the modal radiation patterns S_{bright} and S_{dark} should be very similar to each other. Perturbations imprinted on the eigenmodes would in turn lead to additional changes in the modal radiation patterns and thus on the total radiation pattern $|S_{\mathrm{tot}}|^2$ as well. In figures 3.2h and 3.2i we show Fourier space radiation patterns of the unperturbed and perturbed dipole configurations, while driving the system at resonance at a wavelength of 775 nm. In these figures, we observe concentric rings of bright intensity regions, which correspond to the spatial frequencies or structure factor of the the annulus. These rings in k-space are further supplemented by dark intensity regions in the k_y/k_0 viewing direction, which are a result of a polarization selective form factor of the collective dipole along the y-direction. The perturbed radiation patterns shows broadly similar features, but marked differences can be spotted with respect to the unperturbed pattern upon closer inspection. To highlight the angular dependent differential signal in Fourier space, we subtract the unperturbed and perturbed Fourier images to arrive at a differential radiation pattern in figure 3.2j. A key advantage of the Fourier space diagram with respect to the angle integrated scattering spectrum in figure 3.2g is that in the former regions with both positive and negative intensity differentials may be resolved, which would otherwise cancel out when the signal would be integrated over all angles. This observation hints towards a potential gain in information about the perturbation when the scattered signal of a Fano resonant structure is dispersed in Fourier space, which we will set out to quantify experimentally in the next sections.

3.3 Resonance characterization

To spectrally characterize the resonant properties of individual dielectric metarings experimentally, we perform dark-field scattering spectroscopy, with a schematic of the setup depicted in the supplementary information. In brief, a single metaring (Si meta-atoms on a glass substrate, dimensions and fabrication methods listed in Appendix B) is illuminated by a broadband supercontinuum laser with a low effective NA (NA = 0.18), after which the scattered signal is captured in reflection through the same high NA objective (NA = 0.95). Dark-field acquisition is ensured by filtering the low NA back reflection of the illumination out of the total signal by placing a beam stop in the conjugate Fourier plane of the imaging system. Examples of raw spectra are shown in figure 3.3a, where we show a series of darkfield scattering spectra of individual rings with asymmetry parameters of $\Delta L = 0$ nm in red and $\Delta L = 100$ nm in blue, along with their respective averaged spectra in black. Different spectra with the same color indicate spectra scattered by different realizations of metarings with nominally identical fabrication parameters. A good overlap between these individual spectra is seen, indicating that metarings with nominally identical fabrication parameters have reproducible scattering properties. Spectra of the rings with $\Delta L = 100$ nm contain a clear asymmetric feature around 720 nm with respect to the rings with $\Delta L = 0$ nm, hinting towards a Fano lineshape in the scattered signal. To isolate the Fano resonant features within the scattering spectra, we normalize all raw spectra by the average spectrum of the metarings with asymmetry parameter $\Delta L = 0$ nm, as these metarings are not expected to exhibit Fano resonant features due to symmetry protection of the dark mode. In figure 3.3b we show an exemplary normalized spectra of an individual metaring with asymmetry $\Delta L = 100$ nm. Indeed, an asymmetric Fano like lineshape is seen in the normalized scattering spectrum, and fitting the data in close vicinity around the resonance with a Fano function results in an excellent match. To validate that the Fano feature results from the quasi-BIC in our system, we analyze the normalized scattering spectra of the metarings as a function of the asymmetry parameter ΔL in figure 3.3c. We clearly observe a broadening of the resonance linewidth for increasing ΔL, along with a blueshift of the resonance wavelength, both characteristic of a quasi BIC due to symmetry breaking. These observations are substantiated by fit results in figure 3.3e, where we show resonance wavelengths and linewidths extracted by fitting Fano lineshapes to normalized scattering spectra of individual metarings. The datapoints and errorbars in this panel correspond to respectively the mean and standard deviation of the fitparameters retrieved from the spectra of multiple realizations of individual metarings We next analyze the influence of the perturbation on the scattering behaviour, and show the normalized scattering spectra of the metarings with fixed asymmetry $\Delta L = 100$ nm for increasing perturbation strength Δy in

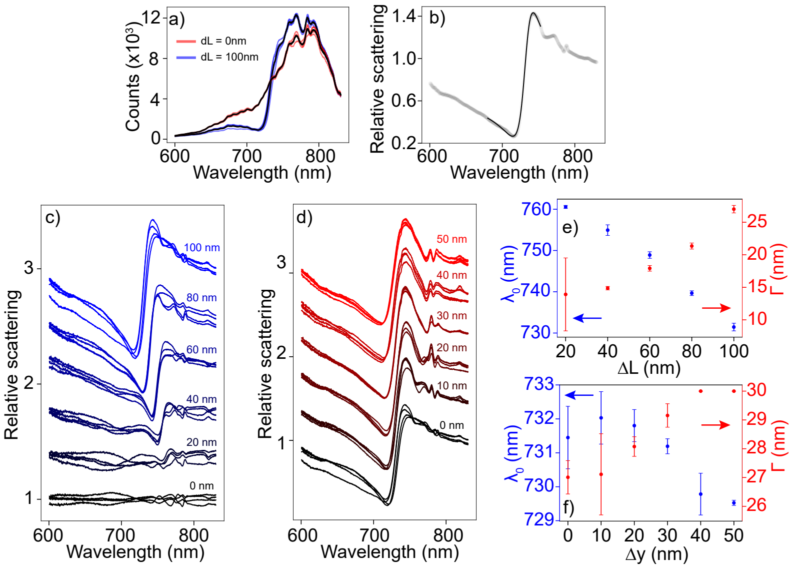

Figure 3.3: Dark-field spectroscopy on single resonant metarings. Panel (A): Raw dark-field spectra of individual unperturbed metarings with $\Delta L = 0$ nm (red) and $\Delta L = 100$ nm (blue). The black lines indicate the average spectra. Panel (B): Example spectrum of a single unperturbed metaring with $\Delta L = 100$ nm normalized by the average spectrum of the $\Delta L = 0$ nm metarings. Shaded datapoints indicate experimental data, the black solid line indicates a fit by a Fano lineshape. Panel (C): Normalized scattering spectra of unperturbed metarings for increasing asymmetry ΔL. Spectra are offset by 0.4 relative scattering units for clarity. Panel (D): Normalized scattering spectra of metarings with fixed asymmetry $\Delta L = 100$ nm for increasing perturbation strength Δy. Spectra are offset by 0.4 relative scattering units for clarity. Panel (E): Resonance wavelength and linewidth of the unperturbed metarings versus asymmetry ΔL. Panel (F): Resonance wavelength and linewidth of metarings with fixed asymmetry $\Delta L = 100$ nm versus perturbation strength Δy. Errorbars denote standard deviations of the fitparamaters retrieved from the spectra of multiple individual metarings.

figure 3.3d. Performing the same fitting analysis on this set of normalized spectra results in extracted resonance wavelengths and linewidths versus Δy in figure 3.3f. These results show a broadening of the resonance for increasing Δy, which can be explained by the fact that the perturbation disturbs the otherwise perfect annular periodicity of the metaring, thereby degrading the resonance quality. This trend is in line with the results of studies on fabrication tolerances on resonant metasurfaces [131]. Apart from the spectral broadening, a minor shift in resonance wavelength is seen as a function of Δy. These results show that the scattering spectra show deeply subwavelength sensitivity to structural perturbation within the metasurface, albeit that the spectral changes are small.

3.4 Displacement induced directionality

In this section, we investigate the sensitivity to perturbations of the scattered signal in Fourier space. For this, we utilize Fourier microscopy, (see Appendix C for a sketch of the setup), where we disperse the scattered signal into angular contributions by imaging the back-focal-plane of a microscope objective onto a C-MOS camera. As we did for the spectroscopic measurements described in the previous section, we illuminate individual metarings with a low effective NA (NA = 0.18) and polarization parallel to the y-direction (parallel to the displacement), but now we bandpass filter the excitation wavelength with a bandwidth of 10 nm. We vary the center wavelengths of these filters to spectrally overlap with the Fano resonances as measured in figure 3.2, and capture the corresponding Fourier images scattered by the individual metarings. As such, we acquire directional scattering patterns of individual rings both on and off-resonance, and investigate the sensitivity to perturbations in both spectral regimes.

In figure 3.4a and 3.4b, we show exemplary raw Fourier images of perturbed ($\Delta y = 50$ nm) and unperturbed ($\Delta y = 0$ nm) metarings respectively, with fixed asymmetry parameter ($\Delta L = 80$ nm), acquired at an on-resonance excitation wavelength of 730 nm. In all acquired images, we clip out in software a circle in the center of Fourier space, as it contains the direct reflection of the illumination by the substrate. The concentric rings originating from the structure factor of the annulus are evident, multiplied by the form factor of the collective dipole emission as we also saw in the calculations of figure 3.2h. We furthermore observe a clear asymmetry in scattered signal in the k_y/k_0 viewing direction for the perturbed ring as compared to the scattered signal of the unperturbed ring, indicating that structural perturbations are transduced into observable Fourier space asymmetries. Note that the symmetry axis in both the real and Fourier space is preserved, since displacements in the y-direction in real space lead to specific asymmetries along the k_y/k_0 viewing direction in Fourier space.

To better visualize this asymmetry in Fourier space, we subtract the angle resolved scattering patterns of an individual unperturbed ring from a perturbed ring to arrive at a differential Fourier space scattering image. To study the influence of the perturbation strength and the excitation wavelength on the asymmetry in Fourier space, we acquire such differential Fourier images for multiple perturbation strengths and for both on and off-resonance excitation. The results are shown in figures 3.4c-3.4n. From left to right, the perturbation strength is gradually increased from $\Delta y = 0$ nm to $\Delta y = 50$ nm in steps of 10 nm, while in the top and bottom rows the excitation wavelength is set to respectively on (730 nm) and off-resonance (780 nm) excitation. We note that the differential images shown for the two wavelength are scattered by exactly the same pair of rings.

Differential images of unperturbed rings with nominally identical fabri-

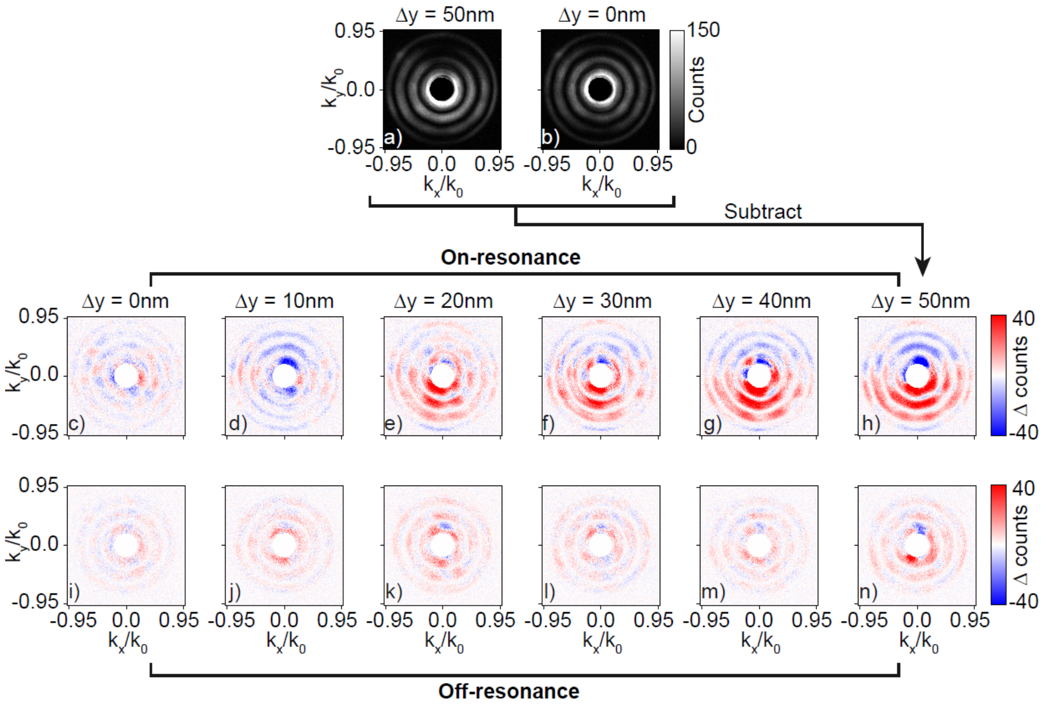

Figure 3.4: Fourier space scatterometry reveals perturbation induced directional scattering. Raw images of angle resolved scattering images for a metaring with perturbation strengths of panel (A): $\Delta y = 50$ nm and panel (B): $\Delta y = 0$ nm acquired at a wavelength of 730 nm. Angle resolved differential scattering images acquired at a wavelength of 730 nm when the signal of an unperturbed metaring is subtracted from a metaring with perturbation strength of Panel (C): $\Delta y = 0$ nm, Panel (D): $\Delta y = 10$ nm, Panel (E): $\Delta y = 20$ nm, Panel (F): $\Delta y = 30$ nm, Panel (G): $\Delta y = 40$ nm and Panel (H): $\Delta y = 50$ nm. Panels (I-N): Same as panels (C-H), but for a wavelength of 780 nm. The results are shown for metarings with asymmetry of $\Delta L = 80$ nm.

cation parameters scatter a relatively low differential contrast-to-noise ratio in Fourier space as can be seen in figures 3.4c and 3.4i. This observation underscores the highly reproducible scattering characteristics of metarings with nominally identical fabrication parameters, as was also evident from the scattering spectra from figure 3.2c. When the perturbation strength is gradually increased from $\Delta y = 0$ nm to $\Delta y = 50$ nm, the differential contrast in Fourier space at resonance in figures 3.4c-3.4h scales accordingly, while the differential contrast off-resonance in figures 3.4i- 3.4n remains relatively unaltered. From these measurements, we conclude that deeply subwavelength structural misalignments are resonantly transduced by the Fano resonance into directional scattering asymmetries in Fourier space.

3.5 Information advantage

In the previous two sections, we have presented two different experimental strategies for the detection of a perturbation in a Fano resonant metasystem, namely dark-field spectroscopy and Fourier scatterometry. The intriguing question which of these two measurements most efficiently detects the perturbation then naturally arises. In this section, we will quantitatively answer this question by determining the information content that each measurement contains about the relevant perturbation. For this, we will use the concept Fisher information [11], which defines a fundamental bound to the precision with which perturbations Θ can be estimated from measured data X, which are unavoidably corrupted by noise. Assuming that one has access to a theoretical description of the noise in terms of a probability density function $p(X;\Theta)$, which describes the probability of measuring a dataset X given a certain perturbation strength Θ, which in our specific sensing experiment corresponds to structural misalignments Δy, the Fisher information is defined as [11]

$$F = E\left[\left(\frac{\partial \ln p(X;\hat{\Theta})}{\partial \hat{\Theta}}\right)^2\right], \tag{3.5}$$

where $E[.]$ denotes the expectation operator. Assuming further that one can construct a so-called unbiased estimator, which is an operation that translates a dataset X into an estimation of the perturbation $\hat{\Theta}$ that on the average should equate the true perturbation Θ, the fundamental precision bound of the estimation is defined by the Cramer-Rao bound

$$\sigma_{\hat{\Theta}}^2 \geq \frac{1}{F}. \tag{3.6}$$

Here, $\sigma_{\hat{\Theta}}$ is the standard deviation of the estimated parameter $\hat{\Theta}$. From this expression, we see that the higher the Fisher information content, the lower the minimum standard deviation and thus the higher the precision with which the perturbation can be estimated from measured data. Maximization of the Fisher information has already been shown to positively impact the measurement precision in experimental contexts such as 3D localization and imaging [73], sensing perturbations in disordered environments [74, 141, 142] and tracking single molecules [143].

To arrive at a closed form expression for the Fisher information in the context of our sensing experiment, we will now discuss the several noise factors that can corrupt our measured data and thus reduce the available Fisher information. The first noise source originates from the unavoidable fabrication errors that invoke additional shape perturbations besides the controlled perturbation that we want to detect. Although our structures show decent reproducibility in scattering properties, two individual metasystems with nominally identical fabrication parameters will never scatter in a perfectly identical way due to fabrication imperfections, as could already be observed from figures 3.4c and 3.4i, where small residues in scattering contrasts exist above the inherent noise floor of the measurement. The measurement noise floor in turn consists of photon shot noise and detector read noise, which we describe in the supplementary information. For simplicity, we have assumed that the only noise sources originate from photon shot noise and detector related noise sources in the derivation of the Fisher information, and describe how we correct for the fabrication noise later on in this section. For analytical tractability, we describe the noise in a single pixel on the detector as Gaussian

$$p(X;\hat{\Theta}) = \frac{1}{\sqrt{2\pi\sigma_{\mathrm{tot}}^2(\hat{\Theta})}} e^{-\frac{(X-I_0(\hat{\Theta}))^2}{2\sigma_{\mathrm{tot}}^2(\hat{\Theta})}}, \tag{3.7}$$

which represents the probability of measuring X photons given a mean number of measured photons $I_0(\hat{\Theta})$ and a standard deviation given by the sum of shot-noise and detector readout noise σ_{read} contributions

$$\sigma_{\mathrm{tot}}^2(\hat{\Theta}) = I_0(\hat{\Theta}) + \sigma_{\mathrm{read}}^2. \tag{3.8}$$

The choice of a Gaussian distribution instead of Poissonian is a convenient way to account for the mixed contributions from shot noise and detector readout noise, and for the count rates at hand the Gaussian distribution approaches the Poissonian one. Substituting Eqs. (3.8) and (3.7) into Eq. (3.5) results in the following closed form expression for the Fisher information

$$F = \frac{2(I_0 + \sigma_{\mathrm{read}}^2) + 1}{2(I_0 + \sigma_{\mathrm{read}}^2)^2} \left(\frac{\partial I_0}{\partial \hat{\Theta}}\right)^2. \tag{3.9}$$

Assuming that we can approximate the differential in Eq. (3.9) with finite differences as $\frac{\partial I_0}{\partial \hat{\Theta}} = \frac{I(\Delta y) - I(0)}{\Delta y}$ and I_0 as the scattered intensity of an unperturbed ring $I(0)$, we can estimate the Fisher information content of a sensing experiment from an unperturbed and perturbed measurement, for which we already acquired all the relevant data in the previous sections.

We now quantitatively compare Fisher information content between an angle integrated scattering measurement and Fourier space measurement. To keep all experimental parameters such as integration time, incident laser power and detector efficiency a constant in the comparison, we estimate the Fisher information in the two different measurement strategies from our Fourier space data alone, constructing spectral data by software integration over angle. Figure 3.5 summarizes the workflow to arrive at quantitative values for the Fisher information content. We start with raw Fourier images scattered by an unperturbed ($\Delta y = 0$ nm) and perturbed ring ($\Delta y = 50$ nm) with fixed asymmetry ($\Delta L = 80$ nm) and excited by a wavelength of 730 nm in figures 3.5a and 3.5b respectively. Following the red connector lines, from these two images we calculate an angle resolved Fisher information image by applying Eq. (3.9) onto the individual pixels of the images, with the result depicted in figure 3.5c. From this image we can see that Fisher information is directionally scattered in Fourier space, with the majority of the information scattering into the negative k_y/k_0 viewing direction. This can be explained by again inspecting figure 3.4h, which is the differential intensity image that corresponds to the Fisher information radiation pattern as shown in 3.5c, from which we can see that indeed the majority of the differential counts are scattered into the negative k_y/k_0 direction. A recent work [144] has shown that the shape of these information patterns can be understood from a near-field description using so-called information sources, which radiate information instead of energy, and poses the interesting design question how antenna theory could be exploited to engineer these information patterns at will. To connect a single information value to this radiation pattern, we make use of the additivity of the Fisher information, and sum all the values in the Fisher information radiation pattern. To correct for the reduction in information due to fabrication noise, we apply the same workflow onto a pair of Fourier images scattered from similar metarings, and subtract the corresponding result from the Fisher information of a perturbed/unperturbed ringpair to arrive at the final information estimate, represented by the red diamond in figure 3.5. To estimate the information content of a simple spectral measurement (blue network) we first sum the individual Fourier space images in figures 3.5a and 3.5b. This operation simulates the measured count value a single pixel on a spectrometer would detect for the relevant excitation wavelength. We finally apply Eq. (3.9) onto this pair of values to arrive at the final information estimate represented by the blue circle.

In figure 3.5d, we showcase the full comparison in information content between an angle integrated and angle resolved measurement. For this, we determined Fisher information values for a fixed perturbation strength of $\Delta y = 50$ nm, while varying the excitation wavelength and the asymmetry ΔL. In the same figure, the center and width of the grey vertical bars indicate the res-

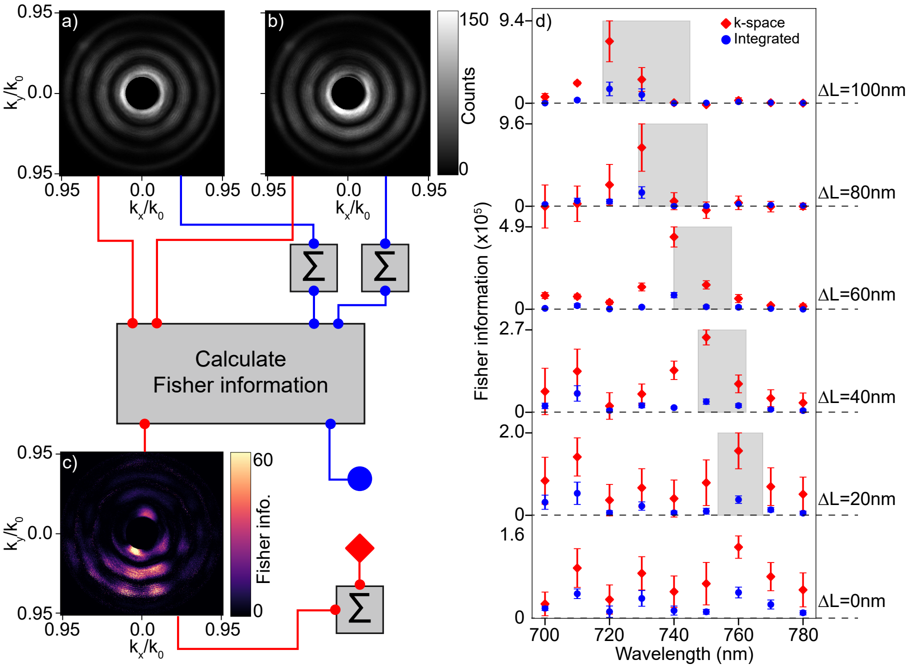

Figure 3.5: Information comparison between angle integrated and angle resolved scattering measurements. Panels (A) and (B) show raw data of unperturbed ($\Delta y = 0$ nm) and perturbed ($\Delta y = 50$ nm) Fourier space images for a metaring with fixed asymmetry of $\Delta L = 80$ nm, excited at a wavelength of 730 nm. These two images are processed through the red and blue networks in the figure to arrive at an information value for the angle resolved and angle integrated measurements respectively. Panel (C) shows the angle resolved Fisher information resulting from the pair of measurements of panels (A) and (B). Panel (D) shows the total Fisher information of angle integrated and angle resolved measurement as blue circles and red diamonds respectively, plotted versus excitation wavelength and for all realizations of the asymmetry ΔL. Datapoints and errorbars denote mean and standard deviation of a set of 4 similar individual metarings. The center and width of the grey bars denote resonance wavelength and linewidths extracted from dark-field spectra of unperturbed rings.

onance wavelengths and linewidths of unperturbed metarings respectively. It can be seen that the information content of both the angle resolved and angle integrated measurements peak at the Fano resonance, where the peak follows the same blue shifted trend versus increasing asymmetry ΔL as we have observed in the spectroscopic measurements of figure 3.2, corroborating the fact that sensing at resonance more efficiently detects a perturbation than sensing off-resonance from an information perspective. We further see that the information content of a Fourier space measurement is always higher than that of an angle integrated measurement, both on and off-resonance, where the information gain can be as high as sevenfold. From the scalebar we can finally observe that the maximum information content increases with increasing asymmetry ΔL, reaching a maximum at $\Delta L = 80$ nm. We speculate that this behavior can be explained by a trade-off in scattering strength of the metarings, figure of merit of the resonance shift per unit linewidth, and the finite bandwidth of our color filters, finding an optimum at $\Delta L = 80$ nm.

3.6 Conclusions

In summary, we have studied deeply subwavelength perturbations in Fano resonant dielectric metasurfaces, and experimentally demonstrated that an information gain in resonance based sensing experiments can be obtained when analyzing the scattered signal of the metasystem in Fourier space. We observed that the information gain is a consequence of resonant directional scattering of the metasurface induced by the perturbation, a feature that is not captured in conventional resonance based sensing schemes, and have theoretically discussed possible origins of this directional scattering by examining how a perturbation affects the system's fundamental eigenmodes. We quantitatively determined the information gain by calculating the Fisher information contents of both an angle resolved and angle integrated detection scheme assuming shot-noise and detector readout noise as dominant noise sources in the experiment. We estimated that an information gain as high as a factor of 7 can be achieved using the Fourier space sensing modality, which means that the exposure time or incident laser power can be reduced by this same factor to achieve similar sensing precisions as in conventional spectral based sensing protocols. This is appealing in sensing experiments where photon budget [143] and fast measurement times [10] play an important role.

Looking forward, we speculate that additional information about a perturbation can be retrieved by adding polarizing optics and interferometric tools in the detection setup to retrieve the full polarization state along with the phase of the scattered signal, such that a complete description of the scattered response is acquired. Besides, one could further control the external degrees of freedom on the excitation side by, for instance, polarization [126] and wavefront [74] shaping to achieve an optimally informative illumination. Such control, in combination with designer metastructures, might also open pathways towards arbitrary design of the information flow in Fourier space [144]. All in all, our work explored advanced sensing strategies that leverage the full potential of resonant metasurfaces, paving the way for more efficient, precise, and versatile sensing platforms.

Appendices

A Coupled dipole calculations

The metarings discussed in the main text are theoretically modeled by coupled point dipoles. For an isolated dipole, we use the dyadic Green's function [140] of a dipole $\mathbf{p}$ positioned at $\mathbf{r}_0$ in a homogeneous medium to describe the scattered fields at a probing position $\mathbf{r}_1$ as:

$$\overset{\leftrightarrow}{\mathbf{G}}(\mathbf{r}_0, \mathbf{r}_1) = \left(\overset{\leftrightarrow}{\mathbf{I}} + \frac{1}{k^2} \nabla\nabla \right) \frac{e^{ik|\mathbf{r}_1 - \mathbf{r}_0|}}{4\pi|\mathbf{r}_1 - \mathbf{r}_0|}, \tag{3.10}$$

such that

$$\mathbf{E}(\mathbf{r}_1, \mathbf{r}_0) = \omega^2 \mu \mu_0 \overset{\leftrightarrow}{\mathbf{G}}(\mathbf{r}_0, \mathbf{r}_1) \cdot \mathbf{p} \tag{3.11}$$

Here, $\overset{\leftrightarrow}{\mathbf{I}}$ is the unit dyad, ω is the driving frequency, $k = n\frac{w}{c}$ is the wavenumber in the medium, μ the permeability of the medium and μ_0 the free space permeability. For an ensemble of N coupled dipoles $\{\mathbf{p}_1 ... \mathbf{p}_N\}$ driven by an incident electric field $\mathbf{E}_{\text{exc}}$, the solution of the n'th dipole configuration can be described by a self consistent set of equations as:

$$\mathbf{p}_{\text{n}} = \alpha_n \left(\mathbf{E}_{\text{exc}}(\mathbf{r}_{\text{n}}) + \sum_{m \neq n} \overset{\leftrightarrow}{\mathbf{G}}(\mathbf{r}_{\text{n}}, \mathbf{r}_{\text{m}}) \cdot \mathbf{p}_{\text{m}} \right), \tag{3.12}$$

where α_n is the polarizability of the n'th dipole. This system of equations can be recast into a matrix form as

$$\begin{bmatrix} \mathbf{p}_1 \\ \vdots \\ \mathbf{p}_{\text{N}} \end{bmatrix} = M^{-1} \cdot \begin{bmatrix} \mathbf{E}_{\text{exc}}(\mathbf{r}_1) \\ \vdots \\ \mathbf{E}_{\text{exc}}(\mathbf{r}_{\text{N}}) \end{bmatrix}, \tag{3.13}$$

and

$$M_{i,j} = \delta_{i,j} \alpha_i^{-1} - (1 - \delta_{i,j}) \overset{\leftrightarrow}{\mathbf{G}}(\mathbf{r}_0, \mathbf{r}_1). \tag{3.14}$$

Here, the $(3N \times 3N)$ matrix M is the coupling matrix of the system, and describes the interactions between all the dipoles in the system. The scattered fields of the ensemble of dipoles, and the optical quantities that result from this can thus be calculated by a matrix inversion of the coupling matrix M. We analytically model the static polarizabilities of the dipolar particles in the metarings as prolate spheroids [145], with a long axis L_0 of 300 nm and short axis W of 100 nm. These particles are positioned in an annulus of radius 1.5 μm, and every other particle in the annulus is reduced in length by $L_0 - \Delta L$, where $\Delta L = 100$ nm. The dielectric permittivity of the particles ϵ is set to 12, approximating that of silicon, while the surrounding medium is set to vaccuum $\epsilon_m = 1$. Radiation damping [146] is included to the static polarizabilities α_0 as $\frac{1}{\alpha} = \frac{1}{\alpha_0} - i\frac{1}{6\pi\epsilon_0}k^3$. Finally, we compute the eigenvectors and corresponding eigenvalues of the coupling matrix M to retrieve the eigenmodes of the coupled system.

B Sample design and nanofabrication

The dieelectric metarings in the main text were fabricated using the following procedure. A glass coverslip (Menzel-Gläser) with a thickness of 170 μm was sonicated for 10 minutes in H_2O and cleaned in a solution of base piranha ($NH_4OH/H_2H_2/H_2O$ = 1/1/5) at 75°C for 15 mins. After thoroughly rinsing excess piranha with H_2O, the sample was blown dry with N_2. A 120 nm layer of amorphous silicon (a-Si) was evaporated onto the cleaned coverslips using electron beam evaporation (Polyteknik Flextura M508 E) at a deposition rate of 0.1 nm/s. After an oxygen plasma descum process of 2 mins, a 60 nm layer of hydrogen silsequioxane (HSQ) was spincoated (CEE Apogee 200 Spin Coater) for 60 s with a speed of 8000 rpm and acceleration of 1000 rpm/s and baked for 2 mins at 180°C. A conductive aluminum layer of 10 nm was thermally evaporated (Polyteknik Flextura M508 E) at a rate of 0.05 nm/s. For alignment purposes of the electron beam (Raith), 50 nm gold nanoparticles were dropcasted in the corners of the substrate, after which the sample was exposed at 50kV acceleration voltage and an area dose of 1500 $\mu C/cm^2$. After exposure, the substrate was chemically developed in a solution of tetramethylammoniumhydroxide (TMAH) for 60 s at 60°C and rinsed with H_2O for 15 s. Finally, the substrate was etched (Oxford Plasmalab 80+) using a mixture of 10 sccm sulfurhexafluoride (SF_6), 15 sscm trifluoromethane (CHF_3) and 3 sccm O_2.

C Experimental setup

The experimental setup that is used to perform dark-field spectroscopy and Fourier scatterometry is depicted in figure 3.6. A supercontinuum laser (NKT Whitelase Micro) is coupled into a single mode optical fiber and collimated into a Gaussian beam. The beam is subsequently linearly polarized and clipped in size by a 500 μm pinhole. The pinhole is relay imaged by a pair of lenses into the pupil plane of a high NA (NA = 0.95) microscope objective, effectively reducing the NA of the illumination beam to approximately 0.18. The beam is then focused onto the sample plane such that a single metaring is entirely illuminated, after which the objective captures both the backreflection of the illumination and the scattered signal originating from the sample. In the dark-field spectroscopic measurement modality, the entire spectrum of the supercontinuum laser is illuminating the sample. Here, the direct reflection of the laser is filtered out by conjugating the pupil plane of the objective by a

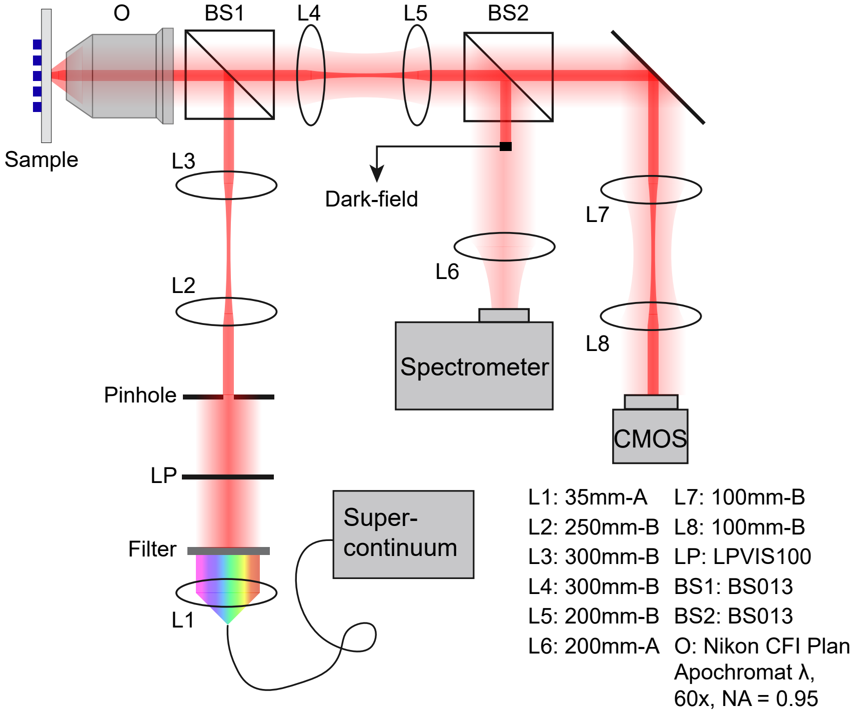

Figure 3.6: Experimental setup for dark-field spectroscopy and Fourier microscopy. Sketch of the complete experimental setup as used in the experiments from the main text. All lenses are achromatic (AC-254), and the indicated codes list the focal length in millimeters, followed by an A or B for the antireflection coating (Thorlabs nomenclature).

pair of lenses and placing a hard mask in this intermediate image plane, such that after the mask only scattered light is propagating through the system. This scattered signal is then focused onto the slit of a spectrometer (Andor Shamrock 303i) equipped with a cooled CCD (Andor iVac), after which a dark-field spectrum can be acquired. All spectra in the main text have been acquired with 10ms integration time and summing 100 spectra. For the Fourier scatterometry measurements, the illumination beam is color filtered by bandpass filters with 10nm bandwidth. The same scattered signal is captured by the microscope objective, where the pupil plane of the objective is now relay imaged onto a C-MOS camera (Basler, acA1920–40um). The direct reflection of the low NA illumination beam is now computationally clipped in a postprocessing step. In all the data shown in the main text, Fourier plane images are acquired at 500ms integration time. All lenses, polarizers and beamsplitters shown in the figure have been bought from Thorlabs, and their respective focal lengths and serial numbers can be found next to the sketch of the setup. Sample navigation is controlled by Thorlabs motorized actuators (Z812) along with K-Cube steppercontrollers (KST101), and a 3D nanopositioning piezo (PI Nanocube) for fine alignment.

D Camera calibration and noise characterization

To characterize the noise in our sensing experiment, we calibrated our image sensor based on a standard procedure [147]. First, we characterized the dark-noise of our camera by acquiring a series of images in complete darkness while varying the exposure time. From the resulting image we extract the noise by taking the standard deviation of the counts σ_c in the image, and plot the result of all these images versus the exposure time in figure 3.7a in a logarithmic plot. For high exposure times the noise follows a linear trend, which is verified by fitting a power law through the datapoints, resulting in the fitcurve $\sigma_c = (8.32 \times 10^{-7}) \cdot t^{0.99}$. This behavior is typical for high exposure times, where dark noise in the form of thermally induced photo-electrons are generated. For lower exposure times, the curve flattens towards a constant offset, which describes the read-out noise of our detector.

Next, we characterize the photon transfer curve of the detector at a constant exposure time equal to 500 ms (equal to the exposure time of all acquired images in the main text). To achieve a constant illumination profile, we place a 1 cm block of Teflon in front of the camera which acts as a diffuser, and illuminate the Teflon block with a halogen lightsource. We then acquire several images for varying illumination intensities, which we control by linear polarizers. The photon transfer curve is retrieved by plotting the standard deviation of the counts σ_c in the acquired images versus the mean of the counts μ_c, which is shown in figure 3.7b in a logarithmic plot. From the curve, we van discern three regimes. The first regime, for mean counts values

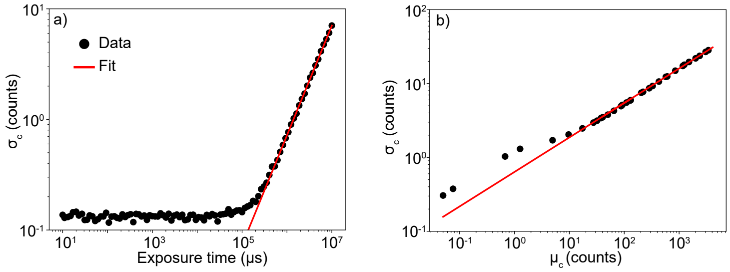

Figure 3.7: Camera calibration and noise characterization. Panel (A): Standard deviation of the counts in an image acquired in complete darkness versus exposure time. Panel (B): Standard deviation of the counts in an image versus the mean of the counts in the same image, acquired at a constant exposure time of 500ms. In every image, the illumination conditions are varied in intensity. The data in both panels are fitted by power laws.

higher than approximately 10 counts, we observe a trend which can be fitted by a powerlaw of $\sigma_c = 0.63 \cdot \mu_c^{0.47}$. This trend is reminiscent of Poissonian statistics, as the standard deviation scales with the square root of the mean, and thereby describes the shot-noise limited regime of the experiment. From the fit, we can extract the gain of the image sensor, which is equal to 2.52 e^-/DU. For mean count values below circa 5 counts per pixel the trend is still Poissonian, but with a ca. 2-fold higher prefactor (same slope, but constant offset in logarithmic plot). We attribute this to an automatic switch in gain settings at low count rates specific for this camera. Finally, for even lower mean count values, the noise again reaches the constant offset defined by the readout noise.

Chapter 4

Wavefront Selective Modal Excitations for Optimally Informative Sensing in Fano-Resonant Metasurfaces

Fano-resonant metasurfaces governed by quasi bound states in the continuum have recently sparked an enormous interest in the sensing community due to their spectacular sensitivity to nanoscale disturbances. Here, a plane wave or focused illumination is typically used to excite the quasi-BIC modes. In this chapter, we theoretically demonstrate how structuring an incident excitation leads to a gain in information about relevant nanoscale perturbations to be detected. We analyze the full eigenmode spectrum of a dielectric quasi-BIC metasurface, and uncover eigenmodes that are incompatible with trivial illuminations such as plane waves. By utilizing the concept of "maximum information states", that was recently developed by the wavefront shaping community, we engineer incident excitations that can selectively excite these quasi-BIC modes. By using information theory, we quantitatively demonstrate that such wavefront selective modal excitations can be more informative than conventional excitations based on plane waves.

4.1 Introduction

Optical sensing platforms form the backbone of many state-of-the-art metrology applications, ranging from gravitational wave detection [8], wearable sensors for health monitoring [148, 149] and environmental quality control [150]. Here, light is used as a probe that interacts with a physical system, and is subsequently used to read out relevant fundamental parameters of that system. In these applications, an efficient interaction between the incident probe light and the object to be sensed is vital to obtain an informative measurement. This is a highly non-trivial prerequisite in the realm of nano-optical sensing, where the goal is to retrieve information about specimens on deeply subwavelength length scales. In this regime, the intrinsic light-matter interaction strengths are often insufficient to generate a responsive and detectable sensing signal. Advances in several nanofabrication techniques have allowed to engineer structures that can manipulate incident probe fields that drastically enhance light-matter interactions on the nanoscale. For example, single metallic [14, 151] and dielectric [15, 152] nanoparticles, whose response is dictated by the resonant oscillation of, respectively, free and bound electrons, have been shown to efficiently transduce propagating far-field radiation into locally enhanced near-field hotspots. These nano antennas [14] have already improved the response in various nanoscale sensing experiments related to, among others, the detection of fluorescence [153], surface-enhanced Raman scattering (SERS) [154, 155], photo thermal effects [156] and nonlinear signals [157, 158].

Even greater flexibility in shaping the local electromagnetic response of a system can be achieved with the use of metasurfaces [17, 18], which are two-dimensional sheets decorated by a collection of nanoparticles precisely tailored in size and shape. A powerful advantage of metasurfaces is that they can host strong collective and non-local effects between the nanoparticles, offering an enhanced sensitivity in sensing contexts. One of these collective effects is the so-called bound state in the continuum (BIC) mode [30, 159], which is a spatially extended and resonant state with an infinite quality factor (Q-factor) embedded within, yet completely decoupled from, the radiation continuum. A true BIC mode cannot be excited by far-field radiation, and in practical realizations a BIC is transformed into a quasi-BIC mode with a tunable Q-factor by introducing a structural symmetry breaking within the metasurface that opens up leakage channels to the far-field. Quasi-BIC mode excitation manifests itself as a sharp Fano lineshape [30] in far-field spectra such as scattering or reflection spectra, and leads to enhanced local fields within the plane of the metasurface. Indeed, recent works have shown that these properties render quasi-BIC metasurfaces as sensors with spectacular sensitivity to nanoscale refractive index changes in the form of biomolecules [32, 33, 160].

While nanoparticles and metasurfaces have fostered great innovations in

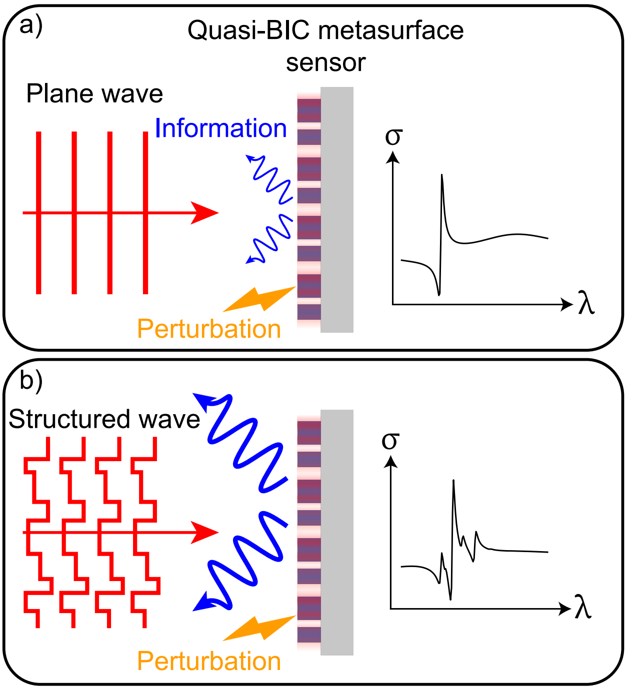

Figure 4.1: Quasi-BIC metasurface sensing with structured excitations (A) A conventional metasurface quasi-BIC mode is excited by a plane wave. The sensitivity of the quasi-BIC mode generates information about a nanoscale perturbation, which can be read out in the far-field. (B) A structured wave selectively excites quasi-BIC modes that are incompatible with plane wave illuminations, providing an increase in information about the perturbation.

sensing applications by shaping the local near fields at the nanoscale, recent advances in the field of wavefront shaping [49, 161] allow for the flexible tayloring of far-field propagating modes of radiation with the use of spatial light modulators (SLMs) and digital mirror devices (DMDs). The central challenge of this field is to optimize the response of a complex environment, that usually cannot be engineered in itself, by supplying an external structured far-field excitation that optimally interacts with the environment. Albeit originally utilized to improve focusing [50, 162] and imaging [52, 163] capabilities through opaque media, wavefront shaping has recently also been exploited to optimally sense parameters in highly complex and disordered environments by maximizing the Fisher information generated by these parameters. [74, 141, 142].

Although the domains of quasi-BIC metasurfaces and wavefront shaping show great promise in enhancing sensing performances by respective structuring of the underlying environments and excitation schemes, combining concepts from both fields to provide a structured excitation that optimally interacts with a quasi-BIC mode could pave the way towards optimal nanoscale sensor designs. It has recently been demonstrated that quasi-BIC mode excitation is governed by strict selection rules derived from the symmetry properties of the metasurface [164], which thereby set specific requirements on far-field excitation schemes. In fact, by exploiting very specific structural symmetry features, quasi-BIC modes can be engineered that are very selective to particularly structured incident wavefronts [165]. These works highlight the importance of structuring the excitation in efficient quasi-BIC mode excitation. However, the impact of combining optimally structured far-field excitations with a resonant quasi-BIC metasurface on nanoscale sensing experiments, and how such excitations should be designed based on the fundamental modes of the meta system, have hitherto not been explored.

In this chapter, we theoretically study optimally structured complex excitation modalities in combination with dielectric quasi-BIC metasurfaces. We find that structured excitations can lead to wavefront selective modal excitation that are incompatible with conventional illumination schemes, such as plane wave illuminations, and that these selective excitations could offer an enhanced performance in a sensing context, as conceptually depicted in Figure 4.1. To retrieve these optimally structured excitations, we utilize the concept of ”maximum information states” [74, 141] recently developed by the wavefront shaping community for precise parameter estimations in disordered systems, and expand these states into the realm of structured meta systems. Finally, by using information theory, we quantitatively determine how much information a structured excitation generates about a relevant nanoscale parameter to be sensed.

4.2 Metasurface eigenmodes

The resonant system that we will theoretically study in this work is depicted in figure 4.2a. The meta system is composed of dielectric silicon nanorods positioned in a ring, in which the long axis of the rods is aligned parallel to the radial direction of the ring. A recent study [137] has shown that these meta rings support radial BIC modes, which can be excited by far-field radiation and turned into quasi-BIC modes by introducing a structural symmetry breaker. Here, the symmetry breaker ΔL corresponds to a length mismatch between every other rod in the ring, as indicated in figure 4.2a. Quasi-BIC mode excitation manifests in the form of a sharp Fano lineshape in observables such as scattering spectra, and the enhanced sensitivity at the resonance condition can then be exploited to sense perturbations on the nanoscale. For the sake of concreteness, in this work we focus on a specific perturbation in the meta ring, and make a choice that is inspired by problems that are encountered in state-of-the-art semiconductor chip manufacturing processes

[10, 84], where misalignments down to the sub-nanometer scale can already lead to malfunctioning chips. The resonant meta rings could thus be exploited as telltale scattering sensors that report on the strength of the misalignment to be monitored. The specific perturbation relevant to this paper is defined in figure 4.2b, and corresponds to an upward shift of every other nanorod in the ring by Δy. Such perturbations for instance occur in microchip manufacturing, when devices are 'interlaced', i.e., placed in the same sample layer using different lithography exposure steps. We note that the results of this work are by no means restricted to this specific form of perturbation and may also be applied to sense other forms of nanoscale disturbances, such as monitoring environmental refractive index changes or the presence of molecular species.

To theoretically describe the response of the meta rings, we make use of a home-built coupled dipole model, of which the theoretical principles are layed out in Appendix A. In short, the individual nanorods within the meta ring are approximated by dipolar point particles described by a polarizability tensor $\overleftrightarrow{\alpha}_i$. By using the knowledge of the positions and polarizability tensors of all participating particles, an interaction matrix M can be constructed, which describes the physics of all dipole-dipole coupling mechanisms. Upon excitation by an external driving field $\mathbf{E}_{\mathrm{ext}}$, the collection of particles is excited and an ensemble of coupled dipoles $\mathbf{p}_{\mathrm{i}}$ can be calculated by inverting the interaction matrix M. Here all multiple scattering events between the particles are self-consistently taken into account. We model the individual nanorods by prolate ellipsoids with major axis $L = 240$ nm and minor axis $W = 100$ nm, which are described by an analytically known polarizability tensor [145]. In the following calculations, the radius R of the meta ring is set to $R = 1.5$ μm, the number of particles N in the ring is $N = 48$, $\Delta L = 50$ nm and $\Delta y = 1$ nm unless otherwise stated.

The whole notion of exciting a quasi-BIC mode for sensing requires a sufficient spatial overlap between the external driving field $\mathbf{E}_{\mathbf{ext}}$ and the relevant fundamental mode at play. To start the discussion, let us recuperate some well-known facts by considering, for instance, excitation by a y-polarized plane wave normally incident onto the meta ring. Figure 4.2c shows the resulting scattering cross section of the meta ring using these illumination conditions. A single Fano lineshape is evident, which can be described by a 2 mode interference effect between a super-radiant "bright" mode $\mathbf{p}_{\mathrm{bright}}$, i.e., a mode that can radiate efficiently into the far-field, and a sub-radiant "dark" mode $\mathbf{p}_{\mathrm{dark}}$, with an inhibited coupling to the far-field. This is the well-known Fano resonance in photonics [26]. The two relevant modes are visualized in the inset of Figure 4.2c, where both $\mathbf{p}_{\mathrm{bright}}$ and $\mathbf{p}_{\mathrm{dark}}$ have a non-zero overlap with $\mathbf{E}_{\mathrm{ext}}$. In the case of $\mathbf{p}_{\mathrm{bright}}$ this is evident, since $\mathbf{p}_{\mathrm{bright}}$ and $\mathbf{E}_{\mathrm{ext}}$ are both odd in parity. By virtue of the asymmetry ΔL, a small net dipole moment is present in the even parity $\mathbf{p}_{\mathrm{dark}}$, which therefore generates an overlap with $\mathbf{E}_{\mathrm{ext}}$. To obtain the highest amount of information about the perturbation Δy in a sensing experiment, the wavelength can now

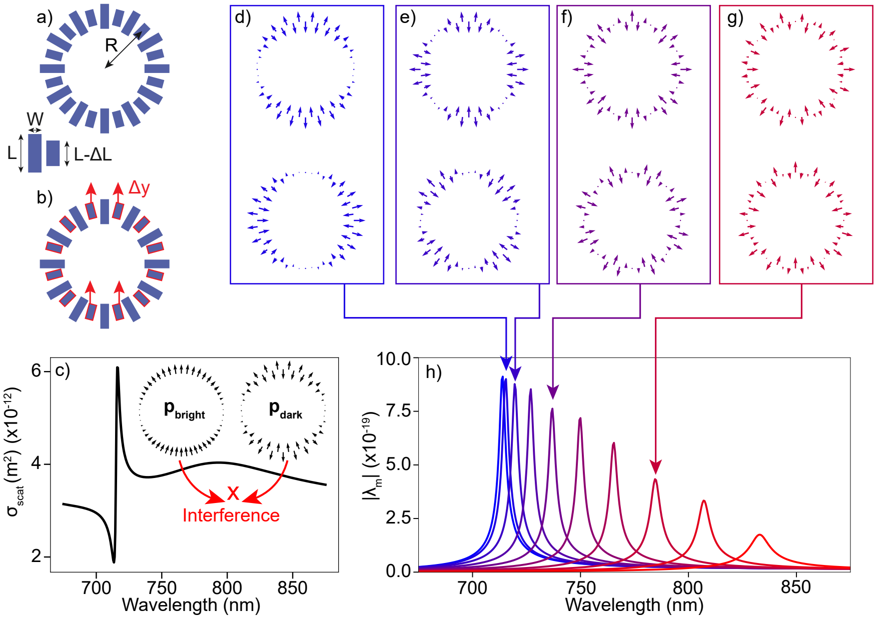

Figure 4.2: Eigenmodes of the metasurface scattering sensor. Panels (A) and (B) denote unperturbed respectively perturbed versions of the resonant metasurface scattering sensor. The perturbation corresponds to an upwards shift of every other meta atom in the ring by Δy. (C) Scattering cross section of the meta ring for a y-polarized plane wave excitation, normally incident onto the ring. The inset depicts the dominant eigenmodes responsible for the Fano interference. (D)-(G) Exemplary dipole configurations of the dominant eigenmodes in the meta ring. (H) Absolute value of the eigenvalue versus wavelength of a series of dominant eigenmodes. The arrows indicate which eigenmode profiles correspond to which eigenvalue spectrum.

be tuned to resonance (approximately 710 nm) to optimally make use of the high sensitivity of the quasi-BIC mode.

A surprising observation is that the established $\mathbf{p}_{\mathrm{bright}}$ and $\mathbf{p}_{\mathrm{dark}}$ that are responsible for the commonly observed Fano resonance under normal incidence are in fact neither the only eigenmodes of the system, nor the only high-Q BICs. To gain a complete picture of all the eigenmodes in the meta ring, we perform an eigenvalue decomposition on the interaction matrix M, from which we can extract all relevant eigenmode profiles $\tilde{\mathbf{p}}_{\mathrm{m}}$ and corresponding eigenvalues λ_{m}. A selection of the eigenmodes with the highest eigenvalues is visualized in Figures 4.2d-4.2g, along with the magnitude spectrum of the corresponding eigenvalues λ_{m} in figure 4.2h. These eigenvalues represent how strongly each collective eigenmode $\tilde{\mathbf{p}}_{\mathrm{m}}$ can be excited by an external field $\mathbf{E}_{\mathrm{ext}}$, provided there is sufficient overlap between $\tilde{\mathbf{p}}_{\mathrm{m}}$ and $\mathbf{E}_{\mathrm{ext}}$, and can be regarded as modal polarizabilities. The complete set of eigenmodes corresponding to all eigenvalue spectra is shown in Appendix B. It can be seen that the retrieved eigenmodes come in degenerate pairs which are mutually rotated, highlighting the high symmetry conditions of an unperturbed meta ring. Except for the dark mode that we have already encountered in Figure 4.2c, Figures 4.2d-4.2g also depict other types of even parity eigenmodes with a seemingly increasing envelope modulation frequency along the circumference of the meta ring. This spatial change in eigenmode shape leads to a corresponding redshift in eigenmode resonance frequency, as can be be observed from the spectra in Figure 4.2h. A crucial difference between the modes in Figures 4.2e-4.2g from the dark modes shown in Figure 4.2c and 4.2d is that the former modes have *zero* overlap with a plane wave excitation. This is the fundamental reason why these eigenmodes do not manifest as Fano lineshapes in the scattering spectrum of Figure 4.2c. However, from the eigenvalue spectra in Figure 4.2h it can be seen that these modes possess all the desirable properties of quasi-BIC modes, such as tunable high Q-factor resonances accompanied by strong polarizabilities, and could thereby be exploited as potentially informative excitations to probe Δy. We note that such modes, incompatible with plane wave excitations, are not necessarily unique to this specific meta ring geometry and might also be found in other types of nanophotonic structures, such as metasurfaces composed of periodic square lattices, oligomers of nanoparticles and even single nanoparticles [134]. The key questions we would like to tackle in the following sections is how these modes could be addressed by supplying a designer structured excitation $\mathbf{E}_{\text{ext}}$ with a non-zero spatial modal overlap, and to quantify how much information about the perturbation can be gained by such selective modal excitations.

4.3 Wavefront shaping pipeline

The external degrees of freedom offered by wavefront shaping offer an ideal toolbox to suitably structure the incident field and to offer the necessary modal overlap to excite the modes discussed in the previous section. To this end, we have developed a numerical wavefront shaping pipeline, which is schematically visualized in figure 4.3. We imagine a scenario in which a meta ring is interrogated in a Fourier microscope, with a liquid crystal spatial light modulator (SLM) in the excitation path, as sketched in Figure 4.3b. In the calculations, we modulate the amplitude and phase of an incident wavefront within a single polarization channel (y-polarization), as SLMs typically operate just for one polarization channel. Figure 4.3a shows an exemplary complex modulation map encoded onto an incident wavefront, where complex values are represented by a color wheel. Here, the hue is connected to the phase, and the brightness is connected to the amplitude. This color wheel visualization is used to represent complex fields throughout remainder of the paper. Individual pixels in the incident wavefront correspond to individual plane waves with different in-plane wave vector components, which are subsequently focused onto the sample consisting of the dielectric meta ring scattering targets. Figure 4.3d shows the y-component of the corresponding complex structured excitation field in real space relative to the dipole positions in the meta ring, as indicated by the gray circles. Due to focusing, the full vectorial excitation field will also contain components along the x- and z-directions, but these components are an order of magnitude smaller in amplitude than the y-polarized component. This excitation field excites dipole moments in the dielectric meta ring, which are governed by the eigenmodes discussed in figure 4.2, and the scattered far-fields of these dipole moments are subsequently calculated and converted into far-field angle resolved intensity images $I(\hat{\mathbf{k}})$, which will be the relevant signal to read out perturbations. In order to mimick a realistic experimental dark-field scattering detection scheme, we utilize a low numerical aperture (NA) illumination, while we calculate the scattered fields in a high NA region that falls outside the low NA illumination region, as shown in Figure 4.3c. The recorded dark-field intensity images are shown in Figures 4.3e and 4.3f, which correspond to the scattered far-field signals of an unperturbed $I_0(\hat{\mathbf{k}})$ ($\Delta y = 0$ nm) and perturbed $I_{\Delta y}(\hat{\mathbf{k}})$ ($\Delta y = 1$ nm) ring, respectively.

To determine how much information a specific calculated far field signal contains about the perturbation at hand, we calculate the Fisher information content of the far-field scattered signal. Suppose we have access to a dataset X, which in an experimental setting will be unavoidably corrupted by noise, and which in our case corresponds to the far-field scattered intensity patterns of Figures 4.3e and 4.3f. The Fisher information F relates to the best sensing precision σ_θ with which perturbations θ can be estimated from inherently noisy data X according to the Cramer-Rao bound

$$\sigma_\theta \geq \frac{1}{\sqrt{F}} \tag{4.1}$$

and is defined as [11]

$$F = E\left[\left(\frac{\partial \ln p(X;\hat{\Theta})}{\partial \hat{\Theta}}\right)^2\right], \tag{4.2}$$

where $p(X;\hat{\Theta})$ denotes the probability of measuring a dataset X given a perturbation strength $\hat{\theta}$, and $E[.]$ is the expectation operator. We assume that shot-noise is the dominant noise contribution in a potential experimental setting. The probability density function $p(X;\hat{\Theta})$ is then described by a Poisson distribution, and it can be shown that the Fisher information is described by the following expression:

$$F(\hat{\mathbf{k}}) = \frac{1}{I(\hat{\mathbf{k}})}\left(\frac{\partial I(\hat{\mathbf{k}})}{\partial \hat{\Theta}}\right)^2. \tag{4.3}$$

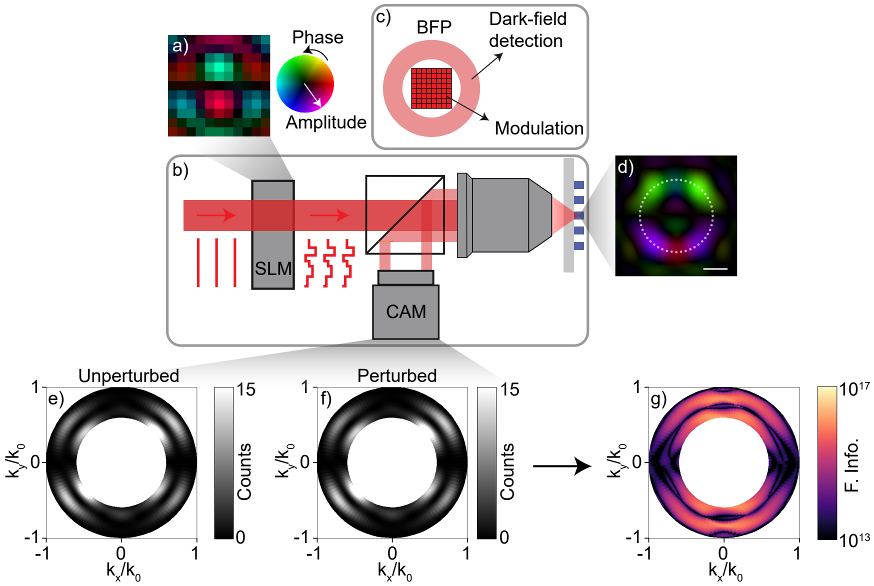

Figure 4.3: Numerical wavefront shaping pipeline (A) Complex modulation map corresponding to a modulated incident wavefront. Complex values are represented by a color wheel, where the hue indicates the phase, and the brightness indicates the amplitude of the wavefront. (B) Cartoon of the numerical wavefront shaping setup. The SLM indicates complex modulation of an incident wavefront, the objective focuses the incident wavefront onto the sample plane, after which a camera detects the far-field scattered intensity originating from the sample (C) Schematic of the illumination and detection modes in the calculations, mimicking dark-field detection. (D) Complex excitation map in real space corresponding to the modulation of panel (A). The gray circles indicate the positions of the dipoles in the meta ring, and the scalebar corresponds to 1 μm. (E) and (F) Scattered far-field intensity images of an unperturbed and perturbed meta ring. (G) Far-field Fisher information map corresponding the signals of panels (E) and (F).

If the derivative in Eq. (4.3) is approximated by finite differences, Eq. (4.3) emphasizes the fact that a pixel wise far-field Fisher information pattern $F(\hat{\mathbf{k}})$ can be constructed by using both unperturbed and perturbed far-field patterns $I(\hat{\mathbf{k}})$. The far-field Fisher information pattern corresponding to the unperturbed and perturbed intensity images of Figures 4.3e and 4.3f is shown in Figure 4.3g. This pattern reveals how much information is scattered into specific far-field detection angles $\hat{\mathbf{k}}$. Since Fisher information is additive, the total Fisher information of the calculation can be determined by simply summing all values in the Fisher information pattern $F(\hat{\mathbf{k}})$. Using this information theoretical formalism, we can now quantify how informative each individual incident wavefront is, and it is our objective to find the wavefront that maximizes the total Fisher information to sense perturbations Δy.

The problem of finding these so-called maximum information states has already been tackled in several works, for instance by using non-linear optimization algorithms [142, 143, 166, 167] or by determination of the (partial) scattering matrices of the system [74, 141]. In this work, we utilize the algorithm proposed in Ref. 141, which retrieves the illumination that maximizes the Fisher information assuming intensity-only signals. In brief, the algorithm exploits higher order tensors which are constructed from the partial scattering matrices of the sample under study and provides a convenient solution based on linear algebra, even though the dependence between the calculated far-field intensities and the excitation fields is quadratic. We thereby determine the partial scattering matrix of a meta ring scattering target H_{ij}, along with its derivative with respect to perturbations $\partial_\theta H_{ij}$, and construct the higher order tensor $W_{ijk} = \partial_\theta(H^*_{ij}H_{ik})$. The wavefront that maximizes the Fisher information can then be found by performing a best rank-one approximation of W_{ijk}. The complex pattern shown in Figure 4.3a is the resulting wavefront after applying this tensor based optimization scheme at a wavelength of 710 nm. At this wavelength, the modes shown in Figures 4.2c and 4.2d are most dominant in the scattering response of the meta ring. Therefore, one intuitively expects that the optimum illumination provides the best spatial overlap with the dominant mode at play in order to fully exploit the high sensitivity at resonance, and that these maximum information illuminations could be used as a tool to selectively excite modes incompatible with trivial excitation schemes.

4.4 Optimum illuminations and selective modal excitations

To evaluate whether optimally informative illuminations correlate to selective modal excitations within the meta ring, we calculate optimum wavefronts to sense Δy for a range of different wavelengths covering the spectral regime of Figure 4.2h. The resulting complex excitation maps in the sample plane are depicted in Figures 4.4a-4.4c, for wavelengths of 710 nm, 730 nm, and 750 nm, respectively. At these wavelengths, we expect that different eigenmodes will dominate the scattering response according to Figure 4.2h. For comparison, a more trivial excitation map, corresponding to a softly focused beam at 750 nm, is visualized in Figure 4.4d. First, it can be seen that the magnitude of all optimally informative excitation fields is strongest at the actual positions of the dipolar scatterers, providing a ring-shaped illumination pattern. This is logical, since the interaction with the excitation field and the scattering sensor should be maximized to obtain the most informative measurement. Second, strong modulations within the optimum excitations can be discerned, which are highly wavelength dependent. In other words, although in previous work metarings have mainly been studied as exquisite sensors under plane wave incidence, they can in fact be at least as informative under more complex illuminations. At first glance, these modulations seem to increase in number along the circumference of the ring for increasing wavelength, similar to the increase in modulations in the eigenmode configurations of Figures 4.2d-4.2g. This indicates that the excitation attempts to optimally couple to the dominant eigenmode.

To quantify this statement, we calculate the overlap between the optimum excitation $\mathbf{E}_{\mathrm{ext}}$ and all relevant eigenmodes $\tilde{\mathbf{p}}_{\mathrm{m}}$ according to $\langle \mathbf{E}_{\mathrm{ext}} | \tilde{\mathbf{p}}_{\mathrm{m}} \rangle$, and plot the results in Figures 4.4e-4.4h as blue vertical bars. Here, the mode indexing follows the convention as defined in Figure 4.6 in Appendix B. It can be seen that the optimum structured excitation fields are able to couple to a plethora of eigenmodes, contrary to the trivial illumination of Figure 4.4d, which can only efficiently couple to a single mode corresponding to the dark mode of Figure 4.2c. Moreover, the overlap spectrum changes dramatically for different optimum excitation fields. In the same Figures 4.4e-4.4h, we plot the change in magnitude of the eigenvalues $|\Delta\lambda_{\mathrm{m}}|$ corresponding to each mode

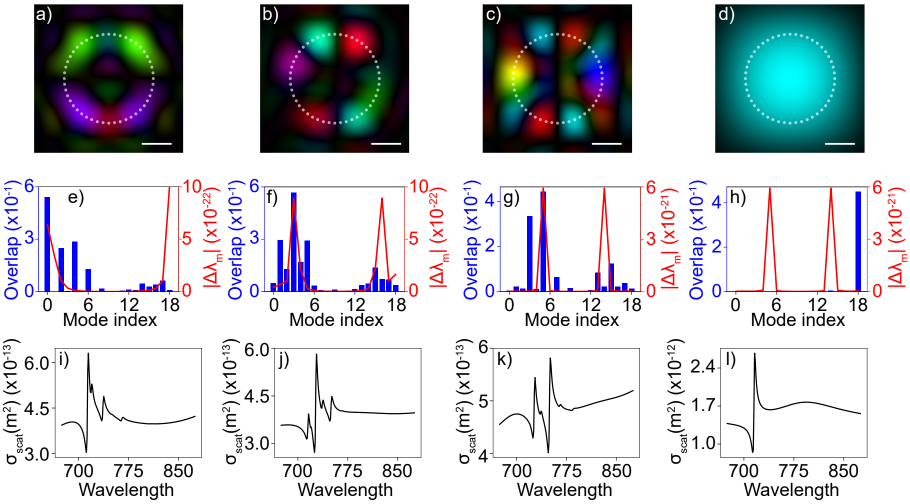

Figure 4.4: Selective modal excitations in Fano resonant meta rings. Panels (A)-(C) show complex excitation maps of the optimally informative illumination in the plane of the meta ring for a wavelength of (A) 710 nm, (B) 730 nm and (C) 750 nm. Panel (D) shows the complex excitation map of a softly focused beam at a wavelength of 750 nm. The same color wheel convention to visualize complex fields is used as in Figure 4.3. (E)-(H) Spatial modal overlap of the excitations in panels (A)-(D) with all dominant eigenmodes in the meta rings, indicated by the blue vertical bars. The indexing of the modes follows the same convention as Figure S1 of the SI. In the same panels, the change in magnitude of the eigenvalue per mode is highlighted by the red solid line at the same wavelengths as panels (A)-(D). (I)-(L) Scattering cross sections of an unperturbed meta ring corresponding to the excitations in panels (A)-(D).

due to the perturbation Δy as red solid lines, again for wavelengths of 710 nm, 730 nm, 750 nm and 750 nm, respectively. This plot indicates which modes are most sensitive in polarizability for different wavelength regimes, and is symmetric on the x-axis due to the degeneracies present in the eigenmodes. A high correlation between the differential modal eigenvalue spectrum and the modal overlap spectrum of the excitation can be observed. This verifies the hypothesis that optimally informative illuminations selectively enhance their coupling to the most sensitive fundamental modes of the system.

To highlight the effect of these optimally informative illuminations on the scattering response of the meta system, we calculate the scattering cross sections of the meta rings for every individual optimum excitation, and show the results in Figures 4.4i-4.4l. Instead of a single Fano lineshape that corresponds to the trivial excitations of Figures 4.4d and 4.2c, multiple Fano lineshapes are now discerned in the scattering spectrum for the complex structured excitations, which are a direct result of the enhanced modal coupling discussed in Figures 4.4e-4.4g. Comparing the shape of the individual spectra for different optimum excitations, we can further observe that the relative modulation depth of the Fano lineshapes in the spectrum is highly wavelength dependent, reflecting the enhanced and suppressed coupling to the underlying quasi-BIC mode. Here, the spectral position of the Fano lineshape with the highest modulation depth corresponds to that spectral region for which the excitation field was optimized for sensing. Finally, the overall modulation depth of the Fano lineshapes decreases for increasing wavelength, reflecting the decreasing polarizability of the eigenmodes with increasing wavelengths, as indicated by Figure 4.2h. These results underscore the potential of structured excitation schemes in combination with quasi-BIC metasurfaces to uncover modal excitations that are incompatible with conventional (plane wave) illuminations. It should be noted that the structural symmetry breaker ΔL is still crucial here for efficient modal excitation, without which no overlap with any far-field excitation scheme could be achieved.

4.5 Sensing precision

We next quantify how much information can be gained from these wavefront selective modal excitations, and compare the information content of an optimally structured excitation with that of more trivial illumination schemes. For this, we calculate the total Fisher information of the numerical sensing experiment according to Eq. (4.3) for three different excitations that are visualized in Figure 4.5a-c. These excitations correspond to a softly focused beam in Figure 4.5a, a focused orbital angular momentum (OAM) beam [168] in Figure 4.5b, which in this case provides a donut-shaped illumination containing a phase vortex that is compatible with the annular shape of the meta ring, and finally the excitation retrieved from the optimization algorithm in Figure 4.5c, respectively. For a fair comparison, we fix the incident average intensity for all excitations to 10^{15} photons per m^2. The Fisher information is calculated for the range of wavelengths in which the relevant eigenmodes of the meta ring are dominant, where the optimum excitation is recalculated for each individual wavelength. The Fisher information as a function of wavelength for the three excitation schemes is shown in Figure 4.5d. It can be observed that the total Fisher information of the optimal excitation is higher than the trivial excitations for all wavelengths, as expected from the optimization algorithm. The OAM excitation seems to be more informative than the focused excitation for a broad range of wavelengths as well. This can be explained by the fact that the OAM excitation has an intensity null exactly in the center of the ring, where no scattering particles are present. We can further see that all three excitations have a strong information peak at 715 nm, reflecting the fact that exciting the most sensitive eigenmode provides the most informative measurement. Even at the fundamental resonance, the optimum excitation outperforms the trivial excitation by a factor of 7 in information content. Besides the main peak at 715 nm, the optimum excitation shows multiple strong information peaks that correspond to the wavefront selective modal excitations, whereas the Fisher information for the trivial illuminations decreases dramatically in this spectral range. As can be seen, these selective excitations radiate a similar information content about the perturbation as the optimum excitation at the fundamental resonance, and selective excitations that address the non-trivial modes can provide even more information than the canonically used Fano resonance in the simple plane-wave excitation manifold.

We finally describe how these excitations, in combination with the scattered signal of the meta rings, could be used to perform precise estimations of potentially unknown perturbation strengths. For this purpose, it is necessary to define an unbiased estimator, which is an operation that translates noisy measured or calculated data into an estimation of the perturbation $\hat{\theta}$. The estimator $\hat{\theta}$ is termed unbiased if the average of $\hat{\theta}$ over the noise fluctuations equates the true perturbation θ. We assume that we are dealing with small perturbations down to the sub-nanometer scale, in accordance with modern semiconductor wafer metrology requirements. In this regime of small parameter variations, the far-field scattered signal $I_{\Delta \mathrm{y}}(\hat{\mathbf{k}})$ corresponding to a perturbation Δy can be described by a linear model according to:

$$I_{\Delta \mathrm{y}}(\hat{\mathbf{k}}) = I_0(\hat{\mathbf{k}}) + \Delta y \frac{\partial I_0(\hat{\mathbf{k}})}{\partial(\Delta y)} + W(\hat{\mathbf{k}}), \tag{4.4}$$

where $I_0(\hat{\mathbf{k}})$ is the far-field scattered signal corresponding to an unperturbed meta ring, $\frac{\partial I_0(\hat{\mathbf{k}})}{\partial \Delta y}$ is the change in scattered signal due to an infinitesimal perturbation, evaluated at $\Delta y = 0$ nm, and $W(\hat{\mathbf{k}})$ is a normally distributed vector that approximates the Poisson distributed noise in the signal. For the linear

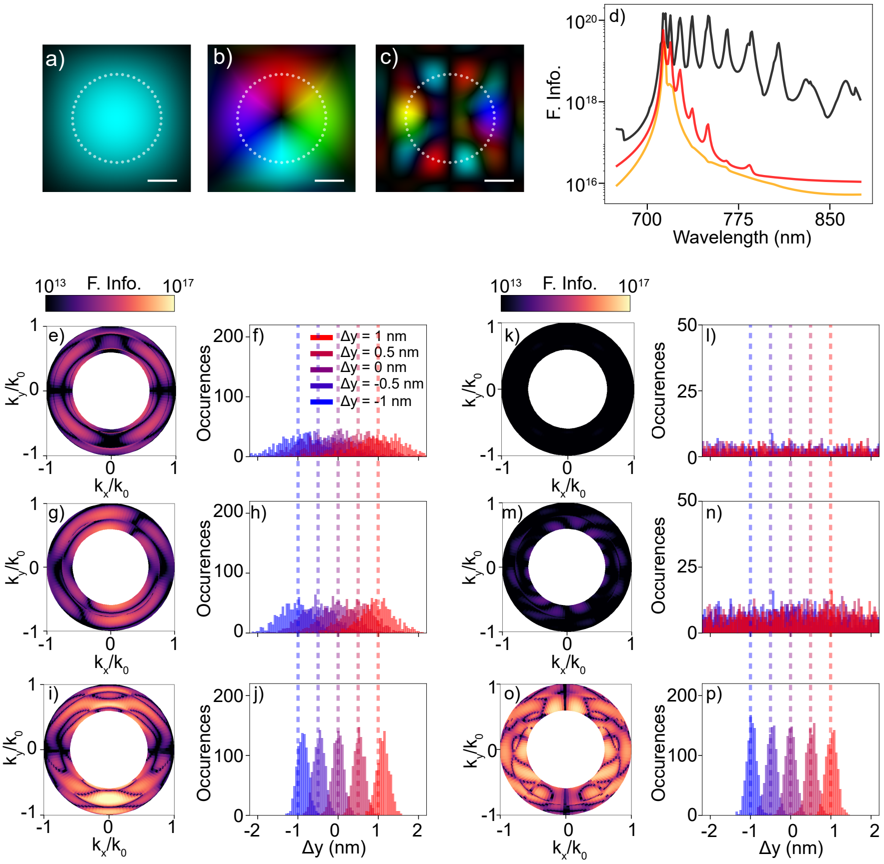

Figure 4.5: Information quantification and estimation precision. Panels (A)-(C) visualize complex excitation maps for (A) a softly focused beam, (B) an OAM beam and (C) the optimum excitation. The scalebar corresponds to 1 μm (D) Total Fisher information versus wavelength for the excitations of panels (A)-(C). The black, red and orange line denote the optimum, OAM and softly focused excitations, respectively. Panels (E), (G) and (I) show angle resolved Fisher information patterns of the meta rings for the softly focused, OAM and optimum excitations, respectively, where the excitation wavelength is set to 715 nm. Panels (F), (H) and (J) show estimation histograms of unknown perturbations using the softly focused, OAM and optimum excitations, respecively. (K)-(P): Same as panels (E)-(J), but at an excitation wavelength of 750 nm.

model described by Eq. (4.4), an expression for the unbiased estimator that reaches the Cramer-Rao lower bound can be derived as [11]:

$$\hat{\theta} = \frac{1}{F_0} \sum_{i=0}^{p} \frac{\partial I_0(\widehat{\mathbf{k_i}})}{\partial(\Delta y)} \left(\frac{I_{\Delta \mathrm{y}}(\widehat{\mathbf{k_i}}) - I_0(\widehat{\mathbf{k_i}})}{I_0(\widehat{\mathbf{k_i}})} \right), \tag{4.5}$$

where $\widehat{\mathbf{k_i}}$ corresponds to the detection angle at pixel i on the detector, p the total number of pixels on the detector, and F_0 the Fisher information corresponding to the two measurements in the differential $\frac{\partial I_0(\hat{\mathbf{k}})}{\partial \Delta y}$. If we again approximate the differential in Eq. (4.5) by finite differences, it can be seen that an estimation of unknown perturbations Δy can be carried out from a noisy far-field image $I_{\Delta \mathrm{y}}(\hat{\mathbf{k}})$ by first conducting a noise free calibration calculation on the scattered signal of an unperturbed meta ring, and of a meta ring at a known, small perturbation strength. In this calibration calculation, we set the known perturbation strength to 0.1 nm. We next calculate far-field scattered signals of the meta rings for the illumination conditions described in Figures 4.5a-4.5c at perturbation strengths of $\Delta y = -1$ nm, $\Delta y = -0.5$ nm, $\Delta y = 0$ nm, $\Delta y = 0.5$ nm and $\Delta y = 1$ nm, and generate 1000 different configurations of these images covered by shot-noise in order to simulate a sequence of measurements. We then apply Eq. (4.5) to these datasets to gather statistics on the estimation precision.

Figures 4.5e, 4.5g and 4.5i show angle resolved Fisher information maps $F_0(\hat{\mathbf{k}})$ of the calibration calculation for the softly focused, OAM and optimal excitation, respectively, where the excitation wavelength is set to 715 nm. Here, the increase in Fisher information can be recognized when an optimally structured excitation is offered. Figures 4.5f, 4.5h and 4.5j report on the corresponding estimation histograms of the noisy datasets under the respective excitation conditions. For the estimations of all datasets, the mean value of the estimation histograms is equal to the true perturbation strength, indicating accurate and unbiased estimations of Δy. For the estimations conducted on the datasets retrieved by the softly focused excitation in Figure 4.5f, a large overlap between individual histograms is seen, which means that the retrieved estimations are not precise. For the OAM excitation in Figure 4.5h, the individual distributions become narrower, while for the optimum excitation in Figure 4.5j five sharp peaks with minimum overlap between the histograms are seen, commensurate with a measurement with maximum Fisher information. We repeat this procedure in Figures 4.5k-4.5p at an excitation wavelength of 750 nm, detuned from the quasi-BIC mode at 715 nm. Estimating a perturbation at this wavelength using a softly focused or OAM excitation results in practically meaningless histograms from which no precise estimations can be made, which is a consequence of the dramatic decrease in Fisher information using these illuminations. When selectively exciting the underlying quasi-BIC mode, however, the 5 well defined estimation histograms are recovered, with a sensing precision comparable to the optimum excitation at 715 nm.

4.6 Conclusions

In conclusion, we theoretically study complex structured excitation modalities in quasi-BIC metasurface sensors, and show how such excitations lead to an information gain about the relevant perturbation to be sensed. We map the eigenmode spectrum of a dielectric Fano resonant meta ring, and, in addition to the well known q-BIC responsible for the Fano resonance under plane wave incidence, we uncover a plethora of hitherto unknown quasi-BIC modes that cannot be directly addressed by conventional plane wave illumination schemes. We show that optimally structuring an excitation using wavefront shaping allows for the excitation of such quasi-BIC modes, and that these selective modal excitations could be used as informative responses to probe nanoscale perturbations. We demonstrate that wavefront selective excitations could be even more informative than excitations by conventional illuminations within the same metasurface, prompting the metasurface community to think of the rich wavefront shaping toolbox as an extra degree of freedom to optimize the metasurface response.

Looking ahead, a single structured excitation could be engineered that efficiently couples to multiple quasi-BIC modes across a broad spectral range, which might be relevant in broadband sensing applications. Besides sensing, wavefront selective excitations might also find relevance in the field of nonlinear optics, where high harmonic signals could be selectively enhanced or suppressed depending on the incident wavefront. Instead of structuring an excitation in the spatial domain, state-of-the-art ultrafast pulse shaping methods [65] also allow to engineer the excitation in the temporal domain, which may pave the road towards optimal spatio-temporal coupling of excitations to quasi-BIC modes. All in all, our work highlights the untapped potential of wavefront engineering as a powerful lever to unlock the full potential of resonant metasurfaces, laying the groundwork for a new class of ultra-sensitive, spectrally versatile, and dynamically tunable photonic sensors.

Appendices

A Coupled dipole calculations

To theoretically model the meta rings discussed in the main text, we utilize a coupled point dipole model. Here, the i'th meta atom in the ring situated at position $\mathbf{r}_\mathrm{i}$ is approximated by a dipole source $\mathbf{p}_\mathrm{i}$, for which the scattered fields $\mathbf{E}(\mathbf{r}_1)$ at some position $\mathbf{r_1}$ can be calculated by evaluating the Green's function $\overleftrightarrow{\mathbf{G}}(\mathbf{r}_\mathrm{i}, \mathbf{r}_1)$ of the dipole in a homogeneous medium of refractive index n and permeability μ [140]:

$$\overleftrightarrow{\mathbf{G}}(\mathbf{r}_\mathrm{i}, \mathbf{r}_1) = \left(\overleftrightarrow{\mathbf{I}} + \frac{1}{k^2} \nabla\nabla \right) \frac{e^{ik|\mathbf{r}_\mathrm{i} - \mathbf{r}_1|}}{4\pi |\mathbf{r}_\mathrm{i} - \mathbf{r}_1|}, \tag{4.6}$$

where $\overleftrightarrow{\mathbf{I}}$ is the unit tensor and k the wavenumber in the medium. The scattered fields are then given by:

$$\mathbf{E}(\mathbf{r}_1) = \omega^2 \mu \mu_0 \overleftrightarrow{\mathbf{G}}(\mathbf{r}_\mathrm{i}, \mathbf{r}_1) \cdot \mathbf{p}_\mathrm{i}, \tag{4.7}$$

where ω is the driving frequency and μ_0 the permeability of free space. For the meta ring ensemble consisting of N coupled dipoles $\{\mathbf{p}_1 ... \mathbf{p}_\mathrm{N}\}$ driven by an incident excitation field $\mathbf{E}_\mathrm{ext}$, a solution of coupled dipoles is retrieved by solving the matrix equation

$$\begin{bmatrix} \mathbf{p}_1 \\ \vdots \\ \mathbf{p}_\mathrm{N} \end{bmatrix} = M^{-1} \cdot \begin{bmatrix} \mathbf{E}_\mathrm{ext}(\mathbf{r}_1) \\ \vdots \\ \mathbf{E}_\mathrm{ext}(\mathbf{r}_\mathrm{N}) \end{bmatrix}, \tag{4.8}$$

where

$$M_{i,j} = \delta_{i,j} \left(\overleftrightarrow{\alpha_\mathbf{i}} \right)^{-1} - (1 - \delta_{i,j}) \overleftrightarrow{\mathbf{G}}(\mathbf{r}_\mathrm{i}, \mathbf{r}_\mathrm{j}) \tag{4.9}$$

is the $(3N \times 3N)$ coupling matrix of the system that described all mutual interactions between the dipoles in the ensemble. In this expression, $\overleftrightarrow{\alpha_\mathbf{i}}$ is the dynamic polarizability tensor of the i'th particle.

B Eigenmode profiles and mode indexing

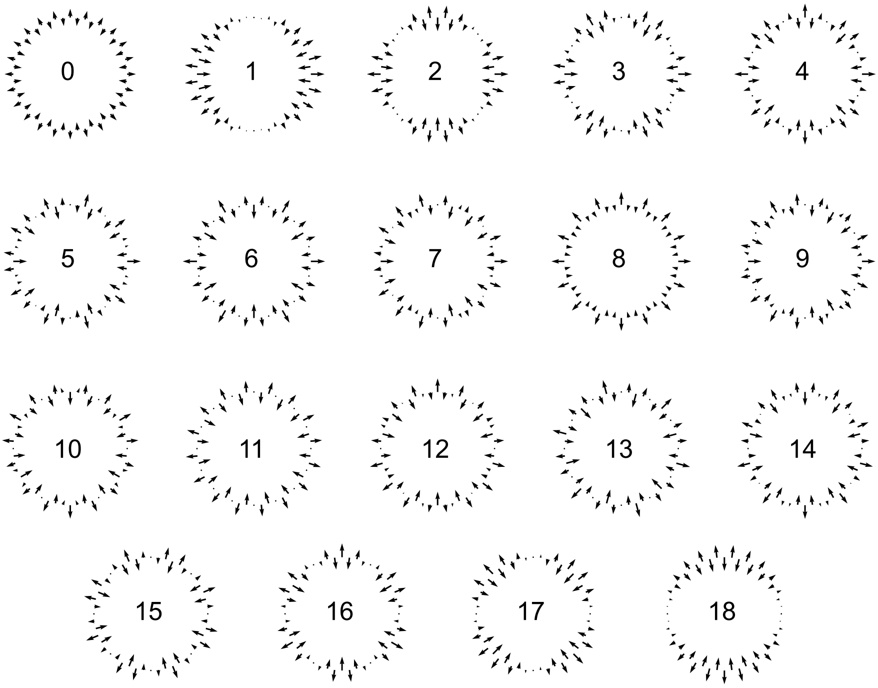

Figure 4.6: Complete set of dominant eigenmode profiles and corresponding mode indices.

Chapter 5

Wavefront Shaping for Optimal Extinction of Focused Light by Individual Nanoscatterers

Achieving high optical extinction contrasts in nanoparticle-based architectures is highly relevant in applications such as photodetection and light harvesting, and responds to the important problem of efficient in and out coupling in nanophotonic devices. In this chapter, we provide an innovative solution to this challenge by experimentally studying optimal extinction by individual and arrayed scatterers separated from a planar reflecting surface, while wavefront shaping the input light. We fabricate a series of periodic planar arrays separated from a back reflector with sizes varying from extended lattices to individual nanoparticles, and investigate how finite-size lattice effects influence attenuation of the reflectivity. We describe how the incident wavefronts of a tightly focused beam can be engineered to achieve optimal coupling to a single nanoparticle-on-mirror structure. Comparing these optimum incident wavefronts to analytical calculations of dipole scattering on a back reflector, we qualitatively demonstrate that the incident wavefronts are matched to the modal radiation patterns of the nanoscatterer in the presence of the planar reflector. Using these optimal illumination conditions, we demonstrate 70% extinction of a tightly focused beam by a single plasmonic nanoparticle, and up to 90% extinction in sub-wavelength 2x2 clusters of nanoparticles.

5.1 Introduction

Optical extinction describes the fraction of energy that is removed from a light beam due to scattering and absorption by atoms, molecules, or material structures, and provides a quantitative metric for the strength of different light-matter coupling mechanisms. Extinction includes elastic scattering, which consists of the redirection of incident light caused by an obstacle, as well as absorption by a material. Strong optical extinction is desirable in applications such as high-efficiency solar cells [169], optical sensors [170], modulators [171], and anti-reflection structures [172], which triggered an interesting question within the photonics community: how *complete* optical extinction can be achieved in designer materials. A hallmark example of complete optical extinction comes in the form of absorption by Salisbury screens [173, 174], in which a thin layer of resistive material is placed at a quarter wavelength from a back reflector. The essential physics of these Salisbury attenuators relies on in-phase superposition of incident and reflected light, which is therefore completely absorbed by the resistive sheet. Sparked by recent progress in the field of nanotechnology, Salisbury screens have been complemented by designer sub-wavelength spatially varying patterns to achieve perfect absorption in spectral regimes ranging from microwaves[175, 176] to near-infrared [177–180] and optical frequencies [181–183]. Such perfectly absorbing systems have also been connected to the notion of *coherent* perfect absorption [184, 185], leveraging light interference through coherent illumination by multiple waves, effectively leading to a time-reversed lasing scenario. [184]

In all the examples discussed thus far, extended thin films or spatially patterned surfaces are used as the extinction medium. A question that has intrigued the optics community for decades is how much extinction can be achieved from a finite collection of small particles or even single isolated nanoparticles. A crucial distinction is that, for infinitely extended surfaces, there is just a single input and output channel (an input plane wave and its specular reflection), so that perfect absorption can be easily achieved by arranging for perfect destructive interference of scattering with the direct reflection in the single output port. For finite objects, extinction is also defined as the destructive interference of scattered light and the incident field. However, finite scattering objects scatter light into all wave vectors components (i.e., into many more ports than just the direct incident beam). Consider the scenario of a single lossless and resonant nanoscatterer with dimensions much smaller than the light wavelength λ that is illuminated by an infinitely extended plane wave. Under these conditions, the nanoparticle can be described within the dipole approximation, and attenuation is quantified by the notion of extinction cross section C_{ext}. It can be shown [186] that the maximum achievable extinction cross section is given by:

$$C_{\text{ext}} = \frac{3}{2\pi}\lambda^2. \tag{5.1}$$

Due to the lossless nature of the nanoparticle, extinction is fully caused by scattering losses. A similar bound for the maximum attainable absorption cross section can be derived for lossy nanoparticles, which occurs under the so-called critical coupling conditions [186–188], in which scattering and absorption losses are made equal. Beyond the dipole approximation, superscattering nano-objects have been proposed that can surpass the limit of Eq. (5.1) by exploiting overlapping multipole resonances in subwavelength nanostructures [189].

Instead of plane-wave illumination, the coupling of incident light and a nanoparticle can be enhanced by tightly focusing the incident light to a diffraction-limited spot size. In this scenario, extinction is defined by the dimensionless fraction of power removed from the incident focus. Comparing the result of Eq. (5.1) with the typical cross section of a tightly focused beam, which is of the order of $(\lambda/2)^2$, one concludes that a single nanoparticle can, in principle, attenuate a large fraction of a focused beam. Indeed, numerical work has shown that a single oscillating dipole positioned in a homogeneous medium is able to cause up to 100% extinction of a focused light beam [190]. On the experimental side, studies have reported high extinction contrasts by dipolar transitions in single quantum emitters [191–193]. In parallel, several studies on the interactions of focused light fields with two level systems [190, 194–196] have argued that precise wavefront and polarization structuring of the incident focus is required to achieve an optimum coupling between excitation and scatterer, which would lead to a larger extinction. For instance, by illuminating a dipolar particle with a

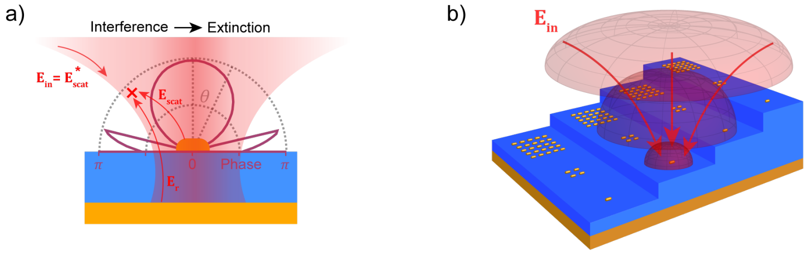

Figure 5.1: Experimental concept and sample architecture. (A) An externally applied, tightly focused incident field $\mathbf{E}_{\mathrm{in}}$ excites a dipolar nanoparticle-on-mirror system, after which the particle emits a scattered field $\mathbf{E}_{\mathrm{scat}}$ into the far-field. When the incident field is shaped such that it corresponds to the phase-conjugated (time-reversed) scattered field ($\mathbf{E}_{\mathrm{in}} = \mathbf{E}^*_{\mathrm{scat}}$), complete destructive interference between the back reflected field $\mathbf{E}_{\mathrm{r}}$ and the scattered field $\mathbf{E}_{\mathrm{scat}}$ can happen, leading to an optimum extinction scenario. (B) We fabricate plasmonic nanoparticle arrays separated from a back reflector by a dielectric spacer layer of variable thickness. The sizes of the arrays are varied from extended lattices, to finite-size patches, and single nanoscatterers.

strongly focused directional dipole wave, the particle can theoretically cause perfect extinction of the incident focused light beam [190, 196]. This can be explained from the viewpoint of time reversal symmetry: a nanoparticle emitting light into a dipolar far-field pattern would be most efficiently excited by a time-reversed field that matches this dipolar pattern, and experiments have been proposed [195] that offer two-sided dipolar illumination schemes that cover full 4π incident angles. This argument can also be recast in the language of destructive interference: by maximizing the similarity between the radiation pattern and the wavefront of the direct beam, one maximizes destructive interference and hence extinction. More recently, theoretical works [196, 197] have shown that positioning a single nanoparticle at an optimum distance from a reflective substrate can cause perfect extinction of a focused light beam, assuming optimal structuring of the incident field over 2π incident angles. The mirror limits the scattered wave to 2π instead of 4π steradian, easing the challenge of optimally structuring the incident field. In a way, these studies provide a single-particle analogue to Salisbury screens, in which the thin resistive layer is replaced by a single nanoscatterer. The crucial distinction here is the number of available ports: in the extended Salisbury screen, the incident field can only be directly reflected or transmitted in the zero-order channel, whereas a single nanoparticle is allowed to scatter light into a continuous angular spectrum. Note that this distinction can be extended to the interference argument as well: while Salisbury screens are designed to cause complete destructive interference between the direct specular reflection caused by the back mirror (which is the outgoing part of the incident wave) and the specular reflection of the resistive sheet, the radiation pattern of the single nanoparticle-on-mirror system causes complete destructive interference with its time reversed incident focus reflected by the back mirror. However, to the best of our knowledge, no experimental studies have been reported that investigate optimal extinction scenarios in single-particle-based Salisbury-screen platforms, nor examine how mode matching of the external illumination influences total extinction.

In this work, we study extinction in Salisbury-screen attenuators down to the single nanoparticle level, and experimentally demonstrate that wavefront engineering of an incident focused beam leads to optimum extinction scenarios. The concept is schematically depicted in Figure 5.1a. A dipolar nanoparticle situated above a back reflector is excited by an externally applied, tightly focused incident field $\mathbf{E}_{\mathrm{in}}$ and emits a scattered field $\mathbf{E}_{\mathrm{scat}}$ into the far field, of which the scattered phase is shown in a polar plot. When the incident field is shaped such that it is phase conjugated (which is the monochromatic equivalent of time-reversal) with respect to the scattered field (i.e., $\mathbf{E}_{\mathrm{in}} = \mathbf{E}^*_{\mathrm{scat}}$), complete destructive interference can happen between the back reflected incident field from the back reflector $\mathbf{E}_{\mathrm{r}}$ and the scattered field of the nanoparticle $\mathbf{E}_{\mathrm{scat}}$, which leads to an optimum extinction condition. As a starting point, we revisit the well-known perfect absorption phenomenon in extended particle arrays near Salisbury screens, after which we study how finite-size effects affect optimal extinction conditions when gradually reducing the array size all the way down to a single scattering nanoparticle. To this end, we have developed a high numerical aperture (NA) wavefront shaping protocol that allows us to precisely engineer wave vector components of a tightly focused beam, and demonstrate that time reversal of the radiation patterns of single nanoscatterers leads to optimum extinction conditions. Using this strategy, we demonstrate up to 70% extinction of focused light in single plasmonic nanoparticles, and 90% in sub-wavelength clusters of 2x2 particles.

5.2 Finite size effects

Figure 5.1b depicts the sample architecture used in our experiments. We fabricate plasmonic arrays consisting of gold nanorods with different sizes ranging from effectively infinite arrays, to finite-size patches containing a few nanoparticles and down to single nanoparticles. Specific nanofabrication procedures and parameters are discussed in Appendix A. In all designs, the length, width, and height of the nanorods are 100 nm, 50 nm, and 40 nm, respectively, and the arrays have a period of 200 nm. These values are in line with a recent literature study [183] and are chosen such that the dipolar resonances of the system are within the detection range of our experimental setup. Multiple copies of these arrays are patterned on a substrate, after which we deposit a dielectric SiO_2 spacer layer with a variable thickness ranging from roughly 200 nm to 640 nm in steps of 10 nm. The spacer layer is finally covered by a back reflector, yielding a nanoparticle-based Salisbury-screen platform. We also fabricate reflectors in the same plane as the nanoparticles, which allows us to accurately determine the variable spacer height by measuring the Fabry-Perot etalon resonances in the resulting mirror-spacer-mirror regions that are immediately adjacent to the arrays and particles under test (see Appendix C for details). Figures 5.2a-5.2d show scanning electron microscopy (SEM) images of typical arrays with varying sizes, which are taken before deposition of the dielectric staircase and mirror.

To probe the extinction properties of these particle array patches, we acquire reflection spectra as a function of spacer height while gradually reducing the array size to, ultimately, a single nanoscatterer. Our strategy to move from array measurements towards single particle extinction measurements is as follows. We start by measuring reflection spectra of very large 100x100 μm^2 arrays using near-normal illumination, revisiting literature results [183]. On this effectively infinite array, we then gradually switch the illumination conditions from near-normal incidence to high-NA tight focusing, which is required for single nanoparticle extinction studies, and investigate how the measured extinction depends on the NA of the incident focus. The high-NA focused illumination conditions are then used to probe finite array size effects.

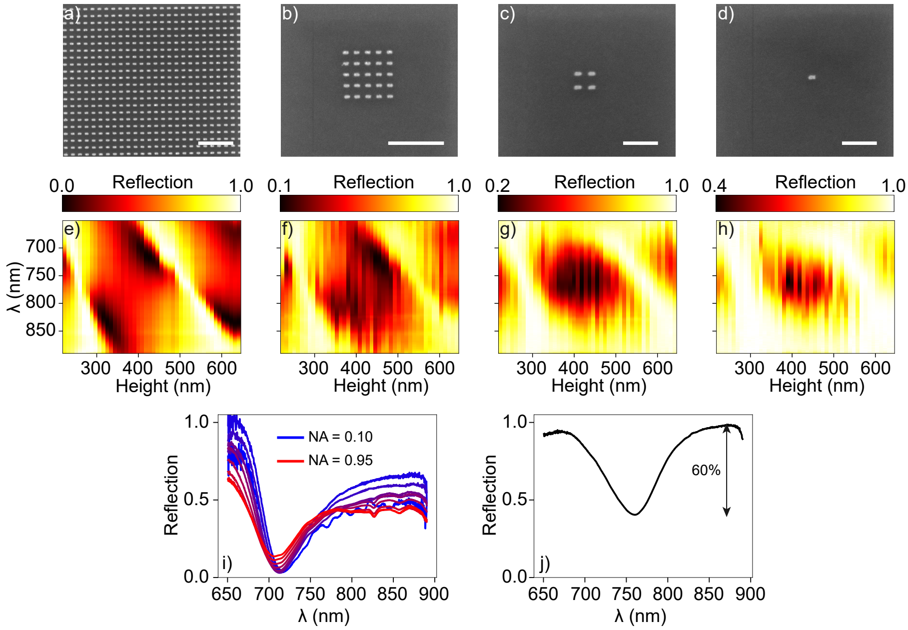

Figure 5.2: Optimal extinction in finite-size particle arrays on Salisbury screens. SEM images of arrays fabricated on a variable spacer height with an array size of (A) 100x100 μm^2; (B) 5x5 particles; (C) 2x2 particles and (D) a single particle. Scalebars correspond to 1 μm in panels (A) and (B), and 500 nm in (C) and (D). Panels (E)-(H) show experimentally measured reflection spectra as a function of spacer height for the arrays in (A)-(D) respectively. (I) reflection spectra captured on a 100x100 μm^2 separated by 427 nm from the back reflector, for different numerical apertures (NAs) in the 0.1-0.95 range. (J) Reflection spectrum of a single nanoparticle separated from the back reflector by 391 nm.

In all measurements, the polarization state of the incident beam is aligned parallel to the long axis of the nanorods. Details on the experimental setup and data acquisition parameters can be found in Appendix D.

We first turn our attention to reflectivity spectra acquired on the 100x100 μm^2 array with a pitch of 200 nm illuminated by a low effective NA of 0.1, as shown in Figure 5.2e. Every vertical slice in this image corresponds to a reflection spectrum acquired on a different array realization, separated by a different spacer thickness from the back reflector. It has been shown in an earlier work [183] that such *metasurfaces etalons* result in pairs of singular points of zero reflection/perfect absorption in the 2D parameter space spanned by the spacer height and the light wavelength, which are associated with topological phase singularities. These perfect absorption conditions originate from a hybridization of array plasmon resonances and Fabry-Perót etalon resonances. From the spectra of Figure 5.2e, we clearly observe such a singular pair of (nearly) null reflection points between spacer heights of 300 nm and 500 nm, approaching bright lines of near unity reflection corresponding to the etalon resonance conditions. These singular pairs are repeated indefinitely for higher spacer heights that lie outside the range of our fabricated sample. The small but finite wave vector spread that is associated with the incident NA results in a small residual reflection at the singular points.

To visualize the effect of incident NA on the extinction properties of such a 100x100 μm metasurface etalon around the normal-incidence perfect absorption condition, we acquire reflection spectra at a constant spacer height of 427 nm while gradually increasing the NA of the incident focus from 0.1 to 0.95, which is the maximum NA of our microscope objective. A gradual increase in residual reflection is observed when increasing the NA, highlighting the specificity of the singular points towards incident wave vectors. Using the high-NA focused illumination, we then progress to finite array patches, again acquiring reflection spectra on a range of different realizations of arrays with sizes of just 5x5 particles, 2x2 particles, and a single particle as a function of spacer height, and show the results in Figures 5.2f-h. We observe that, as the array decreases in size, the pair of singular points gradually vanishes into a single broad feature corresponding to the plasmon resonance of the single particle. This highlights the importance of extended lattices in the creation of topological singular points in the 2D parameter space. The minimum reflection value slowly increases as well for smaller array sizes. Nevertheless, a single plasmonic nanoparticle situated at the optimal height from the back reflector still causes a substantial extinction of almost 60 %, as highlighted by the single particle reflection spectrum in Figure 5.2j. Importantly, this extinction value is achieved with no particular tailoring of the incident wavefront to the radiation pattern of a dipole. The only shaping of the incident wave that evidently matters is to place the antenna in a field maximum of the standing wave formed by the incident focus and its reflection off the back reflector.

5.3 Wavefront optimization protocol

In this section, we describe how the extinction by single nanoparticles can be further optimized by tailoring the incident wavefronts. For this, we band-pass filter the illumination wavelength at 760 nm with a bandwidth of 10 nm, such that the excitation spectrally overlaps with the maximum extinction value as measured in Figure 5.2h. The experimental wavefront optimization workflow is depicted in Figure 5.3 for a single nanorod at the optimum distance from the mirror (391 nm) and is based on an iterative protocol commonly used within the wavefront shaping community [50]. This protocol allows for a more intuitive interpretation of optimization results than more sophisticated strategies such as the steepest-gradient descent method, although the latter might be an option for future implementations. Here, we rely on a set of

Zernike polynomials [198] as depicted in Figure 5.3a, which are widely used in the optics community (e.g., in phase retrieval experiments [199] and characterizing aberrations in imaging systems [200]). Zernike polynomials Z_n form a complete and orthogonal set of functions on the unit disk, which allows any wavefront φ to be decomposed as a linear combination those polynomials:

$$\varphi = \sum_n \alpha_n Z_n, \tag{5.2}$$

where α_n are the corresponding expansion coefficients. Finding the optimum wavefront that maximizes the extinction can thus be conveniently rephrased as finding the optimum contribution of each Zernike polynomial, thereby retrieving the optimum expansion coefficients α_n. To this end, we project a linear combination of Zernike polynomials on a spatial light modulator that we accumulate sequentially, i.e., by adding order after order and optimizing just the coefficient of the highest order term as we add it, as depicted in Figure 5.3b. This pattern is relay imaged onto the back-focal-plane (BFP) of the microscope objective, thereby modulating the phase of incident wave vectors, while the objective focuses the incident light onto a single nano scatterer. To obtain the optimum expansion coefficient for each n, we measure single particle reflectance values for a range of α_n by measuring reflected point-spread-functions (PSFs) of the focus both on and off (i.e., away from) a particle, continuously referencing these two measurements to each other to determine the extinction. Switching between on- and off-particle excitation is achieved by projecting an additional phase-ramp pattern on top of the Zernike expansion, which causes a shift of the focus in the sample plane. This procedure avoids any mechanical sample movements and, hence, potential drifts during the measurement. Example PSFs of a focus corresponding to an extreme value of α_n (with $n = 5$) both on and off a single nanoparticle are shown in Figures 5.3c and 5.3d, respectively. The corresponding measured reflection values as a function of α_5 are shown in Figure 5.3e as black data points, from which a clear minimum in reflection can be observed. Fitting the data with a Gaussian function, depicted by the red solid line in Figure 5.3e allows us to identify the optimum expansion coefficient α_n, after which the next Zernike polynomial is added to the total pattern on the SLM. This process is repeated for 20 Zernike polynomials (excluding Z_0, which corresponds to an arbitrary phase offset) according to the sequence depiced in Figure 5.3a. At the end of this process, we restart the optimization at Z_1, repeating this cycle of optimization 5 times to ensure convergence. The minimum reflectance value for all iterations is shown in Figure 5.3f, clearly showcasing a convergent behavior. It can be seen that an additional 8% in extinction is achieved through illumination with an optimized wavefront with respect to an unmodulated wavefront, reaching nearly 70% extinction by a single nanoparticle. The resulting optimum wavefront that is projected onto the SLM after completing the optimization routine is shown in Figure 5.3g. It is important to note that small alignment

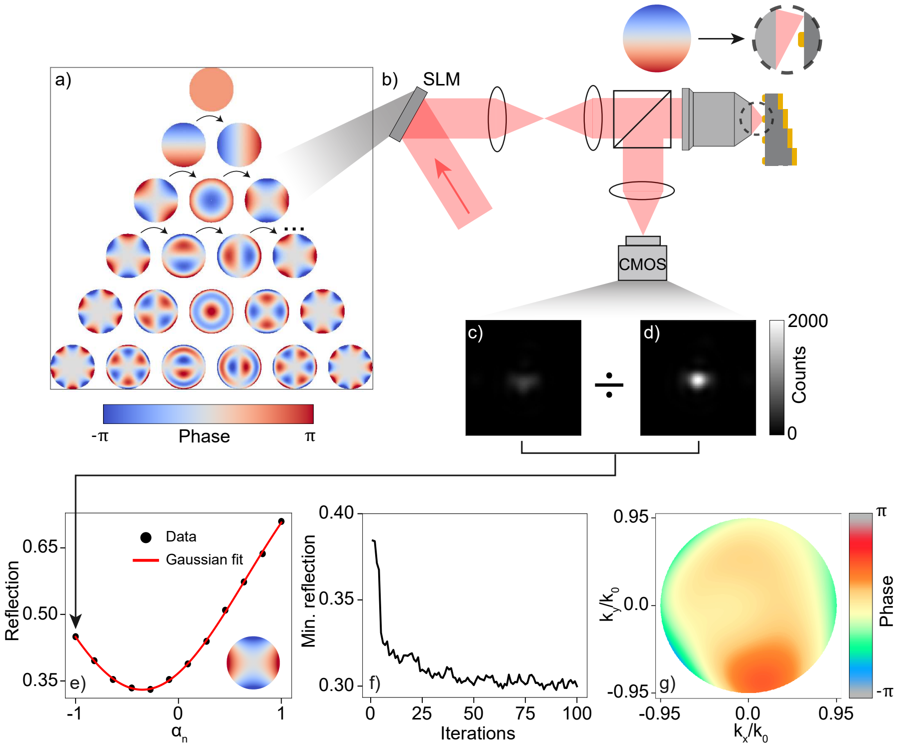

Figure 5.3: Experimental wavefront optimization routine for an individual scatterer. (A) Individual phase contributions described by Zernike polynomials that are linearly superimposed and projected by a spatial light modulator. The procedure to optimize coefficients to obtain optimum extinction is described in the main text. (B) The phase patterns are relay imaged onto the back-focal-plane of the microscope objective, which is focusing the incident wavefronts onto single nanoparticles. An additional phase-ramp pattern applied on the SLM shifts the focus either on or off a single nanoparticle. The back-reflected point spread function is captured on a CMOS detector, with typical point spread functions both on and off the single nanoparticle shown in panels (C) and (D), respectively. From these points spread functions, a single particle reflection value can be determined, and plotted versus weighting coefficient α_n of the relevant Zernike polynomial in panel (E). Here, the black dots denote measured data and the red line a Gaussian fit. (F) Minimum reflection values as a function of all iterations in the optimization. (G) Resulting wavefront after applying the optimization procedure. All data shown in this figure are measured on a single nanoparticle separated from the mirror by 391 nm.

imperfections cause additional minute aberrations in the excitation path of the setup. An unmodulated phase pattern (flat phase) projected onto the SLM therefore does not correspond to an actual flat phase profile in the BFP of the microscope objective. The optimization routine thus optimizes for both the matching of scattered wavefronts from a single nanoparticle-on-mirror, and for the removal of these extra aberrations in the setup. The optimal wavefront shown in Figure 5.3g shows the combination of these two effects, which explains the asymmetric features present in the wavefront.

We next analyze the convergent behavior of the optimization procedure as a function of spacer height between nanoscatterers and the back reflector. To this end, we apply the same protocol to 2x2 clusters of nanoparticles separated from the mirror by 204 nm, 306 nm, 390 nm, 530 nm, and 641 nm, and plot the convergence results in Figure 5.4. We observe that convergence is reached for all spacer heights, resulting in substantial increases in the total extinction after wavefront shaping for all cases, as depicted in Figure 5.4f. An extinction gain as high as 12% can be reached for a spacer height of 390 nm as shown in Figure 5.4c. In this particular case, a sub-wavelength cluster of 2x2 nanoparticles is able to cause $> 90\%$ extinction of focused light. We further observe differences in the shape of the optimization curves for different spacer heights. This indicates that different values for the optimum expansion coefficients α_n were retrieved as a function of spacer height, and thus, that the optimum wave-

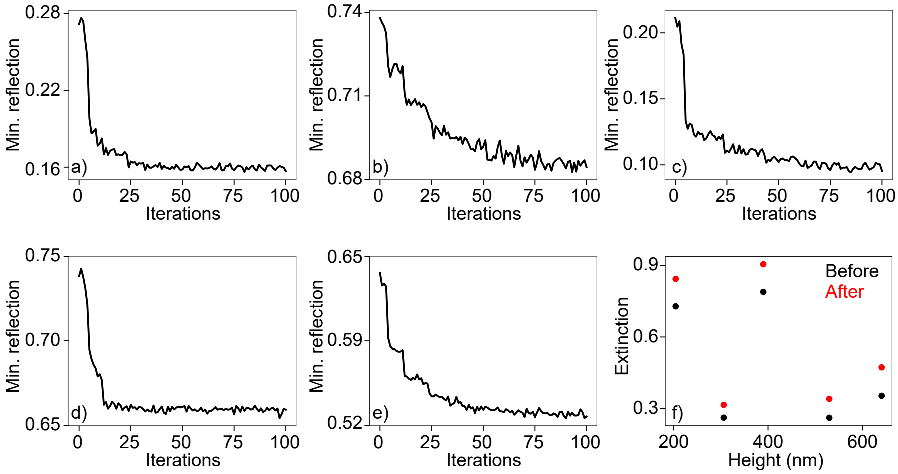

Figure 5.4: Convergence versus spacer height for a 2x2 particle array. Convergence graphs showing reflection values versus all iterations in the optimization for a 2x2 array of nanoparticles separated from the back reflector by (A) 204nm; (B) 306nm; (C) 390nm; (D) 530nm; and (E) 641nm. (F) Extinction values before (black dots) and after (red dots) applying the wavefront optimization procedure.

fronts are spacer height dependent. In the next section, we elaborate more on the connection between spacer height and retrieved optimum wavefronts.

5.4 Time reversal of scattered wavefronts

We now more closely analyze the resulting optimized wavefronts as extracted from the optimization workflow described in the previous section, and qualitatively argue that the resulting incident wavefronts are correlated to time-reversed scattered wavefronts from a nanoparticle-on-mirror system. To gain insights into the scattering behavior of a nanoparticle on mirror, we perform analytical calculations in which we model the nanoparticles as dipolar scatterers in a layered system using the Green function of the stratified system [140] and corresponding modeling parameters as discussed in Appendix B. For this, we utilize the python package "PyRAMIDS", which will shortly become open source through a separate publication. Specifically, we calculate the scattered intensity and phase from a single dipole separated by a varying distance from a gold back reflector, and plot the resulting polar emission patterns in Figure 5.5. Here, we choose spacer height values in agreement with the spacer heights chosen in the optimization measurements of Figure 5.4, namely: 204 nm, 306 nm, 390 nm, 530 nm, and 641 nm, and visualize both scattered intensity and phase as black and red curves, respectively. From this figure, we can observe strong variations in dipolar emission as a function of spacer height. The variation in scattered intensity is the fundamental reason why only a small range of spacer heights causes optimal extinction, as observed in Figure 5.2h. For these optimal heights, a nanoscatterer can most efficiently scatter light into a high-NA angular far-field spectrum, as shown, for instance, in the emission pattern of Figure 5.5c, which can therefore efficiently interfere with a high-NA focused illumination, causing optimal extinction. The variation in scattered phase indicates that a different optimal incident wavefront is required for each spacer height to cause optimal extinction, which we already hinted at in the previous section. It is this height-dependent variation in optimum wavefront which we will set out to verify by inspecting the optimum

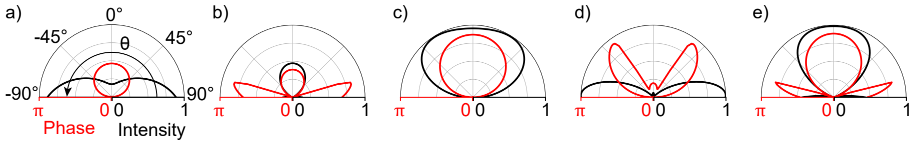

Figure 5.5: Theoretical emission patterns from a dipole on mirror. Scattered intensity and phase of a dipolar scatterer on a mirror are indicated as black and red solid curves respectively. The spacer height is varied in each panel as (A) 204 nm; (B) 306 nm; (C) 390 nm; (D) 530 nm and (E) 641 nm.

wavefronts retrieved from the optimization measurements of Figure 5.4.

To decouple the effects of aberrations in the setup from the relevant spacer height-dependent variations in scattered wavefronts, we inspect differences in optimum wavefronts relative to a reference wavefront optimized for a constant spacer height. We show differential optimized wavefronts in Figures 5.6a - 5.6d for spacer heights of 306 nm, 390 nm, 530 nm, and 641 nm, respectively, all referenced to the optimum wavefront for the spacer height of 204 nm. We further subtract an arbitrary phase offset from all differential wavefront patterns, such that the center of Fourier space corresponds to a differential phase of 0 radians. The resulting relative phase profiles show a higher degree of symmetry than the raw optimized wavefronts, indicating that the effect of static aberrations is indeed removed after referencing. We attribute the remaining minute asymmetries to a slight tilt of the sample with respect to the objective. Striking differences are again observed for the optimized wavefronts as a function of spacer height. We note especially that the differential wavefronts shown in Figures 5.6a and 5.6d show interesting features, where a rapid relative phase variation shows up at high excitation angles. To draw a qualitative comparison between the expected dipolar scattered wavefronts, we show theoretical far-field scattering calculations of relative phase profiles in Fourier space from a dipole-on-mirror system in Figures 5.6e-5.6h, using again the exact same height parameters as were chosen in the experiment. We observe qualitative similarities between the theoretical scattered differential wavefronts and the experimental optimized differential wavefronts. To draw a closer comparison, we plot line cuts of the Fourier space images through the $k_y/k_0 = 0$ axis in Figures 5.6i-5.6h, and show experimental and theoretical relative wavefronts as black and red curves respectively. Note that the curvatures of all relative optimized wavefronts qualitatively agrees with the theoretical scattered relative phase profiles.

Quantitative discrepancies between theoretical and optimized wavefronts remain, which we attribute to the following main causes. First of all, possible steep wavefront gradients in the optimum wavefront, which are described by the higher-order Zernike polynomials, are only reconstructed approximately due to the finite number of lower-order Zernike polynomials present in our optimization basis. This effect is clearly observed in Figures 5.6i and 5.6l: the theoretical relative scattered wavefronts contain steep wavefront gradients, which the experimentally optimized wavefront approximates with smooth gradients. Second, ideal time reversal of scattered wavefronts is only achieved with full vectorial complex amplitude and phase modulation capabilities. Here, we work in just one fixed polarization channel with phase-only shaping, which essentially does not take amplitude and polarization degrees if freedom in the scattered waves into account. Regions in Fourier space in which a dipole cannot efficiently radiate intensity can therefore introduce inaccuracies in the optimization result.

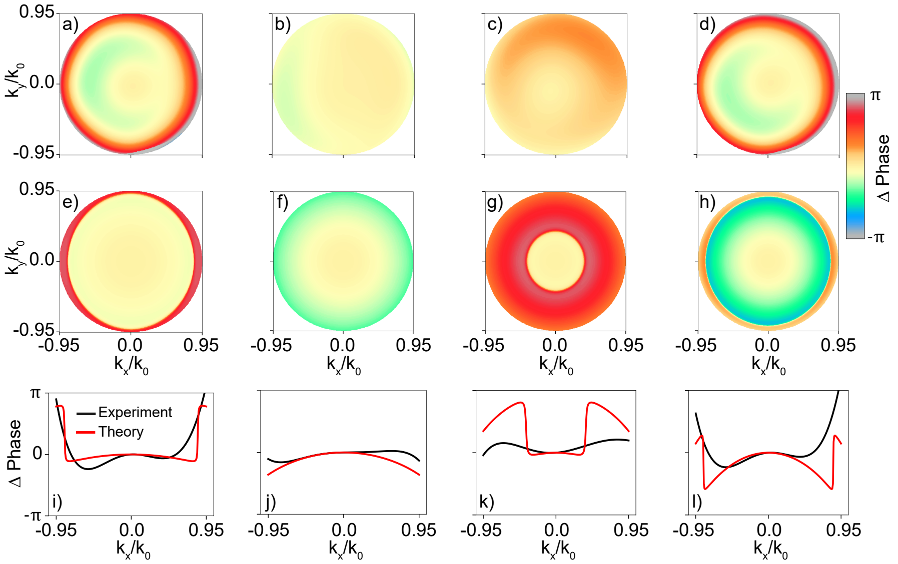

Figure 5.6: Differential phase profiles versus spacer height (A)-(D) Differential phase profiles extracted from the experimental optimization procedure, where the optimum phase profile at a spacer height of 204 nm is subtracted from the optimum phase profile at a spacer height of (A) 306 nm, (B) 390 nm, (C) 530 nm, and (D) 641 nm. All wavefronts are optimized for a cluster of 2x2 particles. (E)-(H) Theoretical differential phase patterns of the scattered wavefront of a dipole on a mirror. The same height conditions as in panels (A)-(D) are used. (I)-(L) linecuts of panels (A)-(H) through the $k_y/k_0 = 0$ axis, where the black and red curves denote experimentally optimized wavefronts and theoretical differential wavefronts, respectively. An arbitrary phase offset is subtracted from all differential phase profiles, such that the center in Fourier space corresponds to a differential phase of 0 radians.

5.5 Angle resolved extinction

From time reversal arguments, it is expected that extinction can only happen in those regions of Fourier space in which a dipole can actually emit with non-vanishing intensity, and a strong correlation between angle-resolved extinction and dipole-scattering intensity is anticipated. We therefore investigate how the spacer-height-dependent extinction is distributed in Fourier space, and compare the result to theoretically calculated scattered dipole intensities. To this end, we focus an optimum wavefront onto a cluster of 2x2 nanoparticles and measure the resulting angle-resolved reflected signal $I_{\text{cluster}}(\hat{k})$ by using Fourier microscopy (see Appendix D for details of the full experimental setup). By recording a reference angle-resolved reflected signal in the absence of the nanoparticles $I_{\text{ref}}(\hat{\mathbf{k}})$ (essentially the reflected signal from the back mirror only), we can derive an angle-resolved extinction pattern $E(\hat{\mathbf{k}})$

by $E(\hat{\mathbf{k}}) = 1 - \frac{I_{\text{cluster}}(\hat{\mathbf{k}})}{I_{\text{ref}}(\hat{\mathbf{k}})}$, which provides insight into the angular regions in Fourier space for which a nanoscatterer causes efficient extinction. We show such experimental angle-resolved extinction patterns in Figures 5.7a-5.7e for the same selection of spacer heights as mentioned in the previous section. From these images, primarily regions of positive extinction can be discerned, sometimes approaching unity as is the case in Figures 5.7a and 5.7c, which correspond to regions in Fourier space in which the nanoscatterers can fully extinguish incident radiation. A strong angle-dependent extinction efficiency is observed, which varies as a function of spacer height. We compare these angle-dependent extinction efficiencies to the calculated dipolar-scattering intensities for the exact same heights, as shown in Figures 5.7f-5.7j, and observe a strong correlation between experiment and theory. This finding corroborates that the extinction of focused light is due to destructive interference of incident waves with the scattered waves of the nanoparticles, thereby providing additional evidence that the incident waves are indeed time-reversed in those regions in which a dipole is allowed to radiate. The fact that regions of non-unity extinction occur is due to the mismatch in amplitude between incident light and the dipole radiation pattern, which can be resolved only by amplitude shaping. Consequently, further amplitude shaping of the incident waves can be beneficial to reach even higher total extinction efficiencies for those spacer heights that show strong angle-dependent extinction.

There are regions in Fourier space where an apparent negative extinction shows up, as we can observe, for instance, in Figures 5.7b and 5.7e. Negative angular extinction relates to specific regions in Fourier space in which relatively *more* light is reflected from a nanoparticle-on-mirror system than from

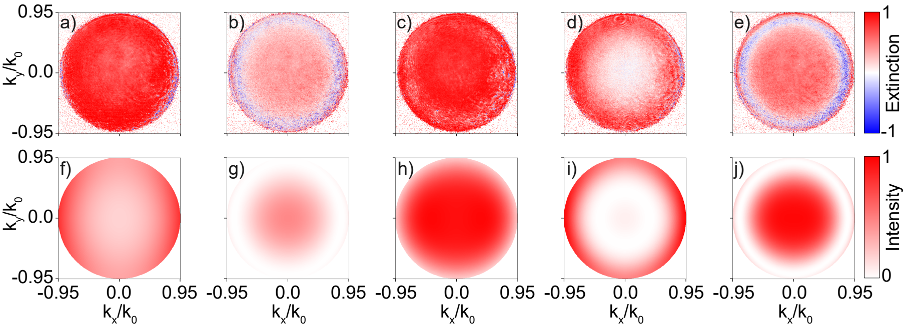

Figure 5.7: Angle resolved extinction correlates to scattered dipole intensity. (A)-(E) Experimental angle resolved extinction patterns for optimized wavefronts illuminated onto a cluster of 2x2 nanoparticles separated by a (A) 204 nm, (B) 306 nm, (C) 390 nm, (D) 530 nm and (E) 641 nm spacer layer from the back reflector. (F)-(J) Theoretical angle resolved scattered intensity patterns of a dipole on mirror, separated by the same spacer heigths as used in panels (A)-(E).

the mirror only. This can happen in regions of the incident wavefront that are out of phase with respect to the time-reversed scattered wave of the nanoparticle, effectively leading to *constructive* interference between the scattering of the nanoparticle and the incident wave. This is, for instance, the case for the differential optimum wavefronts in Figures 5.6i and 5.6l. We further observe that, due to the wavefront discrepancies caused by the smooth Zernike polynomial approximation of the actually abrupt phase changes in the dipole radiation pattern, there are indeed small angular regions in which the relative optimum wavefront is slightly out of phase relative to the calculated scattered phase. These are exactly the regions that correspond to the negative extinction values of Figures 5.7b and 5.7e.

The central notion underlying Figure 7 is that extinction of a small object with a focused beam can be interpreted as the angle-resolved destructive interference of the reflected incident wavefront and the scattering pattern of the object. Interestingly, this also means that one can control by wavefront shaping at will in which regions extinction occurs in the back focal plane. To demonstrate this idea, we add a set of binary $0 - \pi$ phase patterns to the wavefront optimized for a 2x2 cluster of nanoparticles separated from the mirror by the optimum height of 391 nm. Since extinction is connected to the interference between the scattered field and the back-reflected incident light, one expects that, in regions where the incident phase front is toggled to be out of phase with respect to the ideal time-reversed phase front, *constructive* interference with the scattered wave occurs (i.e., *negative* extinction). The projected additional phase patterns are depicted in Figures 5.8a-c, which result in the corresponding angle-resolved extinction patterns shown in Figures 5.8d-f. We observe that negative extinction is indeed seen in those regions in which the incident wavefront is out of phase with the optimum time-reversed scattered wavefront. Effectively, incident light originating from positive extinction regions is redirected into the locally negative extinction regions. In this way, angular extinction in Fourier space can be engineered by projecting additional designer patterns. In the particular case of Figure 5.8f, we observe that the angle-resolved extinction is drastically reduced when a $0-\pi$ symmetric phase step is added to the optimum wavefront. Expressed in wave vector space, this particular incident wavefront is symmetry-mismatched from the dipole mode of the particle. Expressed in real-space terms, the incident wavefront focuses to a double-lobed PSF with vanishing intensity at the center, akin to a Hermite-Gaussian beam profile, which can only interact with much weaker quadrupole terms in the particle polarizability. As the main dipolar particle resonance is not excited at all, this means that there is hardly any extinction (i.e., neither positive nor negative extinction). This observation highlights the crucial aspect of efficient generation of a scattered wave from the nanoparticle, without which no interference, and therefore no extinction, can happen. Of course, the total angle-integrated extinction cannot be lower than zero, and regions of positive and negative extinction must therefore be properly balanced.

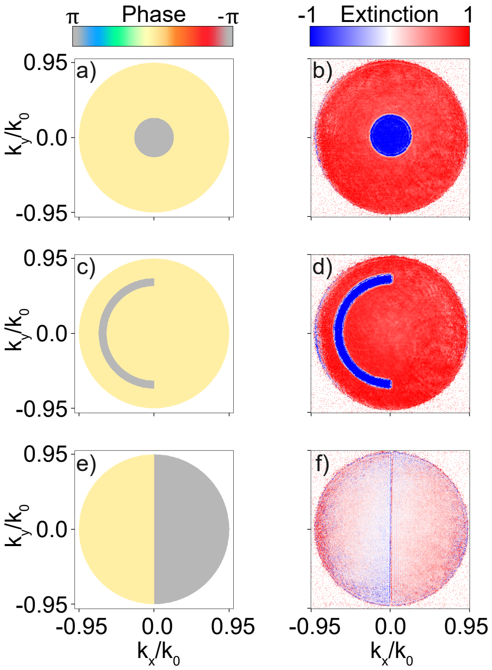

Figure 5.8: Extinction engineering in Fourier space Panels (A), (C), and (E) denote additional phase patterns projected on top of the optimum wavefront, and panels (B), (D), and (F) show angle-resolved extinction patterns for a 2x2 cluster of nanoparticles corresponding to these projected phase patterns. The nanoparticles are separated from the back reflector by a distance of 390 nm.

5.6 Conclusions

In summary, we study optimal extinction scenarios in finite-sized particle arrays and single nanoparticle based Salisbury-screen systems. We experimentally investigate how the angular spectrum of a tightly focused beam can be engineered for optimum extinction in single nanoparticle-on-mirror systems, and qualitatively argue that the optimum incident illumination conditions are matched to the time-reversed radiation pattern of the nanoparticles. Using these tailored illumination schemes, we demonstrate that a single plasmonic nanoparticle can attenuate 70% of a focused light beam, while a cluster of 2x2 particles can cause up to 90% extinction.

Looking ahead, higher extinction contrasts could be realized through tighter focusing using immersion optics. Additionally, incorporating amplitude and polarization [59] structuring capabilities in our wavefront shaping setup could further enhance mode matching with the scatterer's radiation pattern. On the side of the scatterer, higher extinction cross section could be engineered by mixing multipole contributions in low-loss dielectric particles supporting Mie resonances [15, 135, 189]. Besides reaching optimum extinction, the developed framework could also be exploited to *probe* multipole resonances in scattering objects by analyzing the optimum wavefront and corresponding angle-resolved extinction. This can be potentially interesting in, for instance, Fano-resonant systems [132, 201], where precise identification of dominant modes is critical. Additionally, the investigated platform could be exploited as a highly responsive optical sensor, where one could investigate how perturbations on the nanoscale [116] influence optimum extinction conditions. Finally, an interesting continuation to this work would be to probe the specific channels into which the extinguished light is transduced (i.e., absorption at the particles, launching of propagating surface modes, and direct inelastic absorption at the surface). Recent works have predicted that nanoparticles positioned above a substrate can produce efficient coupling of focused light into propagating polaritons in the substrate [196, 202, 203]. We therefore expect that, in our experiment, the incident focused light is mainly transduced into surface-plasmon polaritons in the gold back mirror. Experimentally, such surface modes could be visualized by, for instance, electron beams [204], or scanning near-field probes [205]. Altogether, our work highlights the potential of tailored wavefront engineering to maximize optical extinction at the nanoscale, paving the way for ultracompact light control.

Appendices

A Sample fabrication

We fabricate the nanoscatterers-on-mirror samples by electron beam (e-beam) lithography using the following procedure. A 170 μm-thick glass substrate (Menzel-Gläser) is sonicated for 10 min in H_2O and cleaned in a solution of base piranha (NH_4OH:H_2H_2:H_2O = 1:1:5) at 75°C for 15 min. After thoroughly rinsing excess piranha with H_2O, the sample is blown dry with N_2. For high-resolution patterning of nanostructures, we utilize a multistack thin film recipe consisting of a thick polymethyl methacrylate (PMMA) bottom layer, followed by a thin Ge layer, which is finally covered by a thin e-beam resist (CSAR AR-P 6200:09) as top layer. Here, the thin e-beam resist allows for high resolution e-beam writing, the Ge layer serves as a sacrificial mask through which the patterns can be etched, and the thick PMMA layer generates sufficient undercut for lift-off. We start by spin-coating a solution of (PMMA:Anisole = 3:2) at 3000 rpm for 45 s, followed by baking the sample at 180°C for 2 mins, resulting in a 150 nm layer of PMMA, after which a 20 nm Ge mask is deposited by thermal evaporation (Polyteknik Flextura M508 E) at a rate of 0.05nm/s. A solution of e-beam resist (CZAR:Anisole = 3:2) is then spin-coated at 4000 rpm for 60 s and baked at 150°C for 2 mins, resulting in a 60 nm resist layer. Then, 50 nm gold nanoparticles are drop-casted in the corners of the substrate for e-beam alignment purposes. E-beam exposure (Raith) is done at an acceleration voltage of 50 kV, a beam current of 0.123 nA, and a nominal dose of 130 μC/cm^2. After exposure, the sample is developed in consecutive solutions of 1) Amyl-Acetate for 60 s, 2) O-xylene for 6 s, 3) Methyl-isobutyl-ketone/2-propanol (MIBK:IPA = 9:1) for 15 s, 4) 2-propanol (IPA) for 30 s, and finally blown dry with N_2. We then plasma etch (Oxford Plasmalab 80+) the pattern through the Ge mask using a gas mixture of O_2:SF_6 = 1:5 for 60 s at a forward power of 30 W, and the PMMA layer using O_2 plasma for 100 s at forward power of 50 W. After etching, we deposit a 40 nm gold film using e-beam evaporation (Polyteknik Flextura M508 E) at a rate of 0.05 nm/s. Excess PMMA, Ge and gold are removed by a lift off process by placing the sample in Acetone at 50 °C for 3 hours and gentle flushing afterwards. To obtain a variable spacer height, we deposit SiO_2 at a rate of 0.1 nm/s using e-beam evaporation (Polyteknik Flextura M508 E). A linear shutter that is partly covering the sample can be controlled to obtain a staircase-like thin film that is increasing in thickness with steps of roughly 10 nm, with a lateral step size of 500 μm. Finally, a 50 nm gold back reflector is deposited by e-beam evaporation at a rate of 0.05 nm/s.

B Theoretical calculations

Nanoscatterer-on-mirror emission patterns are calculated using the Green function formalism. In brief, we model the scatterers as electric dipole sources $\mathbf{p}$ positioned at $\mathbf{r}_0$ above a back reflector. For such systems, the total Green function $\overleftrightarrow{\mathbf{G}}(\mathbf{r}_0, \mathbf{r}_1)$ can be separated into free-space and reflected contributions [140], after which the scattered electric fields $\mathbf{E}$ can be determined in the reflected far-field half-space at position $\mathbf{r}_1$ as

$$\mathbf{E}(\mathbf{r}_1, \mathbf{r}_0) = \omega^2 \mu_0 \overleftrightarrow{\mathbf{G}}(\mathbf{r}_0, \mathbf{r}_1) \cdot \mathbf{p}, \tag{5.3}$$

where ω is the driving frequency and μ_0 the free-space permeability. We construct the layered medium in the calculations to precisely mimick the experimental conditions. The consecutive layers are: 1) a semi-infinite half-space of vacuum with a refractive index $n_{\mathrm{vac}} = 1$, 2) a 50 nm gold back reflector with refractive index taken from Ref. [206], and 3) a semi-infinite layer of SiO_2 with $n_{\mathrm{SiO_2}} = 1.42$. The dipole scatterer is positioned above the back reflector according to the experimental parameters.

C Spacer height determination

To accurately determine the retrieved spacer heights between the nanoparticles and the back reflector, we patterned gold mirrors in the same plane as the nanoparticles at every spacer step. In this way, we obtain mirror-on-mirror regions on the sample separated by variable spacer heights, which act as Fabry-Perot resonators. We can retrieve the unknown spacer heights by measuring the resonance wavelengths of all these resonators, and compare the results to the resonant wavelength extracted from a transfer-matrix model, which describes the mirror-spacer-mirror regions with an a priori known spacer height.

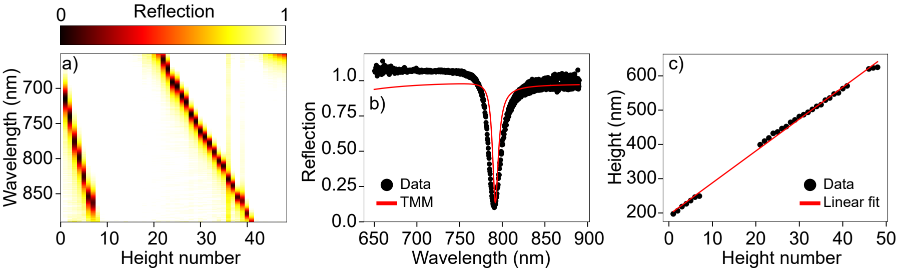

Figure 5.9: Spacer height determination using Fabry-Perot resonances. (A) Reflection spectra for mirror-on-mirror samples separated by a variable height that is to be determined. (B) Single mirror-on-mirror reflection spectrum for height number 32 in panel (A) (black datapoints). A reflection spectrum calculated by a transfer-matrix model for a spacer height of 504 nm is shown for comparison (red curve). (C) Extracted spacer heights versus height number.

Figure 5.9a shows reflection spectra from mirror-on-mirror samples for all relevant spacer heights. A resonant dip in reflection can be observed, which redshifts for increasing spacer heights, indicating the increasing separation between the mirrors. Figure 5.9b shows an example of a single reflection spectrum at height number 32 from Figure 5.9a, from which a resonance wavelength can be determined. In the same panel, the calculated reflection spectrum from the transfer-matrix model is described by a red line, assuming a spacer height of 504nm. In this way, a spacer height can be determined for every height number, and the final result is shown in Figure 5.9c. Regions where no resonance wavelength could be measured due to the limited spectral range of the spectrometer are interpolated by fitting a straight line through all data points, showing excellent overlap.

D Experimental setup

The experimental setup that was used to conduct the experiments described in the main text is schematically depicted in Figure 5.10, alongside all labeled optical components. A fiber-coupled supercontinuum source (NKT whitelase Micro) was collimated and polarized. For the spectroscopic measurements shown in Figure 2 of the main text, the broadband output was focused on the sample by a high-NA (0.95) microscope objective, while an iris positioned in the conjugate back-focal plane on the excitation side controlled the effective NA of the focus. The reflected signal from the sample was captured through the same objective and focused onto the slit of a spectrometer (Andor Shamrock 303i), after which a spectrum was recorded by a cooled CCD (Andor iVac). The spectra used in the main text were acquired by summing 100 frames at 10 ms integration time. For the wavefront shaping measurements, we filtered the input light with a 760 nm bandpass filter (10nm FWHM) and guided the beam towards a liquid-crystal SLM (Meadowlark P1920-600-1300-HDMI) via two flip mirrors. The plane of the SLM was relay-imaged onto the back-focal plane of the objective, allowing for phase-only modulation of incident wave vectors. The back-reflected signal was then imaged onto a C-MOS camera (Basler, acA1920–40um) and acquired in either Fourier-space or real-space imaging mode. Switching between these modes was achieved by adding/removing lens L8 in/from the setup, respectively. During the optimization, point spread functions in real space were acquired at an integration time of 3 ms. Reflected Fourier space images, from which angle-resolved extinction patterns were constructed, were captured at 50 ms exposure time. Sample movement was controlled by motorized actuators (Thorlabs Z812) equipped with K-Cube stepper controllers (KST101). A 3D nanopositioning piezo (PI Nanocube) was used for fine alignment.

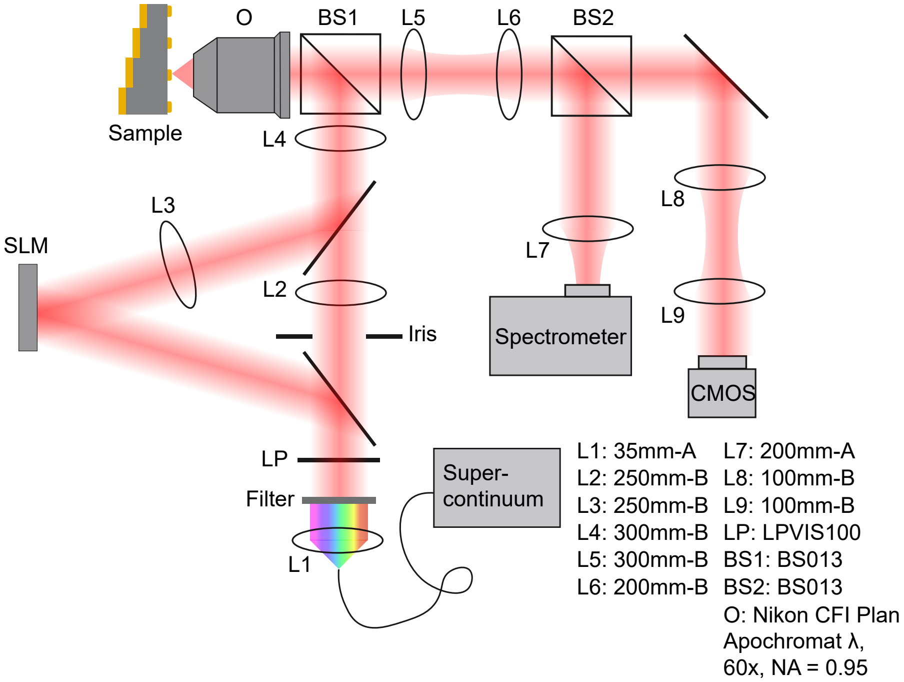

Figure 5.10: Sketch of the complete experimental setup as used in the experiments from the main text. All lenses are achromatic (AC-254), and the indicated codes list the focal length in millimeters, followed by an A or B for the antireflection coating (Thorlabs nomenclature).

References

[1] M. Castells, *The Information Age: Economy, Society and Culture (3 volumes)*, Blackwell, Oxford **1997**, 1998 (1996).

[2] G. Keiser, *Optical Fiber Communications*, vol. 2 (McGraw-Hill New York, 2000).

[3] P. Dong, Y.-K. Chen, G.-H. Duan, and D. T. Neilson, *Silicon Photonic Devices and Integrated Circuits*, Nanophotonics **3**, 215 (2014).

[4] P. L. McMahon, *The Physics of Optical Computing*, Nat. Rev. Phys. **5**, 717 (2023).

[5] D. E. Chang, A. S. Sørensen, E. A. Demler, and M. D. Lukin, *A Single-Photon Transistor using Nanoscale Surface Plasmons*, Nat. Phys. **3**, 807 (2007).

[6] J. R. Lakowicz, *Principles of Fluorescence Spectroscopy* (Springer, 2006).

[7] E. Smith, and G. Dent, *Modern Raman Spectroscopy: a Practical Approach* (John Wiley & Sons, 2019).

[8] B. P. Abbott, R. Abbott, T. Abbott, M. Abernathy, F. Acernese, K. Ackley, C. Adams, T. Adams, P. Addesso, R. X. Adhikari, et al., *Observation of Gravitational Waves from a Binary Black Hole Merger*, Phys. Rev. Lett. **116**, 061102, 1 (2016).

[9] G. E. Moore, *Cramming more Components onto Integrated Circuits*, Proceedings of the IEEE **86**, 82 (1998).

[10] A. J. den Boef, *Optical Wafer Metrology Sensors for Process-Robust CD and Overlay Control in Semiconductor Device Manufacturing*, Surf. Topogr.: Metrol. Prop. **4**, 023001, 1 (2016).

[11] S. M. Kay, *Fundamentals of Statistical Signal Processing: Estimation Theory* (Prentice-Hall, Inc., 1993).

[12] W. X. Lim, and R. Singh, *Universal Behaviour of High-Q Fano Resonances in Metamaterials: Terahertz to Near-Infrared Regime*, Nano Convergence **5**, 5 (2018).

[13] A. F. Koenderink, A. Alù, and A. Polman, *Nanophotonics: Shrinking Light-Based Technology*, Science **348**, 516 (2015).

[14] L. Novotny, and N. Van Hulst, *Antennas for Light*, Nat. Photonics **5**, 83 (2011).

[15] A. I. Kuznetsov, A. E. Miroshnichenko, M. L. Brongersma, Y. S. Kivshar, and B. Luk'yanchuk, *Optically Resonant Dielectric Nanostructures*, Science **354**, aag2472 (2016).

[16] N. I. Zheludev, and Y. S. Kivshar, *From Metamaterials to Metadevices*, Nat. Mater. **11**, 917 (2012).

[17] N. Yu, and F. Capasso, *Flat Optics with Designer Metasurfaces*, Nat. Mater. **13**, 139 (2014).

[18] A. I. Kuznetsov, M. L. Brongersma, J. Yao, M. K. Chen, U. Levy, D. P. Tsai, N. I. Zheludev, A. Faraon, A. Arbabi, N. Yu, et al., *Roadmap for Optical Metasurfaces*, ACS Photonics **11**, 816 (2024).

[19] W. T. Chen, A. Y. Zhu, V. Sanjeev, M. Khorasaninejad, Z. Shi, E. Lee, and F. Capasso, *A Broadband Achromatic Metalens for Focusing and Imaging in the Visible*, Nat. Nanotechnol. **13**, 220 (2018).

[20] J. Balthasar Mueller, N. A. Rubin, R. C. Devlin, B. Groever, and F. Capasso, *Metasurface Polarization Optics: Independent Phase Control of Arbitrary Orthogonal States of Polarization*, Phys. Rev. Lett. **118**, 113901 (2017).

[21] G. Zheng, H. Mühlenbernd, M. Kenney, G. Li, T. Zentgraf, and S. Zhang, *Metasurface Holograms Reaching 80% Efficiency*, Nat. Nanotechnol. **10**, 308 (2015).

[22] L. Huang, S. Zhang, and T. Zentgraf, *Metasurface Holography: from Fundamentals to Applications*, Nanophotonics **7**, 1169 (2018).

[23] G. M. Akselrod, J. Huang, T. B. Hoang, P. T. Bowen, L. Su, D. R. Smith, and M. H. Mikkelsen, *Large-Area Metasurface Perfect Absorbers from Visible to Near-Infrared*, Adv. Mater. **27**, 8028 (2015).

[24] A. Cordaro, H. Kwon, D. Sounas, A. F. Koenderink, A. Alù, and A. Polman, *High-Index Dielectric Metasurfaces Performing Mathematical Operations*, Nano Lett. **19**, 8418 (2019).

[25] A. Cordaro, B. Edwards, V. Nikkhah, A. Alù, N. Engheta, and A. Polman, *Solving Integral Equations in Free Space with Inverse-Designed Ultrathin Optical Metagratings*, Nat. Nanotechnol. **18**, 365 (2023).

[26] M. F. Limonov, M. V. Rybin, A. N. Poddubny, and Y. S. Kivshar, *Fano Resonances in Photonics*, Nat. Photonics **11**, 543 (2017).

[27] K. Koshelev, Y. Tang, K. Li, D.-Y. Choi, G. Li, and Y. Kivshar, *Nonlinear Metasurfaces Governed by Bound States in the Continuum*, ACS Photonics **6**, 1639 (2019).

[28] Z. Liu, Y. Xu, Y. Lin, J. Xiang, T. Feng, Q. Cao, J. Li, S. Lan, and J. Liu, *High-Q Quasibound States in the Continuum for Nonlinear Metasurfaces*, Phys. Rev. Lett. **123**, 253901 (2019).

[29] R. Singh, W. Cao, I. Al-Naib, L. Cong, W. Withayachumnankul, and W. Zhang, *Ultrasensitive Terahertz Sensing with High-Q Fano Resonances in Metasurfaces*, Appl. Phys. Lett. **105** (2014).

[30] K. Koshelev, S. Lepeshov, M. Liu, A. Bogdanov, and Y. Kivshar, *Asymmetric Metasurfaces with High-Q Resonances Governed by Bound States in the Continuum*, Phys. Rev. Lett. **121**, 193903, 1 (2018).

[31] C. W. Hsu, B. Zhen, A. D. Stone, J. D. Joannopoulos, and M. Soljačić, *Bound States in the Continuum*, Nat. Rev. Mater. **1**, 1 (2016).

[32] F. Yesilkoy, E. R. Arvelo, Y. Jahani, M. Liu, A. Tittl, V. Cevher, Y. Kivshar, and H. Altug, *Ultrasensitive Hyperspectral Imaging and Biodetection enabled by Dielectric Metasurfaces*, Nat. Photonics **13**, 390 (2019).

[33] A. Tittl, A. Leitis, M. Liu, F. Yesilkoy, D.-Y. Choi, D. N. Neshev, Y. S. Kivshar, and H. Altug, *Imaging-Based Molecular Barcoding with Pixelated Dielectric Metasurfaces*, Science **360**, 1105 (2018).

[34] E. Abbe, *Beiträge zur Theorie des Mikroskops und der Mikroskopischen Wahrnehmung*, Archiv für mikroskopische Anatomie **9**, 413 (1873).

[35] M. Hu, C. Novo, A. Funston, H. Wang, H. Staleva, S. Zou, P. Mulvaney, Y. Xia, and G. V. Hartland, *Dark-Field Microscopy Studies of Single Metal Nanoparticles: Understanding the Factors that Influence the Linewidth of the Localized Surface Plasmon Resonance*, J. Mater. Chem. **18**, 1949 (2008).

[36] G. G. Stokes, *On the Composition and Resolution of Streams of Polarized Light from Different Sources*, Trans. Cambridge Philos. Soc. **9**, 399 (1851).

[37] H. Poincaré, *Théorie Mathématique de la Lumière II.: Nouvelles études sur la Diffraction.–Théorie de la Dispersion de Helmholtz. Leçons professées pendant le premier semestre 1891-1892*, vol. 1 (G. Carré, 1889).

[38] R. C. Jones, *A New Calculus for the Treatment of Optical Systems. Description and Discussion of the Calculus*, J. Opt. Soc. Am. **31**, 488 (1941).

[39] R. Chipman, W. S. T. Lam, and G. Young, *Polarized Light and Optical Systems* (CRC press, 2018).

[40] C. I. Osorio, A. Mohtashami, and A. F. Koenderink, *K-space Polarimetry of Bullseye Plasmon Antennas*, Sci. Rep. **5**, 1 (2015).

[41] Z. Karny, S. Lavi, and O. Kafri, *Direct Determination of the Number of Transverse Modes of a Light Beam*, Opt. Lett. **8**, 409 (1983).

[42] A. Forbes, M. De Oliveira, and M. R. Dennis, *Structured Light*, Nat. Photonics **15**, 253 (2021).

[43] H. Rubinsztein-Dunlop, A. Forbes, M. V. Berry, M. R. Dennis, D. L. Andrews, M. Mansuripur, C. Denz, C. Alpmann, P. Banzer, T. Bauer, et al., *Roadmap on Structured Light*, J. Opt. **19**, 013001 (2016).

[44] G. Lazarev, P.-J. Chen, J. Strauss, N. Fontaine, and A. Forbes, *Beyond the Display: Phase-Only Liquid Crystal on Silicon Devices and their Applications in Photonics*, Opt. Express **27**, 16206 (2019).

[45] Y.-X. Ren, R.-D. Lu, and L. Gong, *Tailoring Light with a Digital Micromirror Device*, Annal. Phys. **527**, 447 (2015).

[46] S. Turtaev, I. T. Leite, K. J. Mitchell, M. J. Padgett, D. B. Phillips, and T. Čižmár, *Comparison of Nematic Liquid-Crystal and DMD based Spatial Light Modulation in Complex Photonics*, Opt. Express **25**, 29874 (2017).

[47] S. A. Goorden, J. Bertolotti, and A. P. Mosk, *Superpixel-Based Spatial Amplitude and Phase Modulation using a Digital Micromirror Device*, Opt. Express **22**, 17999 (2014).

[48] E. Van Putten, I. M. Vellekoop, and A. Mosk, *Spatial Amplitude and Phase Modulation using Commercial Twisted Nematic LCDs*, Appl. Opt. **47**, 2076 (2008).

[49] S. Gigan, O. Katz, H. B. De Aguiar, E. R. Andresen, A. Aubry, J. Bertolotti, E. Bossy, D. Bouchet, J. Brake, S. Brasselet, et al., *Roadmap on Wavefront Shaping and Deep Imaging in Complex Media*, J. Phys.: Photonics **4**, 042501 (2022).

[50] I. M. Vellekoop, and A. P. Mosk, *Focusing Coherent Light Through Opaque Strongly Scattering Media*, Opt. Lett. **32**, 2309 (2007).

[51] A. P. Mosk, A. Lagendijk, G. Lerosey, and M. Fink, *Controlling Waves in Space and Time for Imaging and Focusing in Complex Media*, Nat. Photonics **6**, 283 (2012).

[52] J. Bertolotti, E. G. Van Putten, C. Blum, A. Lagendijk, W. L. Vos, and A. P. Mosk, *Non-invasive Imaging Through Opaque Scattering Layers*, Nature **491**, 232 (2012).

[53] C. Ma, X. Xu, Y. Liu, and L. V. Wang, *Time-Reversed Adapted-Perturbation (TRAP) Optical Focusing onto Dynamic Objects Inside Scattering Media*, Nat. Photonics **8**, 931 (2014).

[54] J. Tang, R. N. Germain, and M. Cui, *Superpenetration Optical Microscopy by Iterative Multiphoton Adaptive Compensation Technique*, Proc. Natl. Acad. Sci. **109**, 8434 (2012).

[55] C. Moretti, and S. Gigan, *Readout of Fluorescence Functional Signals Through Highly Scattering Tissue*, Nat. Photonics **14**, 361 (2020).

[56] S. Ohayon, A. Caravaca-Aguirre, R. Piestun, and J. J. DiCarlo, *Minimally Invasive Multimode Optical Fiber Microendoscope for Deep Brain Fluorescence Imaging*, Biomed. Opt. Exp. **9**, 1492 (2018).

[57] S. Turtaev, I. T. Leite, T. Altwegg-Boussac, J. M. Pakan, N. L. Rochefort, and T. Čižmár, *High-Fidelity Multimode Fibre-Based Endoscopy for Deep Brain in Vivo Imaging*, Light Sci. Appl. **7**, 92 (2018).

[58] H. Wang, J. Hu, Y. Baek, K. Tsuchiyama, M. Joly, Q. Liu, and S. Gigan, *Optical Next Generation Reservoir Computing*, Light Sci. Appl. **14**, 245 (2025).

[59] A. Rubano, F. Cardano, B. Piccirillo, and L. Marrucci, *Q-plate Technology: A Progress Review*, J. Opt. Soc. Am. B **36**, D70 (2019).

[60] L. Allen, M. W. Beijersbergen, R. Spreeuw, and J. Woerdman, *Orbital Angular Momentum of Light and the Transformation of Laguerre-Gaussian Laser Modes*, Phys. Rev. A **45**, 8185 (1992).

[61] F. Cardano, E. Karimi, S. Slussarenko, L. Marrucci, C. de Lisio, and E. Santamato, *Polarization Pattern of Vector Vortex Beams Generated by Q-Plates With Different Topological Charges*, Appl. Opt. **51**, C1 (2012).

[62] R. Dorn, S. Quabis, and G. Leuchs, *Sharper Focus for a Radially Polarized Light Beam*, Phys. Rev. Lett. **91**, 233901 (2003).

[63] A. F. Abouraddy, and K. C. Toussaint Jr, *Three-Dimensional Polarization Control in Microscopy*, Phys. Rev. Lett. **96**, 153901 (2006).

[64] B. J. Roxworthy, and K. C. Toussaint, *Optical Trapping with π-Phase Cylindrical Vector Beams*, New J. Phys. **12**, 073012 (2010).

[65] A. Monmayrant, S. Weber, and B. Chatel, *A Newcomer's Guide to Ultrashort Pulse Shaping and Characterization*, J. Phys. B: At. Mol. Opt. Phys. **43**, 103001 (2010).

[66] A. M. Weiner, *Ultrafast Optical Pulse Shaping: A Tutorial Review*, Opt. Commun. **284**, 3669 (2011).

[67] A. Chong, C. Wan, J. Chen, and Q. Zhan, *Generation of Spatiotemporal Optical Vortices with Controllable Transverse Orbital Angular Momentum*, Nat. Photonics **14**, 350 (2020).

[68] F. G. Omenetto, A. J. Taylor, M. D. Moores, and D. H. Reitze, *Adaptive Control of Femtosecond Pulse Propagation in Optical Fibers*, Opt. Lett. **26**, 938 (2001).

[69] D. Goswami, *Optical Pulse Shaping Approaches to Coherent Control*, Phys. Rep. **374**, 385 (2003).

[70] W. Zhou, R. Apkarian, Z. L. Wang, and D. Joy, in *Scanning Microscopy for Nanotechnology: Techniques and Applications* (Springer, 2006), pp. 1–40.

[71] A. Habermas, D. Hong, M. F. Ross, and W. R. Livesay, *193-nm CD Shrinkage under SEM: Modeling the Mechanism*, in *SPIE Metrol. Inspec. and Proc. Contr. for Microlitho. XVI* (SPIE, 2002), vol. 4689, pp. 92–101.

[72] M. Adel, D. Kandel, V. Levinski, J. Seligson, and A. Kuniavsky, *Diffraction Order Control in Overlay Metrology: a Review of the Roadmap Options*, SPIE **6922**, 23 (2008).

[73] Y. Shechtman, S. J. Sahl, A. S. Backer, and W. E. Moerner, *Optimal Point Spread Function Design for 3D Imaging*, Phys. Rev. Lett. **113**, 133902 (2014).

[74] D. Bouchet, S. Rotter, and A. P. Mosk, *Maximum Information States for Coherent Scattering Measurements*, Nat. Phys. **17**, 564 (2021).

[75] A. Bag, M. Neugebauer, P. Woźniak, G. Leuchs, and P. Banzer, *Transverse Kerker Scattering for Angstrom Localization of Nanoparticles*, Phys. Rev. Lett. **121**, 193902, 1 (2018).

[76] G. H. Yuan, and N. I. Zheludev, *Detecting Nanometric Displacements with Optical Ruler Metrology*, Science **364**, 771 (2019).

[77] K. J. Gåsvik, *Optical Metrology* (John Wiley & Sons, 2003).

[78] T. Yoshizawa, *Handbook of Optical Metrology: Principles and Applications* (CRC press, 2009).

[79] S. W. Hell, and J. Wichmann, *Breaking the Diffraction Resolution Limit by Stimulated Emission: Stimulated-Emission-Depletion Fluorescence Microscopy*, Opt. Lett. **19**, 780 (1994).

[80] E. Betzig, G. H. Patterson, R. Sougrat, O. W. Lindwasser, S. Olenych, J. S. Bonifacino, M. W. Davidson, J. Lippincott-Schwartz, and H. F. Hess, *Imaging Intracellular Fluorescent Proteins at Nanometer Resolution*, Science **313**, 1642 (2006).

[81] M. J. Rust, M. Bates, and X. Zhuang, *Sub-Diffraction-Limit Imaging by Stochastic Optical Reconstruction Microscopy (STORM)*, Nat. Methods **3**, 793 (2006).

[82] K. Kong, C. Kendall, N. Stone, and I. Notingher, *Raman Spectroscopy for Medical Diagnostics—From in-Vitro Biofluid Assays to in-Vivo Cancer Detection*, Adv. Drug Deliv. Rev. **89**, 121 (2015).

[83] N. G. Orji, M. Badaroglu, B. M. Barnes, C. Beitia, B. D. Bunday, U. Celano, R. J. Kline, M. Neisser, Y. Obeng, and A. E. Vladar, *Metrology for the Next Generation of Semiconductor Devices*, Nat. Electron. **1**, 532 (2018).

[84] A. J. Den Boef, *Optical Metrology of Semiconductor Wafers in Lithography*, in *icOPEN2013* (SPIE, 2013), vol. 8769, pp. 57–65.

[85] S. W. Hell, *Far-field Optical Nanoscopy*, Science **316**, 5828, 1153 (2007).

[86] B. Huang, M. Bates, and X. Zhuang, *Super-Resolution Fluorescence Microscopy*, Annu. Rev. Biochem. **78**, 993 (2009).

[87] A. F. Koenderink, R. Tsukanov, J. Enderlein, I. Izeddin, and V. Krachmalnicoff, *Super-Resolution Imaging: when Biophysics meets Nanophotonics*, Nanophotonics **11**, 169 (2022).

[88] R. Röhrich, C. Hoekmeijer, C. I. Osorio, and A. F. Koenderink, *Quantifying Single Plasmonic Nanostructure Far-Fields with Interferometric and Polarimetric K-Space Microscopy*, Light Sci. Appl. **7**, 1 (2018).

[89] R. D. Buijs, N. J. Schilder, T. A. W. Wolterink, G. Gerini, E. Verhagen, and A. F. Koenderink, *Super-Resolution without Imaging: Library-Based Approaches using Near-to-Far-Field Transduction by a Nanophotonic Structure*, ACS Photonics **7**, 3246 (2020).

[90] M. G. L. Gustafsson, *Surpassing the Lateral Resolution Limit by a Factor of Two using Structured Illumination Microscopy*, J. Microsc. **198**, 82 (2000).

[91] H. Rubinsztein-Dunlop, A. Forbes, M. V. Berry, M. R. Dennis, D. L. Andrews, M. Mansuripur, C. Denz, C. Alpmann, P. Banzer, T. Bauer, E. Karimi, L. Marrucci, M. Padgett, M. Ritsch-Marte, N. M. Litchinitser, et al., *Roadmap on Structured Light*, J. Opt. **19**, 013001, 1 (2017).

[92] Z. Xi, L. Wei, A. J. L. Adam, H. Urbach, and L. Du, *Accurate Feeding of Nanoantenna by Singular Optics for Nanoscale Translational and Rotational Displacement Sensing*, Phys. Rev. Lett. **117**, 113903, 1 (2016).

[93] T. A. Wolterink, R. D. Buijs, G. Gerini, E. Verhagen, and A. F. Koenderink, *Calibration-Based Overlay Sensing with Minimal-Footprint Targets*, Appl. Phys. Lett. **119**, 111104 (2021).

[94] J. B. Mueller, N. A. Rubin, R. C. Devlin, B. Groever, and F. Capasso, *Metasurface Polarization Optics: Independent Phase Control of Arbitrary Orthogonal States of Polarization*, Phys. Rev. Lett. **118**, 113901, 1 (2017).

[95] A. Arbabi, Y. Horie, M. Bagheri, and A. Faraon, *Dielectric Metasurfaces for Complete Control of Phase and Polarization with Subwavelength Spatial Resolution and High Transmission*, Nat. Nanotechnol. **10**, 937 (2015).

[96] K. Abrashitova, and L. V. Amitonova, *Multimode Fiber Ruler for Detecting Nanometric Displacements*, APL Photonics **7**, 086103, 1 (2022).

[97] H. Zang, Z. Xi, Z. Zhang, Y. Lu, and P. Wang, *Ultrasensitive and Long-Range Transverse Displacement Metrology with Polarization-Encoded Metasurface*, Sci. Adv. **8**, eadd1973, 1 (2022).

[98] W. Yang, R. Lowe-Webb, S. Rabello, J. Hu, J.-Y. Lin, J. D. Heaton, M. V. Dusa, A. J. den Boef, M. van der Schaar, and A. Hunter, *Novel diffraction-based spectroscopic method for overlay metrology*, in *Metrology, Inspection, and Process Control for Microlithography XVII* (SPIE, 2003), vol. 5038, pp. 200–207.

[99] S. Pancharatnam, *Generalized Theory of Interference, and its Applications: Part I. Coherent Pencils*, in *Proc. Indian Acad. Sci. - Sect. A.* (1956), vol. 44, pp. 247–262.

[100] M. V. Berry, *The Adiabatic Phase and Pancharatnam's Phase for Polarized Light*, J. Mod. Opt. **34**, 1401 (1987).

[101] E. Hasman, V. Kleiner, G. Biener, and A. Niv, *Polarization Dependent Focusing Lens by use of Quantized Pancharatnam-Berry Phase Diffractive Optics*, Appl. Phys. Lett. **82**, 328 (2003).

[102] X. Ding, F. Monticone, K. Zhang, L. Zhang, D. Gao, S. N. Burokur, A. de Lustrac, Q. Wu, C.-W. Qiu, and A. Alu, *Ultrathin Pancharatnam-Berry Metasurface with Maximal Cross-Polarization Efficiency*, Adv. Mater. **27**, 1195 (2015).

[103] A. A. Michelson, *On the Spectra of Imperfect Gratings*, Astrophys. J. **18**, 278 (1903).

[104] A. W. Lohmann, and D. Paris, *Binary Fraunhofer Holograms, Generated by Computer*, Appl. Opt. **6**, 1739 (1967).

[105] B. R. Brown, and A. W. Lohmann, *Complex Spatial Filtering with Binary Masks*, Appl. Opt. **5**, 967 (1966).

[106] M. Khorasaninejad, A. Ambrosio, P. Kanhaiya, and F. Capasso, *Broadband and Chiral Binary Dielectric Meta-Holograms*, Sci. Adv. **2**, e1501258, 1 (2016).

[107] C. M. Linton, *Lattice Sums for the Helmholtz Equation*, SIAM rev. **52**, 630 (2010).

[108] B. Wang, F. Dong, Q.-T. Li, D. Yang, C. Sun, J. Chen, Z. Song, L. Xu, W. Chu, Y.-F. Xiao, et al., *Visible-Frequency Dielectric Metasurfaces for Multiwavelength Achromatic and Highly Dispersive Holograms*, Nano Lett. **16**, 5235 (2016).

[109] C. Messinis, M. Adhikary, T. Cromwijk, T. T. van Schaijk, S. Witte, J. F. de Boer, and A. den Boef, *Pupil Apodization in Digital Holographic Microscopy for Reduction of Coherent Imaging Effects*, Opt. Cont. **1**, 1202 (2022).

[110] Z. Xi, S. Konijnenberg, and H. Urbach, *Information-Efficient Metagrating for Transverse-Position Metrology*, Phys. Rev. Appl. **14**, 014026, 1 (2020).

[111] Z. Li, R. Pestourie, Z. Lin, S. G. Johnson, and F. Capasso, *Empowering Metasurfaces with Inverse Design: Principles and Applications*, ACS Photonics **9**, 2178 (2022).

[112] G. Binnig, C. F. Quate, and C. Gerber, *Atomic Force Microscope*, Phys. Rev. Lett. **56**, 930 (1986).

[113] S. Emir Diltemiz, R. Keçili, A. Ersöz, and R. Say, *Molecular Imprinting Technology in Quartz Crystal Microbalance (QCM) sensors*, Sensors **17**, 454 (2017).

[114] R. G. Leisure, and F. A. Willis, *Resonant Ultrasound Spectroscopy*, J. Phys.: Condens. Matter **9**, 6001 (1997).

[115] M. T. Vlaardingerbroek, and J. A. Boer, *Magnetic Resonance Imaging: Theory and Practice* (Springer Science & Business Media, 2013).

[116] P. Zijlstra, P. M. Paulo, and M. Orrit, *Optical Detection of Single Non-Absorbing Molecules using the Surface Plasmon Resonance of a Gold Nanorod*, Nature Nanotechnol. **7**, 379 (2012).

[117] G. A. Lopez, M.-C. Estevez, M. Soler, and L. M. Lechuga, *Recent Advances in Nanoplasmonic Biosensors: Applications and Lab-on-a-Chip Integration*, Nanophotonics **6**, 123 (2017).

[118] J. M. Bingham, J. N. Anker, L. E. Kreno, and R. P. Van Duyne, *Gas Sensing with High-Resolution Localized Surface Plasmon Resonance Spectroscopy*, J. Am. Chem. Soc. **132**, 17358 (2010).

[119] A. Tittl, H. Giessen, and N. Liu, *Plasmonic Gas and Chemical Sensing*, Nanophotonics **3**, 157 (2014).

[120] M. Aspelmeyer, T. J. Kippenberg, and F. Marquardt, *Cavity Optomechanics*, Rev. Mod. Phys. **86**, 1391 (2014).

[121] B.-B. Li, L. Ou, Y. Lei, and Y.-C. Liu, *Cavity Optomechanical Sensing*, Nanophotonics **10**, 2799 (2021).

[122] B. Luk'yanchuk, N. I. Zheludev, S. A. Maier, N. J. Halas, P. Nordlander, H. Giessen, and C. T. Chong, *The Fano Resonance in Plasmonic Nanostructures and Metamaterials*, Nat. Mater. **9**, 707 (2010).

[123] A. E. Cetin, and H. Altug, *Fano Resonant Ring/Disk Plasmonic Nanocavities on Conducting Substrates for Advanced Biosensing*, ACS Nano **6**, 9989 (2012).

[124] T. A. Wolterink, R. D. Buijs, G. Gerini, A. F. Koenderink, and E. Verhagen, *Localizing Nanoscale Objects using Nanophotonic Near-Field Transducers*, Nanophotonics **10**, 1723 (2021).

[125] M. Neugebauer, P. Woźniak, A. Bag, G. Leuchs, and P. Banzer, *Polarization-*

Controlled Directional Scattering for Nanoscopic Position Sensing, Nat. Commun. **7**, 11286 (2016).

[126] S. Nechayev, J. S. Eismann, M. Neugebauer, and P. Banzer, *Shaping Field Gradients for Nanolocalization*, ACS Photonics **7**, 581 (2020).

[127] M. V. Rybin, P. V. Kapitanova, D. S. Filonov, A. P. Slobozhanyuk, P. A. Belov, Y. S. Kivshar, and M. F. Limonov, *Fano Resonances in Antennas: General Control over Radiation Patterns*, Phys. Rev. B **88**, 205106 (2013).

[128] J. Yan, P. Liu, Z. Lin, H. Wang, H. Chen, C. Wang, and G. Yang, *Directional Fano Resonance in a Silicon Nanosphere Dimer*, ACS Nano **9**, 2968 (2015).

[129] Y. Yang, I. I. Kravchenko, D. P. Briggs, and J. Valentine, *All-Dielectric Metasurface Analogue of Electromagnetically Induced Transparency*, Nat. Commun. **5**, 5753 (2014).

[130] S. Campione, S. Liu, L. I. Basilio, L. K. Warne, W. L. Langston, T. S. Luk, J. R. Wendt, J. L. Reno, G. A. Keeler, I. Brener, et al., *Broken Symmetry Dielectric Resonators for high Quality Factor Fano Metasurfaces*, ACS Photonics **3**, 2362 (2016).

[131] J. Kühne, J. Wang, T. Weber, L. Kühner, S. A. Maier, and A. Tittl, *Fabrication Robustness in BIC Metasurfaces*, Nanophotonics **10**, 4305 (2021).

[132] M. Hentschel, D. Dregely, R. Vogelgesang, H. Giessen, and N. Liu, *Plasmonic Oligomers: the Role of Individual Particles in Collective Behavior*, ACS Nano **5**, 2042 (2011).

[133] M. Frimmer, T. Coenen, and A. F. Koenderink, *Signature of a Fano resonance in a Plasmonic Metamolecule's Local Density of Optical States*, Phys. Rev. Lett. **108**, 077404 (2012).

[134] E. Melik-Gaykazyan, K. Koshelev, J.-H. Choi, S. S. Kruk, A. Bogdanov, H.-G. Park, and Y. Kivshar, *From Fano to Quasi-BIC Resonances in Individual Dielectric Nanoantennas*, Nano Lett. **21**, 1765 (2021).

[135] M. V. Rybin, K. L. Koshelev, Z. F. Sadrieva, K. B. Samusev, A. A. Bogdanov, M. F. Limonov, and Y. S. Kivshar, *High-Q Supercavity Modes in Subwavelength Dielectric Resonators*, Phys. Rev. Lett. **119**, 243901 (2017).

[136] A. A. Bogdanov, K. L. Koshelev, P. V. Kapitanova, M. V. Rybin, S. A. Gladyshev, Z. F. Sadrieva, K. B. Samusev, Y. S. Kivshar, and M. F. Limonov, *Bound States in the Continuum and Fano Resonances in the Strong Mode Cupling Regime*, Adv. Phot. **1**, 016001 (2019).

[137] L. Kühner, L. Sortino, R. Berté, J. Wang, H. Ren, S. A. Maier, Y. Kivshar, and A. Tittl, *Radial Bound States in the Continuum for Polarization-Invariant Nanophotonics*, Nat. Commun. **13**, 4992 (2022).

[138] A. Vaskin, R. Kolkowski, A. F. Koenderink, and I. Staude, *Light-Emitting Metasurfaces*, Nanophotonics **8**, 1151 (2019).

[139] F. J. García de Abajo, *Colloquium: Light Scattering by Particle and Hole Arrays*, Rev. Mod. Phys. **79**, 1267 (2007).

[140] L. Novotny, and B. Hecht, *Principles of Nano-Optics* (Cambridge university press, 2012).

[141] R. Gutiérrez-Cuevas, D. Bouchet, J. de Rosny, and S. M. Popoff, *Reaching the Precision Limit with Tensor-Based Wavefront Shaping*, Nat. Commun. **15**, 6319

(2024).

[142] D. Bouchet, R. Carminati, and A. P. Mosk, *Influence of the Local Scattering Environment on the Localization Precision of Single Particles*, Phys. Rev. Lett. **124**, 133903 (2020).

[143] F. Balzarotti, Y. Eilers, K. C. Gwosch, A. H. Gynnå, V. Westphal, F. D. Stefani, J. Elf, and S. W. Hell, *Nanometer Resolution Imaging and Tracking of Fluorescent Molecules with Minimal Photon Fluxes*, Science **355**, 606 (2017).

[144] J. Hüpfl, F. Russo, L. M. Rachbauer, D. Bouchet, J. Lu, U. Kuhl, and S. Rotter, *Continuity Equation for the Flow of Fisher Information in Wave Scattering*, Nat. Phys. **20**, 1294 (2024).

[145] C. F. Bohren, and D. R. Huffman, *Absorption and Scattering of Light by Small Particles* (John Wiley & Sons, 2008).

[146] W. Weber, and G. Ford, *Propagation of Optical Excitations by Dipolar Interactions in Metal Nanoparticle Chains*, Phys. Rev. B **70**, 125429 (2004).

[147] E. M. V. Association, et al., *Standard for Characterization of Image Sensors and Cameras*, EMVA Standard **1288** (2010).

[148] B. Kaur, S. Kumar, and B. K. Kaushik, *Novel Wearable Optical Sensors for Vital Health Monitoring Systems—A Review*, Biosensors **13**, 181 (2023).

[149] J. Heikenfeld, A. Jajack, J. Rogers, P. Gutruf, L. Tian, T. Pan, R. Li, M. Khine, J. Kim, and J. Wang, *Wearable Sensors: Modalities, Challenges, and Prospects*, Lab on a Chip **18**, 217 (2018).

[150] Y. Guo, C. Liu, R. Ye, and Q. Duan, *Advances on Water Quality Detection by UV-VIS Spectroscopy*, Appl. Sci. **10**, 6874 (2020).

[151] P. K. Jain, X. Huang, I. H. El-Sayed, and M. A. El-Sayed, *Noble Metals on the Nanoscale: Optical and Photothermal Properties and some Applications in Imaging, Sensing, Biology, and Medicine*, Acc. Chem. Res. **41**, 1578 (2008).

[152] Y. Kivshar, *The Rise of Mie-tronics*, Nano Lett. **22**, 3513 (2022).

[153] A. Kinkhabwala, Z. Yu, S. Fan, Y. Avlasevich, K. Müllen, and W. E. Moerner, *Large Single-Molecule Fluorescence Enhancements Produced by a Bowtie Nanoantenna*, Nat. Photonics **3**, 654 (2009).

[154] X.-M. Qian, and S. M. Nie, *Single-Molecule and Single-Nanoparticle SERS: from Fundamental Mechanisms to Biomedical Applications*, Chem. Soc. Rev. **37**, 912 (2008).

[155] D.-K. Lim, K.-S. Jeon, J.-H. Hwang, H. Kim, S. Kwon, Y. D. Suh, and J.-M. Nam, *Highly Uniform and Reproducible Surface-Enhanced Raman Scattering from DNA-Tailorable Nanoparticles with 1-nm Interior Gap*, Nat. Nanotechnol. **6**, 452 (2011).

[156] G. Baffou, F. Cichos, and R. Quidant, *Applications and Challenges of Thermoplasmonics*, Nat. Mater. **19**, 946 (2020).

[157] P. C. Ray, *Size and Shape Dependent Second Order Nonlinear Optical Properties of Nanomaterials and their Application in Biological and Chemical Sensing*, Chem. Rev. **110**, 5332 (2010).

[158] M. Mesch, B. Metzger, M. Hentschel, and H. Giessen, *Nonlinear Plasmonic Sensing*, Nano Lett. **16**, 3155 (2016).

[159] K. Koshelev, A. Bogdanov, and Y. Kivshar, *Meta-Optics and Bound States in the*

Continuum, Science Bulletin **64**, 836 (2019).

[160] J. Wang, J. Kühne, T. Karamanos, C. Rockstuhl, S. A. Maier, and A. Tittl, *All-Dielectric Crescent Metasurface Sensor Driven by Bound States in the Continuum*, Adv. Funct. Mater. **31**, 2104652 (2021).

[161] Z. Yu, H. Li, T. Zhong, J.-H. Park, S. Cheng, C. M. Woo, Q. Zhao, J. Yao, Y. Zhou, X. Huang, et al., *Wavefront Shaping: a Versatile Tool to Conquer Multiple Scattering in Multidisciplinary Fields*, The Innovation **3**, 100292 (2022).

[162] I. M. Vellekoop, A. Lagendijk, and A. Mosk, *Exploiting Disorder for Perfect Focusing*, Nat. Photonics **4**, 320 (2010).

[163] A. Boniface, J. Dong, and S. Gigan, *Non-Invasive Focusing and Imaging in Scattering Media with a Fluorescence-based Transmission Matrix*, Nat. Commun. **11**, 6154 (2020).

[164] A. C. Overvig, S. C. Malek, M. J. Carter, S. Shrestha, and N. Yu, *Selection Rules for Quasibound States in the Continuum*, Phys. Rev. B **102**, 035434 (2020).

[165] A. Overvig, and A. Alù, *Wavefront-Selective Fano Resonant Metasurfaces*, Adv. Phot. **3**, 026002 (2021).

[166] D. Bouchet, J. Seifert, and A. P. Mosk, *Optimizing Illumination for Precise Multi-Parameter Estimations in Coherent Diffractive Imaging*, Optics Lett. **46**, 254 (2021).

[167] P. Ambichl, W. Xiong, Y. Bromberg, B. Redding, H. Cao, and S. Rotter, *Super-and Anti-Principal-Modes in Multimode Waveguides*, Phys. Rev. X **7**, 041053 (2017).

[168] A. E. Willner, H. Huang, Y. Yan, Y. Ren, N. Ahmed, G. Xie, C. Bao, L. Li, Y. Cao, Z. Zhao, et al., *Optical Communications using Orbital Angular Momentum Beams*, Adv. Opt. Photonics **7**, 66 (2015).

[169] K. Catchpole, , and A. Polman, *Plasmonic Solar Cells*, Opt. Express **16**, 21793 (2008).

[170] J. N. Anker, W. P. Hall, O. Lyandres, N. C. Shah, J. Zhao, and R. P. Van Duyne, *Biosensing with Plasmonic Nanosensors*, Nat. Mater. **7**, 442 (2008).

[171] G. T. Reed, G. Mashanovich, F. Y. Gardes, and D. Thomson, *Silicon Optical Modulators*, Nat. Photonics **4**, 518 (2010).

[172] T.-K. Wu, *Frequency Selective Surfaces*, Encyclopedia RF Microwave Engineering (2005).

[173] W. W. Salisbury, *Absorbent Body for Electromagnetic Waves*, US patent (1952).

[174] R. L. Fante, and M. T. McCormack, *Reflection Properties of the Salisbury Screen*, IEEE Trans. Antennas Propag. **36**, 1443 (1988).

[175] N. I. Landy, S. Sajuyigbe, J. J. Mock, D. R. Smith, and W. J. Padilla, *Perfect Metamaterial Absorber*, Phys. Rev. Lett. **100**, 207402 (2008).

[176] C. M. Watts, X. Liu, and W. J. Padilla, *Metamaterial Electromagnetic Wave Absorbers*, Adv. Mater. **24**, OP98 (2012).

[177] N. Liu, M. Mesch, T. Weiss, M. Hentschel, and H. Giessen, *Infrared Perfect Absorber and its Application as Plasmonic Sensor*, Nano Lett. **10**, 2342 (2010).

[178] Y. Avitzour, Y. A. Urzhumov, and G. Shvets, *Wide-Angle Infrared Absorber Based on a Negative-Index Plasmonic Metamaterial*, Phys. Rev. B **79**, 045131 (2009).

[179] M. Pu, C. Hu, M. Wang, C. Huang, Z. Zhao, C. Wang, Q. Feng, and X. Luo, *Design*

Principles for Infrared Wide-Angle Perfect Absorber Based on Plasmonic Structure, Opt. Express **19**, 17413 (2011).

[180] S. Thongrattanasiri, F. H. Koppens, and F. J. García de Abajo, *Complete Optical Absorption in Periodically Patterned Graphene*, Phys. Rev. Lett. **108**, 047401 (2012).

[181] K. Aydin, V. E. Ferry, R. M. Briggs, and H. A. Atwater, *Broadband Polarization-Independent Resonant Light Absorption using Ultrathin Plasmonic Super Absorbers*, Nat. Commun. **2**, 517 (2011).

[182] C. Hu, Z. Zhao, X. Chen, and X. Luo, *Realizing Near-Perfect Absorption at Visible Frequencies*, Opt. Express **17**, 11039 (2009).

[183] A. Berkhout, and A. F. Koenderink, *Perfect Absorption and Phase Singularities in Plasmon Antenna Array Etalons*, ACS Photonics **6**, 2917 (2019).

[184] W. Wan, Y. Chong, L. Ge, H. Noh, A. D. Stone, and H. Cao, *Time-Reversed Lasing and Interferometric Control of Absorption*, Science **331**, 889 (2011).

[185] Y. Chong, L. Ge, H. Cao, and A. D. Stone, *Coherent Perfect Absorbers: Time-Reversed Lasers*, Phys. Rev. Lett. **105**, 053901 (2010).

[186] S. Tretyakov, *Maximizing Absorption and Scattering by Dipole Particles*, Plasmonics **9**, 935 (2014).

[187] R. Alaee, M. Albooyeh, and C. Rockstuhl, *Theory of Metasurface based Perfect Absorbers*, J. Phys. D: Appl. Phys. **50**, 503002 (2017).

[188] V. Grigoriev, N. Bonod, J. Wenger, and B. Stout, *Optimizing Nanoparticle Designs for Ideal Absorption of Light*, ACS Photonics **2**, 263 (2015).

[189] Z. Ruan, and S. Fan, *Superscattering of Light from Subwavelength Nanostructures*, Phys. Rev. Lett. **105**, 013901 (2010).

[190] G. Zumofen, N. Mojarad, V. Sandoghdar, and M. Agio, *Perfect Reflection of Light By an Oscillating Dipole*, Phys. Rev. Lett. **101**, 180404 (2008).

[191] I. Gerhardt, G. Wrigge, P. Bushev, G. Zumofen, M. Agio, R. Pfab, and V. Sandoghdar, *Strong Extinction of a Laser Beam by a Single Molecule*, Phys. Rev. Lett. **98**, 033601 (2007).

[192] J. Zirkelbach, B. Gmeiner, J. Renger, P. Türschmann, T. Utikal, S. Götzinger, and V. Sandoghdar, *Partial Cloaking of a Gold Particle by a Single Molecule*, Phys. Rev. Lett. **125**, 103603 (2020).

[193] A. N. Vamivakas, M. Atatüre, J. Dreiser, S. Yilmaz, A. Badolato, A. K. Swan, B. B. Goldberg, A. Imamoğlu, and M. Ünlü, *Strong Extinction of a Far-Field Laser Beam by a Single Quantum Dot*, Nano Lett. **7**, 2892 (2007).

[194] S. Van Enk, and H. Kimble, *Strongly Focused Light Beams Interacting with Single Atoms in Free Space*, Phys. Rev. A **63**, 023809 (2001).

[195] M. Stobińska, G. Alber, and G. Leuchs, *Perfect Excitation of a Matter Qubit by a Single Photon in Free Space*, Europhys. Lett. **86**, 14007 (2009).

[196] E. J. Dias, and F. J. García de Abajo, *Complete Coupling of Focused Light to Surface Polaritons*, Optica **8**, 520 (2021).

[197] A. Proskurin, A. Bogdanov, and D. G. Baranov, *Perfect Absorption of a Focused Light Beam by a Single Nanoparticle*, Laser Photonics Rev. **15**, 2000430 (2021).

[198] V. Lakshminarayanan, and A. Fleck, *Zernike Polynomials: a Guide*, J. Mod. Opt.

58, 545 (2011).

[199] E. Goi, S. Schoenhardt, and M. Gu, *Direct Retrieval of Zernike-based Pupil Functions using Integrated Diffractive Deep Neural Networks*, Nat. Commun. **13**, 7531 (2022).

[200] L. Miccio, D. Alfieri, S. Grilli, P. Ferraro, A. Finizio, L. De Petrocellis, and S. Nicola, *Direct Full Compensation of the Aberrations in Quantitative Phase Microscopy of Thin Objects by a Single Digital Hologram*, Appl. Phys. Lett. **90**, 041104 (2007).

[201] N. Verellen, Y. Sonnefraud, H. Sobhani, F. Hao, V. V. Moshchalkov, P. V. Dorpe, P. Nordlander, and S. A. Maier, *Fano Resonances in Individual Coherent Plasmonic Nanocavities*, Nano Lett. **9**, 1663 (2009).

[202] E. J. Dias, and F. J. García de Abajo, *Fundamental Limits to the Coupling Between Light and 2D Polaritons by Small Scatterers*, ACS Nano **13**, 5184 (2019).

[203] S. Abdullah, E. J. Dias, J. Krpensky, V. Mkhitaryan, and F. J. García de Abajo, *Toward Complete Optical Coupling to Confined Surface Polaritons*, ACS Photonics **11**, 2183 (2024).

[204] X. Li, G. Haberfehlner, U. Hohenester, O. Stéphan, G. Kothleitner, and M. Kociak, *Three-Dimensional Vectorial Imaging of Surface Phonon Polaritons*, Science **371**, 1364 (2021).

[205] A. V. Zayats, I. I. Smolyaninov, and A. A. Maradudin, *Nano-Optics of Surface Plasmon Polaritons*, Phys. Rep. **408**, 131 (2005).

[206] G. Rosenblatt, B. Simkhovich, G. Bartal, and M. Orenstein, *Nonmodal Plasmonics: Controlling the Forced Optical Response of Nanostructures*, Phys. Rev. X **10**, 011071 (2020).

[207] C. Sauvan, T. Wu, R. Zarouf, E. A. Muljarov, and P. Lalanne, *Normalization, Orthogonality, and Completeness of Quasinormal Modes of Open Systems: the Case of Electromagnetism*, Opt. Express **30**, 6846 (2022).

[208] W. Yan, R. Faggiani, and P. Lalanne, *Rigorous Modal Analysis of Plasmonic Nanoresonators*, Phys. Rev. B **97**, 205422 (2018).

[209] P. Lalanne, W. Yan, K. Vynck, C. Sauvan, and J.-P. Hugonin, *Light Interaction with Photonic and Plasmonic Resonances*, Laser Photonics Rev. **12**, 1700113 (2018).

[210] F. Betz, F. Binkowski, and S. Burger, *RPExpand: Software for Riesz Projection Expansion of Resonance Phenomena*, SoftwareX **15**, 100763 (2021).

[211] F. Binkowski, F. Betz, R. Colom, M. Hammerschmidt, L. Zschiedrich, and S. Burger, *Quasinormal Mode Expansion of Optical Far-Field Quantities*, Phys. Rev. B **102**, 035432 (2020).

[212] W. Yan, P. Lalanne, and M. Qiu, *Shape Deformation of Nanoresonator: a Quasinormal-Mode Perturbation Theory*, Phys. Rev. Lett. **125**, 013901 (2020).

[213] F. Binkowski, F. Betz, M. Hammerschmidt, P.-I. Schneider, L. Zschiedrich, and S. Burger, *Computation of Eigenfrequency Sensitivities using Riesz Projections for Efficient Optimization of Nanophotonic Resonators*, Commun. Phys. **5**, 202 (2022).

[214] H. Liu, C. Guo, G. Vampa, J. L. Zhang, T. Sarmiento, M. Xiao, P. H. Bucksbaum, J. Vučković, S. Fan, and D. A. Reis, *Enhanced High-Harmonic Generation from an All-Dielectric Metasurface*, Nat. Phys. **14**, 1006 (2018).

Summary and Outlook

The interplay between light and information is at the heart of several foundational technologies in our current day society, and continues to drive innovative solutions to the ever growing challenges in today's Information Age. Optical fibers and photonic integrated circuits are indispensable for high-speed *transfer* of information, remarkable scientific progress is made in *processing* of information through all-optical computing, and advanced optical instrumentation has been developed to *retrieve* information from physical systems through measurements. The overarching field of extracting information about specific parameters of a system by performing an optical measurement is termed *optical metrology*, and is the main subject matter of this thesis.

A highly relevant application domain of optical metrology is the semiconductor chip manufacturing industry. The most advanced modern chips are composed of complex networks of components that need to be fabricated with an accuracy down to the sub-nanometer scale, which is comparable to the dimensions of a single atom. The increasing demands for more powerful chips, fueled by developments in artificial intelligence (AI), continue to impose stricter requirements on chip fabrication, and the development of optical metrology protocols that efficiently extract structural information about nanoscale environments that comprise the chip is vital to enable accurate process control. This thesis proposes several strategies to conduct information efficient metrology on such nanoscale environments. Throughout the thesis, we use the concept of Fisher information to quantify the amount of information a certain measurement protocol contains, which is directly related to the precision with which relevant unknown parameters can be estimated from measured data.

An optical metrology protocol consists of a specific illumination scheme that interrogates a nanoscale environment, which in turn generates a detected signal from which relevant parameters are to be estimated. Here, an efficient interplay between the illumination, the nanoscale environment, and the detection modality is crucial to obtain maximum Fisher information about the parameter to be retrieved. Several tools exist to optimize an optical metrology protocol on all three separate fronts. The field of nanophotonics, for instance, provides a rich and flexible toolbox to shape the nanoscale environment so that particular nanoscale sensitivities are enhanced. For example, individual dielectric nanoparticles can host Mie resonant modes that are highly sensitive to structural variations in the particle. A second, more flexible strategy for engineering the nanoscale environment is through the use of metasurfaces, which are two-dimensional patches of designer nanoparticles patterned on a surface that are specifically programmed in size and shape. Metasurfaces can result in strong collective effects between the individual nanoparticles on the surface. One of these collective effects is the Fano resonance, which is a powerful mechanism for generating enhanced response functions in nanoscale sensing experiments. Fano-resonant metasurfaces can be flexibly designed through the physics of quasi bound states in the continuum, which are extended resonant states with a tunable quality factor that depends on a structural asymmetry parameter within the metasurface. These Fano-resonant metasurfaces have already been exploited in many sensing experiments to detect nanoscale refractive index perturbation in the form of biological molecules. The generated responses on the nanoscale are subsequently transduced into detectable far-field signals, and several experimental techniques can be used for efficient read out. These include conventional microscopy for direct imaging of a sample, Fourier scatterometry for angle-resolved detection, spectroscopy to disperse a signal in wavelength components, holography for phase retrieval and polarimetry for polarization characterization. Finally, on the side of the illuminations, significant progress in the field of structured light has lead to a variety of techniques based on spatial light modulating devices for shaping far-field illuminations in the form of wavefront shaping, polarization shaping and ultrafast pulse shaping. In the context of sensing, the wavefront shaping community has recently introduced the concept of "maximum information states", which are specifically tailored modes of far-field illuminations that generate maximum information about a relevant parameter to be sensed.

While many research groups have already made significant efforts over the past years to develop efficient nanoscale metrology strategies, usually one, or at most two, of the three key aspects of a measurement procedure are optimized. The work performed in this thesis is motivated by the goal to optimize all three ingredients of an optical metrology protocol concurrently. We propose several metrology platforms that combine concepts from the fields of metasurfaces, wavefront shaping, Fourier microscopy and information theory to efficiently retrieve information about parameters embedded in nanoscale systems.

In **Chapter 2**, we report on an interlaced displacement sensing platform comprised of a diffractive metasurface capable of resolving nanometer structural misalignments within a device layer. We argue that the physics of the sensing experiment relies on a combination of Pancharatnam-Berry and detour phase shifts, and show how these phase shifts efficiently transduce nanoscale displacements into specific polarization fingerprints in the far-field diffraction channels. We investigate several polarimetric measurement protocols suitable for efficient semiconductor metrology applications, and discuss how the metasurface can be optimized for an optimally informative response. Finally, we show that the proposed platform is capable of resolving arbitrary two-dimensional displacements on a device.

In **Chapter 3**, we combine the physics of quasi-BIC metasurfaces with a Fourier scatterometry read-out scheme for efficient detection of nanometer structural displacements. Conventional quasi-BIC metasurface sensing experiments rely on measuring spectral distortions of Fano lineshapes resulting from perturbations on the nanoscale, in which the detected signal is usually integrated over all scattering angles. Here, instead, we propose to resolve the resonant scattering in Fourier space, and experimentally demonstrate that deeply sub-wavelength perturbations can lead to notable contrasts in directional scattering. We discuss the nanophotonic mechanisms responsible for the resonant directional scattering through analysis of the fundamental modes of the system. Finally, by using information theory, we compare the Fisher information content between a conventional angle-integrated measurement and an angle-resolved measurement modality, and demonstrate that up to a factor of 7 in Fisher information can be gained from a Fourier space measurement.

In **Chapter 4**, we theoretically investigate how structuring an incident illumination affects the amount of information that can be retrieved from resonant metasurface sensors, such as those discussed in **Chapter 3**. Sensing experiments with resonant metasurfaces are usually performed with plane wave or focused illumination conditions, in which typically a single quasi-BIC mode is excited. By analyzing the full eigenmode spectrum of a resonant dielectric metasurface, we uncover a plethora of quasi-BIC modes that cannot be adressed by such trivial illumination schemes. We show how the wavefront shaping toolbox can be exploited to design structured excitations that generate sufficient modal overlap to selectively excite these quasi-BIC resonances, and that these wavefront selective excitations could provide more Fisher information than conventional excitations based on plane waves.

In **Chapter 5**, we utilize the wavefront shaping toolbox to experimentally investigate optimal extinction by both individual scatterers and finite-sized arrays positioned above a planar mirror. To this end, we fabricate a set of periodic planar arrays with varying sizes — from extended lattices down to single nanoparticles — each separated from a back reflector, and study how finite-size lattice effects influence reflectivity attenuation. We show how the incident wavefront of a tightly focused beam can be tailored to optimally couple light into a single nanoparticle-on-mirror structure. By comparing these optimal illumination profiles with analytical models of dipole scattering above a back reflector, we qualitatively confirm that the engineered wavefronts match the time-reversed modal radiation patterns of the nanoscatterer in the presence of the mirror. Under these optimal conditions, we achieve up to 70% extinction of a tightly focused beam by a single plasmonic nanoparticle, and as high as 90% extinction for a sub-wavelength cluster of 2x2 nanoparticles.

Future perspectives

The results presented in this thesis present initial stepping stones in the direction of optical metrology platforms that optimally extract information from nanoscale systems, by optimizing the interplay between excitations, nanoscale environments, and detection settings. In the following, we will discuss remaining open questions that could serve as potential continuations of this thesis.

Optimal nanophotonic sensor design via hybrid QNM/information theory: Recently, tremendous theoretical progress has been made in the computational nanophotonics community to provide a semi-analytical description of resonant nanosystems through the framework of quasi-normal-modes (QNMs) [207–211] . This framework allows to efficiently describe and compute relevant experimental observables emanating from resonant excitations on the nanoscale purely in terms of the natural modes, or QNMs, of the system. In addition, initial works on QNM perturbation theory [212, 213] have demonstrated accurate reconstructions of modal and far-field sensitivities to nanoscale perturbations. An open fundamental question that directly applies to this framework is: *For a given observable, how does one design a resonant system that generates maximum information about a specific nanoscale parameter?* One can imagine, for example, that certain types of Fano resonances are more sensitive to specific perturbations than others, as we have already eluded to in **Chapter 4**. *What is the most informative Fano resonance, and how does this relate to the field distributions of the relevant QNMs?* This question could be tackled by developing a hybrid QNM/information theoretical framework, in combination with inverse design strategies, and would greatly aid the nanophotonic sensing community to gain fundamental insights into optimal resonance-based sensor design motifs.

Non-linear metasurfaces for metrology: The works of this thesis are performed in the regime of linear light scattering. Resonant metasurfaces are, however, also exploited to efficiently generate non-linear signals [27, 28], such as high harmonic generation [214]. *How much information can be retrieved from a non-linear metrology protocol, and is there an information advantage with respect to linear optical metrology?* Three crucial considerations that influence the amount of information that can be retrieved are: the upconverted frequency of the non-linear signal, the efficiency with which the non-linear signal is generated, and the power law dependence of high-harmonic contrasts with respect to the excitation power. As a testbed to investigate these questions, the metaring platform discussed in **Chapter 3** could be tuned such that the Fano resonances spectrally overlap with the excitation of an ultrafast laser pulse. Both linear and non-linear light scattering can be acquired individually through spectral filtering, after which the Fisher information in both signals can be determined and compared.

Optimal spatio-temporal shaping of excitations: In **Chapter 4** we showed that supplying spatially structured excitations that maximize the overlap with a relevant fundamental mode enhances the amount of information that can be retrieved in a sensing experiment. Instead of structuring an excitation in the spatial domain, advanced ultrafast pulse shaping techniques [65, 66] can be used to shape an excitation in the spectral and temporal domains as well, as we have briefly mentioned in **Chapter 1**. *Is there an optimally informative pulse shape to sense perturbations? How does this pulse shape relate to the spectral properties of the fundamental modes of the system?* Ultrafast pulse shaping could also be combined with wavefront shaping techniques, laying the groundwork for optimally informative spatio-temporal excitations in nanoscale sensors.

Samenvatting

De wisselwerking tussen licht en informatie ligt ten grondslag aan verscheidene fundamentele technologieën in onze hedendaagse samenleving, en blijft innovatieve oplossingen bieden op de almaar groeiende uitdagingen in het huidige Informatie Tijdperk. Optische vezels en fotonische geïntegreerde schakelingen zijn onmisbaar voor de *overdracht* van informatie op hoge snelheid, opmerkelijke wetenschappelijke vooruitgang is geboekt in het *verwerken* van informatie door middel van optische berekeningen, en geavanceerde optische instrumentatie is ontwikkeld om informatie te *winnen* van fysische systemen vanuit metingen. Het overkoepelende veld dat informatie vanuit een systeem probeert te winnen door middel van een optische meting wordt *optische metrologie* genoemd, en vormt het hoofdonderwerp van dit proefschrift.

Een extreem relevant applicatie domein binnen de optische metrologie is de halfgeleider chip industrie. De meest geavanceerde moderne chips bestaan uit complexe netwerken van componenten die gefabriceerd dienen te worden met een nauwkeurigheid op de sub-nanometer schaal, vergelijkbaar met de grootte van een enkel atoom. De toenemende vraag naar krachtigere chips, aangedreven door onwtikkelingen binnen de kunstmatige intelligentie, blijven strengere eisen stellen aan de chip fabricatie. De ontwikkeling van optische metrologie protocollen die efficient structurele informatie vanuit zulke omgevingen op de nanometer schaal kunnen extraheren zijn essentieel om een nauwkeurige procescontrole uit te voeren. Dit proefschrift stelt verscheidene strategieën voor om informatie efficiënte metrologie uit te oefenen. Gedurende het proefschrift gebruiken we het concept van Fisher-informatie om de hoeveelheid informatie te kwantificeren die een bepaald meetprotocol bevat. Dit concept houdt direct verband met de nauwkeurigheid waarmee relevante onbekende parameters kunnen worden geschat vanuit gemeten data.

Een optisch metrologieprotocol bestaat uit een specifieke belichtingsmethode dat een omgeving op de nanoschaal ondervraagt, die op zijn beurt een signaal genereert waaruit relevante parameters moeten worden geschat vanuit gemete data. Een efficiënte wisselwerking tussen de belichting, de omgeving op nanoschaal en de detectie is hier van cruciaal belang om maximale Fisher informatie over de parameter te verkrijgen. Er bestaan verschillende methodes om een optisch metrologieprotocol te optimaliseren op alle drie de afzonderlijke fronten. Het gebied van de nanofotonica biedt bijvoorbeeld een rijke en flexibele gereedschapset om de omgeving op de nanoschaal zo vorm te geven dat bepaalde gevoeligheden worden versterkt. Zo kunnen individuele diëlektrische nanodeeltjes Mie-resonanties bevatten die zeer gevoelig zijn voor grootte en vorm veranderingen in het deeltje. Een tweede, flexibelere strategie voor het ontwerpen van de omgeving op de nanometer schaal gebeurt door het gebruik van metaoppervlakken: tweedimensionale roosters van nanodeeltjes die op een oppervlak zijn gevormd en die specifiek zijn geprogrammeerd in grootte en vorm. Metaoppervlakken kunnen resulteren in sterke collectieve effecten tussen de individuele nanodeeltjes op het oppervlak. Eén van deze collectieve effecten is de Fano-resonantie, dat een krachtig mechanisme is voor het genereren van verhoogde responsfuncties bij nanoschaal sensoren. Fano-resonante metaoppervlakken kunnen flexibel worden ontworpen via de natuurkunde van "quasi-gebonden toestanden in het continuüm" (quasi-BIC). Dit zijn ruimtelijke resonante toestanden met een afstembare kwaliteitsfactor die afhangt van een structurele asymmetrieparameter binnen het metaoppervlak. Fano-resonante metaoppervlakken zijn al in veel sensorexperimenten benut om nanoschaal brekingsindexverstoringen in de vorm van biologische moleculen te detecteren. Gevoeligheden op de nanoschaal worden vervolgens omgezet in detecteerbare signalen in het verre veld, en verschillende experimentele technieken kunnen worden gebruikt voor een efficiënte uitlezing. Deze omvatten conventionele microscopie voor directe beeldvorming van een monster, Fourier-scatterometrie voor hoekopgeloste detectie, spectroscopie om een signaal te ontbinden in golflengtecomponenten, holografie voor het ophalen van de fase en polarimetrie voor polarisatiekarakterisering. Tenslotte is er aanzienlijke vooruitgang geboekt op het gebied van gestructureerd licht, wat heeft geleid tot een verscheidenheid aan technieken gebaseerd op ruimtelijke lichtmodulerende apparaten voor het moduleren van verre veldbelichtingen in de vorm van golffrontvorming, polarisatievorming en ultrasnelle pulsvorming. In de context van sensoren heeft de golffrontvorming gemeenschap onlangs het concept van ‘maximale informatie toestanden’ geïntroduceerd, wat specifiek op maat gemaakte modi van verre veldbelichtingen zijn die maximale informatie genereren over een relevante parameter die moet worden gedetecteerd.

Terwijl veel onderzoeksgroepen de afgelopen jaren al aanzienlijke inspanningen hebben geleverd om efficiënte metrologiestrategieën op de nanometer schaal te ontwikkelen, worden er meestal één of hoogstens twee van de drie belangrijkste aspecten van een meetprocedure geoptimaliseerd. Het werk dat in dit proefschrift wordt uitgevoerd is gemotiveerd door het doel om alle drie de ingrediënten van een optisch metrologieprotocol tegelijkertijd te optimaliseren. Wij stellen verschillende metrologieplatformen voor die concepten uit de vakgebieden van metaoppervlakken, golffrontvorming, Fouriermicroscopie en informatietheorie combineren om efficiënt informatie op te halen over parameters die ingebed zijn in nanoschaal systemen.

In **Hoofdstuk 2** rapporteren we over een verplaatsingsdetectieplatform dat bestaat uit een diffractief metaoppervlak dat uitlijningsfouten binnen een laag op een toestel tot op enkele nanometers kan oplossen. Wij stellen dat de fysica van het detectie-experiment is gebaseerd op een combinatie van Pancharatnam-Berry en detour faseverschuivingen, en laten zien hoe verplaatsingen op de nanoschaal worden getransduceerd naar specifieke polarisatievingerafdrukken in de verre velddiffractiekanalen. We onderzoeken verschillende polarimetrische metingprotocollen die geschikt zijn voor efficiënte halfgeleidermetrologietoepassingen, en bespreken hoe het metaoppervlak kan worden geoptimaliseerd voor een optimaal informatieve gevoeligheid. Ten slotte laten we zien dat het voorgestelde platform willekeurige tweedimensionale verplaatsingen op een apparaat kan detecteren.

In **Hoofdstuk 3** combineren we de fysica van quasi-BIC metaoppervlakken met een Fourier-scatterometrie-uitleesschema voor efficiënte detectie van structurele verplaatsingen op de nanometer schaal. Conventionele sensoren gemaakt van quasi-BIC metaoppervlakken zijn afhankelijk van het meten van spectrale vervormingen van Fano-lijnvormen die resulteren uit verstoringen op de nanoschaal, waar het gedetecteerde signaal meestal is geïntegreerd over alle verstrooiingshoeken. In plaats daarvan stellen wij voor om de resonante verstrooiing op te lossen in de Fourier-ruimte, en tonen experimenteel aan dat verstoringen ver beneden de golflengte kunnen leiden tot opmerkelijke contrasten in hoekopgeloste verstrooiing. We bespreken de nanofotonische mechanismen die verantwoordelijk zijn voor de resonante directionele verstrooiing door analyse van de fundamentele modi van het systeem. Ten slotte vergelijken we, met behulp van de informatietheorie, de Fisher Informatie inhoud tussen een conventionele hoekgeïntegreerde meting en een hoek-opgeloste meetmodaliteit, en demonstreren we dat zeven maal meer Fisher-informatie kan worden gewonnen uit een Fourier-ruimtemeting.

In **Hoofdstuk 4** onderzoeken we theoretisch hoe het structureren van een inkomende belichting de hoeveelheid informatie beïnvloedt die kan worden opgehaald uit resonante metaoppervlak-sensoren, zoals die besproken in **Hoofdstuk 3**. Sensoren bestaande uit resonante metaoppervlakken worden meestal belicht met een vlakke golf, waarbij doorgaans één enkele quasi-BIC-modus is aangeslagen. Door het volledige eigenmodusspectrum van een resonant diëlektrisch metaoppervlak te analyseren ontdekken we een hele reeks aan quasi-BIC-modi die niet kunnen worden aangeslagen door zulke vlakke golven. We laten zien hoe golffrontvorming kan worden benut om gestructureerde excitaties te ontwerpen die voldoende modale overlap genereren om deze quasi-BIC-resonanties selectief aan te slaan, en dat deze golffront selectieve excitaties meer informatie kunnen bieden dan conventionele excitaties gebaseerd op vlakke golven.

In **Hoofdstuk 5** gebruiken we golffrontvorming om experimenteel onderzoek te doen naar optimale uitdoving van gefocuseerd licht door zowel individuele verstrooiers als eindige roosters van verstrooiers die boven een vlakke spiegel zijn geplaatst. Hiervoor fabriceren we een reeks periodische roosters met verschillende afmetingen — van uitgebreide roosters tot enkele nanodeeltjes — elk gescheiden van een achterreflector, en bestuderen we hoe eindige roostereffecten het uitdovingsvermogen beinvloeden. We laten zien hoe het inkomende golffront van een sterk gefocusseerde straal kan worden gemoduleerd om licht optimaal te koppelen tot een enkel nanodeeltje-op-spiegelstructuur. Door deze optimale golffront te vergelijken met analytische modellen van dipoolverstrooiing boven een spiegel, bevestigen we kwalitatief dat de ontworpen golffronten overeenkomen met de tijds-omgekeerde stralingspatronen van de nanoverstrooier in aanwezigheid van de spiegel. Onder deze optimale omstandigheden bereiken we tot 70% optische uitdoving van een sterk gefocusseerde straal door een enkel metaal nanodeeltje, en zo hoog als 90% uitdoving voor een cluster van 2x2 nanodeeltjes.

List of Publications

Related to this thesis

1. **N. Feldman**, K. M. M. Goeloe, A. J. den Boef, L. V. Amitonova and A. F. Koenderink, *Nanometer Interlaced Displacement Metrology Using Diffractive Pancharatnam-Berry and Detour Phase Metasurfaces*, ACS Photonics **11**, 5229-5238 (2024). (**Chapter 2**)
2. **N. Feldman**, A. J. den Boef, L. V. Amitonova and A. F. Koenderink, *Information Advantage in Sensing Revealed by Fano-Resonant Fourier Scatterometry*, Nature Communications, accepted. (**Chapter 3**)
3. **N. Feldman**, N. de Gaay Fortman, A. J. den Boef, L. V. Amitonova and A. F. Koenderink, *Wavefront Selective Modal Excitations for Optimally Informative Sensing in Fano-Resonant Metasurfaces*, in preparation. (**Chapter 4**)
4. **N. Feldman**, J. Pals, A. J. den Boef, F. J. García de Abajo, L. V. Amitonova and A. F. Koenderink, *Wavefront Shaping for Optimal Extinction of Focused Light by Individual Nanoscatterers*, submitted to Advanced Photonics, under review. (**Chapter 5**)

Other

5. F. Betz, F. Binkowski, J. D. Fischbach, **N. Feldman**, L. Zschiedrich, C. Rockstuhl, A. F. Koenderink and S. Burger *Uncovering Hidden Resonances in Non-Hermitian Systems with Scattering Thresholds*, Laser Photonics Rev. **e00811**, 1–6 (2025).
6. A. Tiede, **N. Feldman**, A. Lambertz, A. F. Koenderink and E. Alarcón-Lladó, *Blob Detection for Photonic Metasurface Designing: Angular and Spectral Control of Scattered Light*, submitted to PhotoniX
7. N. de Gaay Fortman, R. Kolkowski, **N. Feldman**, P. Schall, A. F. Koenderink, *Plasmon Lattice Lasers Programmed in Size, Shape and Symmetry*, in preparation.

Author Contributions

Chapter 2 *N. Feldman* and *A. F. Koenderink* conceived the project idea. *N. Feldman* performed measurements, theoretical modeling, interpretation of results and wrote the first draft of the manuscript. *K. M. M. Goeloe* fabricated the sample, performed measurements, interpretation of results and commented on the manuscript. *A. J. den Boef* contributed to discussions and interpretation. *A. F. Koenderink* developed the theoretical model. *L. V. Amitonova* and *A. F. Koenderink* contributed to discussions, interpretation, writing and overall supervision.

Chapter 3 *N. Feldman* and *A. F. Koenderink* conceived the project idea. *N. Feldman* performed theoretical modeling, sample fabrication, measurements, interpretation, and wrote the first draft of the manuscript. *A. J. den Boef* contributed to discussions and interpretation. *L. V. Amitonova* and *A. F. Koenderink* contributed to discussions, interpretation, writing and overall supervision.

Chapter 4 *N. Feldman* and *A. F. Koenderink* conceived the project idea. *N. Feldman* performed theoretical modeling, calculations, interpretation, and wrote the first draft of the manuscript. *N. de Gaay Fortman* wrote the coupled dipole model. *A. J. den Boef* contributed to discussions and interpretation. *L. V. Amitonova* and *A. F. Koenderink* contributed to discussions, interpretation, writing and overall supervision.

Chapter 5 *A. F. Koenderink* and *F. J. García de Abajo* conceived the project idea. *N. Feldman* performed theoretical modeling and calculations, sample fabrication, measurements, interpretation, and wrote the first draft. *J. Pals* performed measurements and interpretation of results. *D. Pal* and *A. F. Koenderink* developed the stratified coupled dipole solver "PyRAMIDS". *A. J. den Boef and F. J. García de Abajo* contributed to discussions and interpretation. *F. J. García de Abajo* commented on the manuscript. *L. V. Amitonova* and *A. F. Koenderink* contributed to discussions, interpretation, writing and overall supervision.

The author acknowledges the use of text-based artificial intelligence tools, which were consulted during the writing of the thesis for suggesting editing improvements in grammar and vocabulary on the sentence level, and which were used in debugging Python algorithms during data analysis.

Acknowledgements

If you have made it to this point, that means you have *carefully* read *all* previous pages in great detail, and we have now both reached the finish line of my thesis. Writing this thing was an incredibly rewarding, frustrating, fulfilling, annoying and beautiful experience at the same time, which would *not* have happened without the help of some people.

First of all, Femius, you have been absolutely instrumental to the creation of this book and in my development as a scientist. Under your guidance I felt the freedom to explore, make my own mistakes and grow from them, while there was always someone having my back. Your devotion to your group members is admirable, as you always make time for a discussion or to even dig into a python code, despite the many *many* other obligations you face. You are a world-class advisor and mentor, and I feel lucky for the opportunity to complete my PhD in your group.

As my PhD was spread over both AMOLF and ARCNL, I've got the chance to reap the benefits from two wonderful institutes. Lyuba, as second promotor you were my mentor at ARCNL, and you always made me feel very welcome to visit the place. You are razor sharp in scientific discussions and I always looked forward to our biweekly meetings, which I already miss. I enjoyed our lively group meetings on Mondays filled with discussion, for which the only thing I blame you was that they were planned *exactly* during lunchtime. Arie, you were our industrial glue with ASML, and with you on our side we never needed to worry about potential usecases in our projects. Thanks for all your curiosity driven questions and input.

I shared the bulk of the ride with 3 other PhD students, with whom I roughly started together back in 2021. Nelson, you seemed to be totally undisturbable no matter what happened, even when the cooling tank of a €200k lasersystem sprays water all of your optical setup. This calming aura also helped me in my "doomsday thinking" to relativize situations when times got tough. Falco, we are opposites in practically every personality trait that exists, and to be honest I did not have a very good first impression of you. Over the years, however, I have grown to truly appreciate you as a colleague/person, and I really enjoyed our joined master's project supervision and "Arie meetings". I learned a lot from you, especially on the social side of things, and I'm happy to have shared this metrology experience with you from the start. Deba, your conscientiousness, work ethic and perseverance in the face of adversity are out of this world. You are always ready to help out a colleague or friend, regardless whether it's 10 o'clock in the morning or in the night, and I look back fondly to the late night sessions in the lab, the intense scientific discussions and "brutally honest" chats about life. Meanwhile, as us "dinosaurs" are all leaving soon, a new generation has arrived. Masha, Kim, Steven, August, thanks for the nice time together in the office (even though *someone* stole my nice window spot, the "Fano whisperers" meetings and the refreshing after-work runs.

Throughout my PhD I have been very lucky to guide 4 students. Kian, your enthusiasm, energy and positive mindset provided a huge boost to the project, and without your little mistake in the GDS file chapter 2 would not even exist in its current form. Joris, being a professional bob-sledder you had quite a busy life filled with trainings and competitions next to your Master's project. Even so, you found a nice balance between your bob-sledding and AMOLF duties, and your precision in the lab ultimately provided the key alignment trick that made life a whole lot easier in measuring those extremely difficult single nanorod reflection spectra of chapter 5. Boris, you were a hands-on experimental beast. You constructed from scratch an extremely complicated phase imaging system, developed code that can extract the necessary information from the images, and fully characterized the whole thing, all within *only 4 months*. Louis, your hands-on skills and initiative in the lab allowed us to measure one of the most complicated and rich metasurface scattering patterns I have ever seen. On top of that, thanks to your perseverance in the "Bessel-expedition", we could ultimately also fully explain those patterns theoretically. All of you brought unique strengths and personalities to your projects, and each and every one of you contributed to the contents of this book in one way or another. It was a pleasure and honor for me to guide you in your projects.

Besides wonderful master's students, I was backed by a squad of highly skilled lab-technicians, a.k.a. the superheroes of AMOLF/ARCNL. Marko and Daniel, our experimental microscopy Gods, without you the lab would turn into complete chaos and mayhem. Thanks for all the lessons, keeping things safe, and for the motivating heavy metal in the background. To the nano-gang, Bob, Igor, Dylan, Rilda, Isabelle, Hans and Arthur, thanks for saving me all these times when the Voyager was crashing or a sample was stuck again in the E-flex.

An AMOLF acknowledgements section is not complete unless mentioning the legendary "magic of AMOLF" at least once. So here goes a big thank you to all the magicians: Pasquale, Ilan, Zihao, Vashist, Said, Roos, Giel, Kevin, Nassim, Govert, Roel, Jente, Jesse, Rene, Daniel, Ewold, Menno, Fons, Timo, Tuoyu, Kostas, Giorgos, Christian, Patrick, Daniel, Evelijn, Matthias, Robin, Kathi, Kasper, Sasha, Zhouping, Ksenia, Max, Tamar, Marc, Jakub and many more, for the jolly atmosphere, nice conversations, support, and laughter these past years. You really made this an awesome experience.

I'll end with some pillars in my personal life. Giulia, thank you for sticking around these past 5 years, you are a truly wonderful person. Roos, dankjewel voor de mooie tijd en avonturen die ik met je heb mogen beleven het afgelopen jaar. Kasper, kerel, heel erg fijn dat je nu lekker dichtbij woont, en dat we voorlopig nog even samen kunnen knallen in de Vondelgym. Yair, Joan, gracias por estar alli en Barcelona, y por las risas. Mam, Pap, Luc, danke veur de wermte, de sjoon fietstochte en de lekker soep dea altied kloarsjtuit es ich weer es richting ut zuje kom.